NOVA SCHOOL OF SCIENCE & TECHNOLOGY

DEPARTAMENT OF LIFE SCIENCES

Inês Ferreira Domingos

BSc in Biomedical Sciences

PHENOTYPIC CHARACTERIZATION OF THE INDUCED P16-POSITIVE CELL POPULATION IN A SPINAL CORD INJURY CONTEXT

MASTER IN MOLECULAR GENETICS AND BIOMEDICINE

NOVA University Lisbon

September 2024

DEPARTAMENT OF LIFE SCIENCES

PHENOTYPIC CHARACTERIZATION OF THE INDUCED P16-POSITIVE CELL POPULATION IN A SPINAL CORD INJURY CONTEXT

Inês Ferreira Domingos

BSc in Biomedical Sciences

Adviser: Doctor Maria Leonor Tavares Saúde
Invited associate Professor, Faculty of Medicine, University of Lisbon/ Principal Investigator; GIMM

Co-advisers: Doctor Maria Alexandra Núncio de Carvalho Ramos Fernandes
Associate Professor with Habilitation, NOVA School of Science and Technology, NOVA University of Lisbon

Examination Committee:

Chair: Doctor Ana Rita Fialho Grosso
Assistant professor, NOVA School of Science and Technology, NOVA Univsersity of Lisbon

Rapporteurs: Doctor Ana Sofia Iria Azevedo Falcão de Jesus
Postdoctoral researcher, NOVA Medical School, NOVA Univsersity of Lisbon

Adviser: Doctor Maria Leonor Tavares Saúde
Invited associate Professor, Faculty of Medicine, University of Lisbon/Principal Investigator; GIMM

MASTER IN MOLECULAR GENETICS AND BIOMEDICINE

NOVA University Lisbon
September 2024

Phenotypic characterization of the induced p16-positive cell population in a spinal cord injury context

ACKNOWLEDGMENTS

Este foi sem dúvida um dos períodos mais desafiantes da minha vida, mas também um dos mais construtivos. Desde horas de almoço às 15h e 16h da tarde em dias de Flow, a acordar a meio da noite para desligar o Confocal, a muitos fins de semana passados no iMM a cuidar dos ratinhos ou os dias intensos de cirurgias. Fazendo agora uma retrospetiva completa, não foi um ano fácil e ser cientista não é de todo fácil. No entanto, olho para os momentos mais desafiantes como as chamadas "dores de crescimento". Durante este último ano não só cresci enquanto cientista, mas também enquanto pessoa. Fui privilegiada com a oportunidade de aprender e ter contacto com os mais variados temas e técnicas e conheci pessoas fantásticas ao longo deste percurso. Quero agradecer a todas essas pessoas com quem este percurso se tornou mais fácil.

Em primeiro lugar, gostaria de agradecer à minha orientadora Professora Dr. Leonor Saúde pelo voto de confiança e pela oportunidade que me deu para aprender. Por ter acreditado em mim, no meu conhecimento e na minha vontade de trabalhar. Agradeço por toda a supervisão e orientação. Agradeço também por promover um ambiente tão descontraído e bom no laboratório e pela relação de proximidade que tem connosco, é realmente um exemplo. Quero também agradecer a todos os membros do laboratório, foram todos fantásticos comigo e tornaram esta experiência ainda mais enriquecedora, foi um orgulho pertencer a uma equipa tão fantástica. Um agradecimento especial à Ana Isidro e ao Daniel Ribeiro. Ana, muito obrigada por toda a tua paciência e disponibilidade, por me transmitires o teu conhecimento desde o dia 1, experimentação animal não é fácil em todos os aspetos e, sem ti e sem o teu conhecimento não teria conseguido fazer este projeto. Dani, foi um prazer, obrigada por toda a ajuda, pelo acompanhamento e conhecimento, pelos momentos divertidos no laboratório e pelos momentos "sem filtro" também. Foi um prazer ter concluído o nosso "alfas Project" contigo. Aos meus master colegues por terem estado comigo neste barco.

Quero agradecer também à minha co-orientadora Professora Dr. Alexandra Fernandes, por todo o acompanhamento desde o dia 1 do mestrado e agora também no ano de tese.

Agradeço também a todos os meus amigos por me terem ajudado nos tempos mais difíceis, mas também por terem celebrado comigo as minhas conquistas. Ao meu parceiro do crime, palavras não chegam para todo o apoio que me tens dado especialmente neste último ano. Obrigada por nunca me teres deixado desistir (quem nunca pensou em desistir da tese que atire a primeira pedra), puxaste sempre, sempre por mim mesmo quando eu não achava que o conseguia fazer. Hoje entrego esta tese muito por ti, pelo teu apoio, pela tua ajuda e também por ter tido um ombro e um abraço nos dias mais difíceis

(também fazem parte). Agradeço do fundo do coração tudo o que fizeste e fazes por mim todos os dias, nunca, mas nunca estive sozinha, estiveste sempre lá every step of the way, contigo sou a minha melhor versão. Sou muito sortuda por viver um amor assim, obrigada por impulsionares as minhas maiores conquistas. Por último, à minha base, a minha família, os que estão lá desde o dia um. Nunca me impediram de voar, sempre me encorajaram, sempre me apoiaram. Estou onde estou graças a vocês e ao vosso amor. Mãe, Pai, Pedro, Fábio, Marco, Anas, Guilherme, Eva, Tomás, Maria, Vicente, Vasco, Avó Luísa, Avó Maria, Avô Joaquim e Avô Zé, a minha família, amo-vos, obrigada por tudo. Nem todos estão aqui para presenciar, dedico-vos esta conquista.

“Tudo é ousado para quem a nada se atreve.” (Fernando Pessoa).

ABSTRACT

A spinal cord injury (SCI) is a highly disruptive condition that causes non-resolving neurologic damage to the spinal cord. Senescent cells are known to be upregulated after SCI, with devastating consequences for the tissue. p16 is a known marker of senescence, however its expression did not follow the same tendency as other senescent cell populations. We aimed to perform a phenotypic characterization of these p16-positive cells using a new p16-FDR mouse line, with an mCherry reporter gene. We optimized a single-cell spinal cord dissociation protocol for flow cytometry and fluorescence-activated cell sorting (FACS), enabling a comprehensive cellular characterization. We showed the induction of an injury-specific p16-mCherry population at 7 days post-injury (dpi), which is enriched in neurons. Additionally, by flow cytometry, we also identified a new injury-specific mCherry macrophage population. All these results together with the selective elimination of p16-mCherry-positive cells that revealed a transient locomotor impairment at 15 dpi, suggested an important functional role of these cells. Meanwhile, pharmacological treatment with a senolytic, ABT-263, did not eliminate p16-positive cells, questioning their canonical senescence nature. However, transcriptomic profiling of sorted mCherry-positive cells revealed an upregulation of immune and senescence-associated genes. Taken together, our comprehensive approach has uncovered new insights into the intricate profile of mCherry-positive cells and the interaction between senescence and tissue repair.

Keywords: Spinal cord; Spinal cord injury; Cellular senescence; p16; Regeneration

RESUMO

Uma lesão vertebro-medular é uma condição altamente devastadora que promove danos neurológicos permanentes inferiormente ao local da lesão. Sabe-se que as células senescentes são induzidas após lesões deste tipo, e que a sua persistência acarreta consequências devastadoras para o tecido. p16 é um marcador clássico de senescência, no entanto, a sua expressão não segue a mesma tendência observada noutras populações de células senescentes. A identidade desta população p16-mCherry ainda não é conhecida. Deste modo, o nosso objetivo incidiu em realizar uma caraterização fenotípica das células p16-positivas utilizando um novo modelo p16-FDR, com um gene reporter *mCherry*. Para tal, otimizámos um protocolo de *single-cell* apto para citometria de fluxo e *fluorescence-activated cell sorting* (FACS), permitindo uma caraterização celular abrangente. Demonstrámos a indução de uma população mCherry específica aos 7 dias após a lesão, que é enriquecida em neurónios. Além disso, por citometria de fluxo, identificámos uma nova população de macrófagos p16-mCherry positiva. Estes resultados, juntamente com uma eliminação seletiva de células mCherry-positivas que revelaram uma deficiência locomotora transitória aos 15 dias após lesão, sugeriram um papel funcional importante destas células. O tratamento farmacológico com um potente senolítico, ABT-263, não eliminou as células p16-positivas, questionando a sua natureza senescente. No entanto, o perfil transcricional das células mCherry-positivas sorteadas por FACS revelou um aumento de expressão de genes implicados em processos de imunidade e senescência. A nossa abordagem abrangente revelou novos conhecimentos sobre o perfil complexo das células mCherry-positivas e a interação entre a senescência e a reparação de tecidos.

Palavras chave: Medula espinhal; Lesões na medula espinhal; Senescência; p16; Regeneração

CONTENTS

LIST OF FIGURES

LIST OF TABLES

.

ACRONYMS

ACSA-2	Astrocyte Cell Surface Antigen-2
AMI	Acute Muscle Injury
AMPA	α-Amino-3-hydroxy-5-methyl-4-isoxazolepropionic acid
APOE	Apolipoprotein E
ATP	Adenosine Triphosphate
BCL2	B-cell lymphoma 2
BMS	Basso Mouse Scale
BSCB	Blood-Spinal Cord Barrier
CCFs	Cytoplasmic Chromatin Fragments
CCGs	Chondroitin Sulfate Proteoglycans
CCL2	Chemokine C-C motif ligand 2
CCL20	Chemokine C-C motif ligand 20
CD13	Cluster of Differentiation 13
CD31	Cluster of Differentiation 31
CD45	Cluster of Differentiation 45
CDKIs	Cyclin-Dependent Kinase Inhibitors
cGAMP	Cyclic GMP-AMP
cGAS	Cyclic GMP-AMP Synthase
CHAT	Choline Acetyltransferase
CNS	Central Nervous System
CSF	Cerebrospinal Fluid
DAPI	4',6-Diamidino-2-Phenylindole
DGAV	Direção-Geral de Alimentação e Veterinária
dpi	days post-injury
DT	Diphtheria Toxin
ECF	Extracellular Fluid
ECM	Extracellular Matrix
ER	Endoplasmic Reticulum

FACS	Fluorescence-Activated Cell Sorting
FAPs	Fibro-Adipogenic Progenitors
GFAP	Glial Fibrillary Acidic Protein
GLB1	Galactosidase, beta 1
Gro-α	Growth-Regulated Oncogene Alpha
H3K9me	Histone H3 Lysine 9 Methylation
HP1	Heterochromatin Protein 1
hpi	hours post-injury
HSC	Hepatic stellate cells
Iba-1	Ionized Calcium-Binding Adapter Molecule 1
IFN-γ	Interferon gamma
IH	Infinite Horizon
IHC	Immunohistochemistry
IL-1β	Interleukin-1 beta
IL-6	Interleukin-6
LMNB1	Lamin B1
log2FC	Logarithm Base 2 Fold Change
MMP	Matrix Metalloproteinase
MPSS	Methylprednisolone Sodium Succinate
NET	Neutrophil Extracellular Trap
NMDA	N-Methyl-D-Aspartate
Nogo-A	Neurite Outgrowth Inhibitor A
NPC	Neural Progenitor Cell
NSC	Neural Stem Cell
OPCs	Oligodendrocyte Precursor Cells
ORBEA	Orgão de Bem-Estar e Ética Animal
P2A	P2A Peptide
PAI-1	Plasminogen Activator Inhibitor-1
PB	Phosphate Buffer
PDGF-AA	Platelet-Derived Growth Factor AA
PFA	Paraformaldehyde
RBC	Red Blood Cells
RNA-seq	RNA Sequencing
RNS	Reactive Nitrogen Species
ROS	Reactive Oxygen Species
RT	Room Temperature
SA-β-gal	Senescence-Associated β-Galactosidase
SAHF	Senescence-Associated Heterochromatin Foci
SASP	Senescence-Associated Secretory Phenotype
SC	Spinal Cord
SCI	Spinal Cord Injury
SeCs	Senescent Cells
Spp1	Secreted Phosphoprotein 1, also known as Osteopontin
sq	Subcutaneous

STING	Stimulator of Interferon Genes
TGF-β	Transforming Growth Factor Beta
TIF	Telomere Dysfunction-Induced Focus
TNF-α	Tumor Necrosis Factor Alpha
UPR	Unfolded Protein Response
UTIs	Urinary Tract Infections
VEGF	Vascular Endothelial Growth Factor
WHO	World Health Organization

1

INTRODUCTION

1.1 Spinal cord - the master cable of communication

1.1.1 Structure and Function of the Spinal cord in mammals

The spinal cord (SC) is positioned within the vertebral column and stands as a crucial part of the central nervous system (CNS). It runs from the brainstem, through the foramen magnum, to the L1 and L2 vertebrae before phasing out at the conus medullaris. Finally, it stretches into the “cauda equina”, a bundle of nerve roots **(Fig 1.1. A)** [1][2]. The central canal runs longitudinally through the center of the spinal cord and connects to the brain's ventricles which are filled with cerebrospinal fluid (CSF). CSF conveys hydromechanical protection to the CNS, while also being an important player during brain development and in maintaining the homeostasis of the brain interstitial fluid[3]. The spinal cord can be divided into three regions through the laminar designation: dorsal, intermediate, and ventral **(Fig 1.1. B).** The dorsal horns process external sensory information, while the ventral horns control motor execution and generate rhythmic motor behaviors. The intermediate spinal cord integrates sensory and descending information to fine-tune motor output[4]. The spinal cord is composed of gray matter surrounded by white matter, resulting in a butterfly-like or H-shaped structure when viewed in a cross-section (**Fig 1.B**)[1] [4] [5]. The gray matter's "H" supports the right and left dorsal and ventral horns[4]. It is composed of cell bodies of motor and sensory neurons, interneurons, neuroglia cells, and mostly unmyelinated axons. In contrast, the white matter is composed mainly of interconnecting fiber tracts, which are primarily myelinated sensory and motor axons. While ascending tracts transmit information from sensory receptors to higher levels of the CNS, descending tracts convey information from the CNS to the periphery [4]. This complex structure of the spinal cord is responsible for conducting information from the brain to the periphery and vice versa. As a segmented structure, its neural segments correspond to the nerve roots that extend between each vertebra. In total, there are 31 spinal nerve roots: eight cervical, twelve thoracic, five lumbar, five sacral, and one coccygeal, all of which play a role in regulating important physiological processes such as respiration, heart rate, and temperature[2].

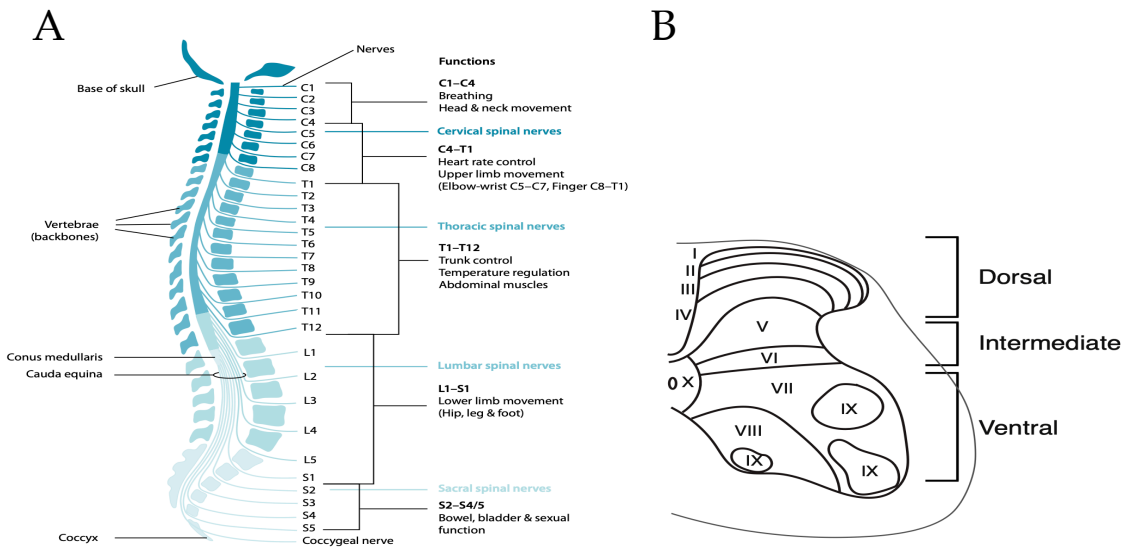

Figure 1.1 Structure of the spinal cord. (A) Longitudinal organization of the spinal cord (with cervical, thoracic, lumbar, and sacral segments shaded), spinal vertebrae, and spinal nerves and a rough representation of its major functions. Adapted from Lukersmith et al. (2013)[2]. **(B)** Lamination pattern of the spinal regions – dorsal, intermediate, and ventral. From Peter J Osseward II et al. (2019) [4].

1.2 Spinal cord Injury (SCI) – the bridge waiting to be crossed

A spinal cord injury (SCI) is a condition that causes non-resolving neurologic damage to the SC. SCI entails highly disruptive and complex events from both the medical and patient perspectives, being a life-altering condition. SCI patients experience physical dependence due to the loss of physiological functions such as partial or total loss of motor and sensory functions below the injury level as well as high psychological and financial burden, and increased morbidity [2] [6] [7]. The World Health Organization (WHO) 2013 statistics reveal an estimated global incidence of SCI of 40 to 80 new cases per million inhabitants annually, reflecting that each year, 250,000 to 500,000 people suffer an SCI[2]. The vast majority of these cases are traumatic SCI due to road accidents, however, they can also result from falls, sports injuries, or violence [2] [6]. SCIs can be categorized as traumatic or non-traumatic, depending on the cause of the injury. Traumatic SCI is the result of high-intensity injuries caused by external physical impact, such as those sustained in traffic accidents. Non-traumatic SCIs, on the other hand, can be caused by acute or chronic illnesses such as infections, tumors, degenerative disorders of the vertebral column, or vascular issues[6]. Regarding severity, SCIs can be classified into complete or incomplete. In the case of a complete injury, there is no nerve communication below the site of injury, while in an incomplete injury, some communication in the spinal cord remains intact, allowing for some sensory-motor control below the injury site[8]. However, SCI does not exclusively entail motor and sensory deficits. SCI patients can also experience various injury-related secondary complications. These complications may encompass orthostatic hypotension, which refers to a sudden drop in blood pressure upon assuming an upright position, urinary tract infections (UTIs), and sublesional osteoporosis resulting from bone mass loss after injury [2].

According to the pathophysiology, acute SCI can be divided into primary and secondary injuries, the former is the stage immediately after the injury and is due to the mechanical injury to the spinal cord. The primary injury triggers the secondary injury through the activation of a cascade of cellular,

molecular, and biochemical events that further damage spinal tissues causing tissue dysfunction and preventing neurological recovery **(Fig 1.2)**[6][7].

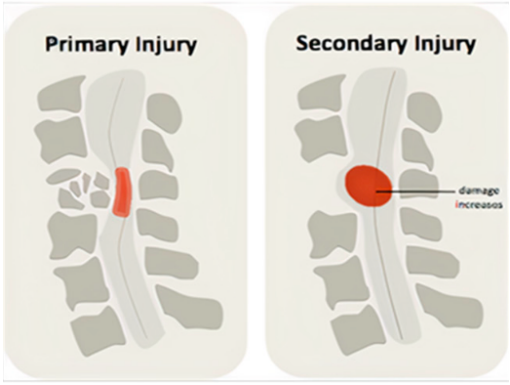

Figure 1.2. Primary and secondary phases of a SCI. The primary injury occurs due to sudden trauma to the spinal cord triggering a complex cascade of events leading to a secondary injury promoting further tissue dysfunction. From Anam Anjum et al.(2020)[7]

1.2.1 Primary Mechanisms of Spinal Cord Injury

As mentioned above, the primary injury results from mechanical damage at initial impact, where bone fragments, disc compartments, and spinal ligament tearing damage the spinal cord tissue [6] [7]. This primary impact can cause compression, contusion, or transection injuries to the spinal cord, the latter being an anatomically complete lesion[9]. The most frequent type of injury is contusion, followed by compression as a result of vertebral fracture and dislocation. The severity of the injury is determined by its location, the extent of initial damage, and the duration of compression [7]. After the initial impact, there is a breakdown of the blood-spinal cord barrier (BSCB), hemorrhage, and destruction of neural parenchyma, axonal network, and glial membranes [7]. The rupture of cellular membranes, and local blood vessels, promotes the release of cytotoxic factors and compromises oxygen supply leading to ischemia and hemorrhage events that increase local pressure on the spinal cord and result in edema [7]. These events trigger a secondary injury, causing further damage to spinal tissues and neurological dysfunction that can, in some cases, excess the damage caused by the primary injury[10].

1.2.2 Secondary Mechanisms of Spinal Cord Injury

The activation of the secondary injury phase promotes further chemical and mechanical damage to spinal tissues. It is initiated minutes after primary injury and can last for several weeks [7][11].
The secondary injury mechanism can be divided into acute (0-48 hours post-injury (hpi)), sub-acute (48 hpi to 14 days post-injury (dpi)), and chronic injury (from days to years), following a distinct but somewhat overlapping temporal sequence **(Fig 1.3)** [7], [10], [11].

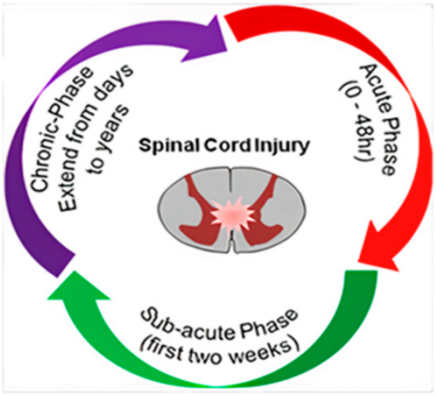

Figure 1.3. Temporal classification of the secondary phase of a SCI. The secondary phase can be divided into acute (0-48 hours post-injury (hpi)), sub-acute (48 hpi to 14 days post-injury (dpi)), and chronic injury (from days to years). From Anam Anjum et al.(2020) [7]

The acute phase is characterized by vascular damage, hemorrhage, ischemia, edema, inflammatory cell infiltration, ionic imbalance, excitotoxicity, free radical production, increased calcium influx, lipid peroxidation, and inflammation, among others. It is also characterized by necrosis, in the first instance due to mechanical trauma and followed by apoptosis of neuronal and glial cells, such as oligodendrocytes, within hours after injury **(Fig 1.4.A).** These events also trigger demyelination and the loss of neural circuits [7], [10], [11]. In a more detailed view of the acute phase, the destruction of the main microvasculature upon injury leads to hypovolemia due to excessive bleeding. This promotes cell permeabilization allowing leukocytes and red blood cells (RBCs) to extravasate to the injury site, resulting in edema and exerting pressure on the injured spinal tissues, thereby compromising blood flow to the rest of the spinal cord[7]. Severe hemorrhage also exposes the spinal cord to an incredible influx of inflammatory cells, namely macrophages, neutrophils, and lymphocytes. Additionally, it is exposed to inflammatory cytokines such as interleukin (IL)-1β, interleukin-6 (IL)-6, tumor necrosis factor-α (TNF-α), and vasoactive peptides[7], [11]. Furthermore, vascular disruption promotes pro-apoptotic signaling, and ischemic injury, leading to cell dysfunction and death. Altogether, this highly inflammatory tissue environment combined with a disrupted BSCB contributes to further spinal cord swelling. This swelling can increase mechanical compression on the spinal cord, worsening the injury [7], [10].

In the subacute phase, events from the acute phase continue, with ongoing edema exacerbating ischemia and the recruitment of inflammatory cells promoting further cell death[10], [11]. This phase is also characterized by axon demyelination, Wallerian degeneration, axon and matrix remodeling, and immune-mediated neurotoxicity [7]. Given the structural alterations to the spinal cord architecture and cell death, cystic microcavities are formed. Moreover, in the perilesion area, there is the deposition of extracellular matrix (ECM) molecules as a result of astrocytic proliferation and glial scar formation **(Fig 1.4.B)**[10]. In a finer-grained view, there is a loss of intra and extracellular ionic homeostasis, due to an increase in intracellular concentration of Ca^{2+} in neurons and glia[10]. Initially, this increase derives

from the mechanical injury itself causing breaches in the cells' plasma membranes resulting in an ionic imbalance[11]. Later on, a phenomenon known as glutamate excitotoxicity also contributes to this imbalance. Glutamate, a major excitatory neurotransmitter, is released in excessive amounts after an injury by dying astrocytes and neurons, and surviving astrocytes are not able to uptake glutamate to its normal levels. The excess of glutamate promotes the overactivation of NMDA (N-methyl-d-aspartate), AMPA (α-amino-3-hydroxy-5-methyl-4-isoxazole propionic acid), and kainate receptors, thus promoting the influx of Ca^{2+} and Na^{+} ions [7], [10], [11]. Excess of glutamate coupled with dysfunctions in the ATP-dependent ion pump results in an increase in intracellular concentrations of Ca^{2+} and Na^{+} and a decrease in K^{+}[7]. Neurons and oligodendrocytes are especially susceptible to glutamate excitotoxicity as they have a complete set of glutamate receptors[11]. Higher levels of Ca^{2+} inside the cell activate fundamental enzymes, caspases, and calpains that induce apoptosis by cleaving cytoskeleton and membrane proteins[7], [11]. The excess of Ca^{2+} also leads to mitochondrial dysfunction, resulting in the formation of reactive oxygen species (ROS) and reactive nitrogen species (RNS). This oxidative stress environment causes lipid peroxidation and damage to proteins and nucleic acids, thus contributing to necrotic and apoptotic cell death [7], [10], [11]. Moreover, ATP and DNA released by necrotic cells activate microglia. Activated microglia infiltrate the injury site, further aggravating the inflammatory response and promoting additional cell death[10]. Loss of glial cells, mainly oligodendrocytes, results in the demyelination of axons. Without myelin, neurons are directly exposed to the effects of inflammatory cytokines, ROS, and RNS which result in more necrosis and apoptosis. The consequence is a partial or complete loss of axonal transmission, which contributes to motor and sensory impairments[11]. As the inflammatory response from previous phases decreases, there is an attempt at remyelination, reconstruction of the vascular architecture, and remodeling of neural circuits. However, these attempts often fail due to the overall detrimental microenvironment that has been established[10].

Then the chronic phase, the final phase, is initiated and it is marked by the formation of cysts and the maturation of the glial scar **(Fig 1.4.C)**[7]. Cystic microcavities are composed of extracellular fluid (ECF), connective tissue, and macrophages that fuse together forming a physical barrier to axonal regrowth and a poor substrate for cells to migrate. Around the cystic cavity, reactive astrocytes proliferate and interconnect their processes to form the glial scar[7], [10], [12]. In addition to astrocytes, the glial scar also contains pericytes and connective tissue[7]. Interestingly the population of pericytes is twice that of astrocytes. These pericytes produce various molecules that can stimulate fibroblasts to produce fibronectin, an ECM component, that contributes to the formation of scar connective tissue.

The glial scar is a double-edged sword, it constitutes a physical barrier to axon regeneration, however, it also isolates the injury site by preventing the spreading of the injury to adjacent healthy parenchyma. Also, astrocytes provide trophic support and promote neovascularization[10].

As a result of these events, the SCI lesion is composed of a nonneural lesion core due to its toxic environment, a glial scar at the peri lesion site, and a spare but reactive neural tissue that contains neurons, astrocytes, oligodendrocytes, oligodendrocyte precursor cells **(**OPCs), and microglia[6], [13].

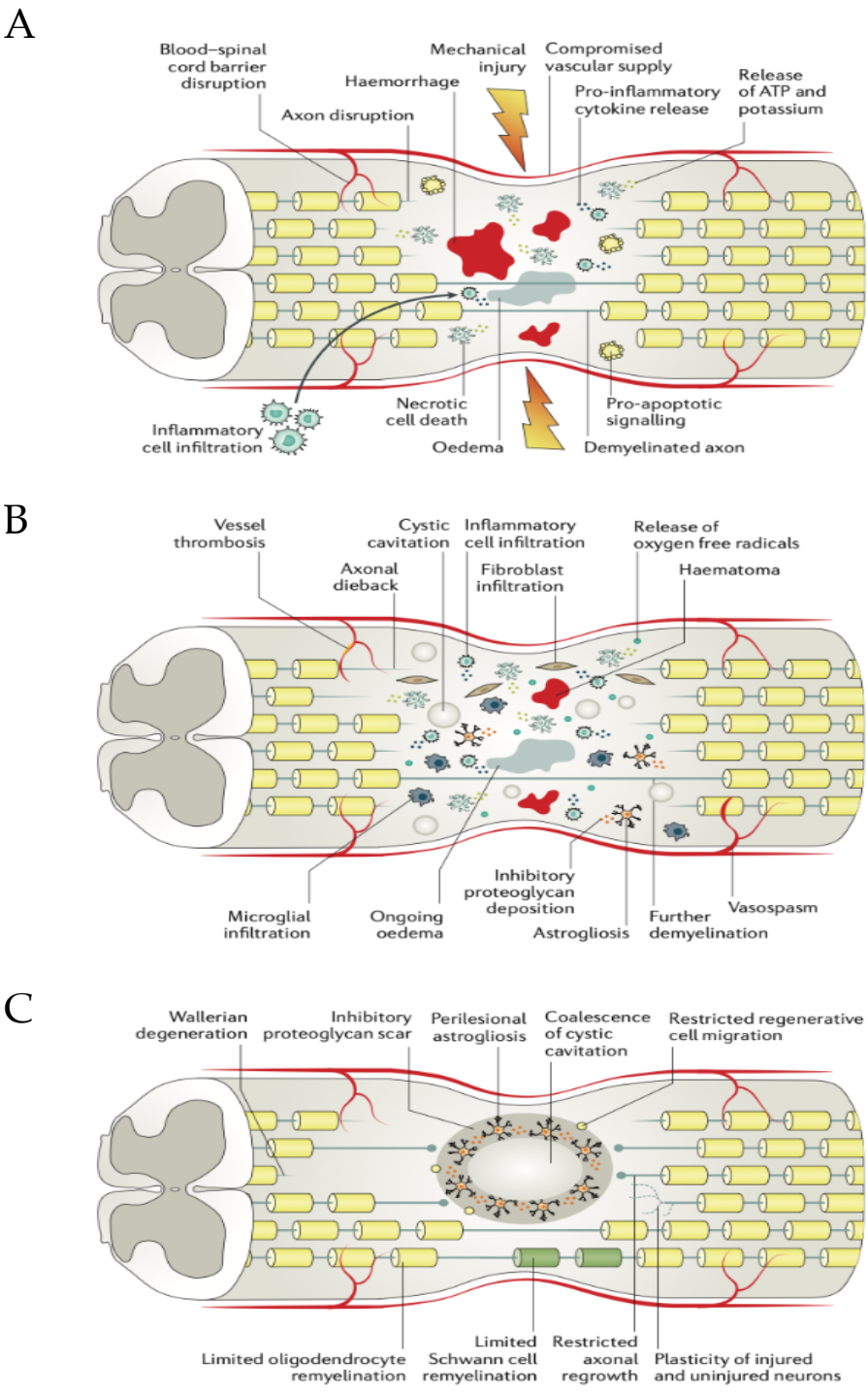

Figure 1.4.Pathophysiological events after a SCI. A) In the acute phase, edema, hemorrhage, and ischemia occur, leading to a consequent infiltration of inflammatory cells. Necrosis and apoptosis of neurons and glial cells are also observed leading to the loss of neural circuits. B) In the subacute phase, events from the acute phase continue, and inflammation continues, leading to further cell death. Cystic microcavities are formed during this phase. C) In the chronic phase, the glial scar matures, inhibiting regeneration. Cystic cavities coalesce to further restrict axonal regrowth and cell migration. From Ahuja et al. (2017) [10]

1.2.3 Cell types that coordinate the injury response

Cells involved in a SCI process can originate from the nervous, immune, or vascular systems and are categorized into either intrinsic or blood-borne cells [7]. The cellular response is fundamental in an injury context, and it is important to understand its temporal and spatial dynamics to be able to find effective therapeutic strategies **(Fig 1.5)** [6]. This section aims to provide a deeper insight into both SC resident cell types and those recruited from the circulatory system in the context of SCI, bearing in mind the pathophysiology described in the section above.

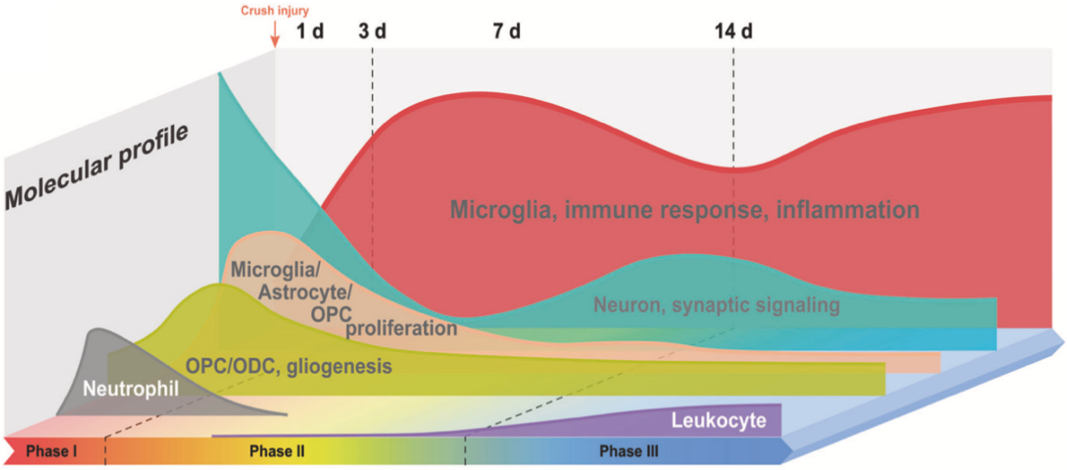

Figure 1.5 Cellular changes upon a SCI. Several cells are involved in a SCI context that can be from the nervous, immune, or vascular systems and are categorized into either intrinsic or blood-borne cells. These cells present different temporal profiles being recruited at different timepoints. Oligodendrocyte precursor cells (OPCs). From Xiao Hu et al. (2023) [6]

Immune cells

There are four major cell types that are recruited upon an SCI: neutrophils, monocytes/macrophages, tissue-resident microglia, and lymphocytes[11].

In situ immune cells

Microglia are the innate immune cells of the CNS. Upon injury, these cells go through a series of morphological and molecular changes to be able to phagocytize and remove debris. They also adopt a pro-inflammatory phenotype that contributes further to the secondary injury. Regarding inflammation, microglia are known to exert namely a M1 or M2 phenotype. M1 is mainly pro-inflammatory, aggravating the inflammatory response and promoting neuroinflammation. In contrast, M2 has anti-inflammatory properties and promotes tissue repair. However, this classification is not objective as there can be more subtypes of microglia[6]. After SCI, it has been suggested that there are two peaks of microglial activation. Nguyen et.al reported that upon a contusion SCI in rats, microglia peak at 7 dpi and 60 dpi [14]. Similar temporal distributions have been observed in mice studies[6]. While microglia rapidly

disappear from the lesion core, they are maintained at the lesion periphery exhibiting a pro-inflammatory phenotype[6].

Blood-derived immune cells

Neutrophils are the first immune cells to be recruited to the injury site, typically detected 2 hours after the injury and peaking at 3 dpi in mice[6]. They act as a triggering factor of the secondary injury. Neutrophil recruitment occurs through signals produced by resident cells, that secrete adhesion molecules and cytokines (IL-1β, TNF), which guide neutrophils to the damaged site. In this setting, neutrophils have mainly a detrimental role by releasing a wide variety of pro-inflammatory molecules, ROS, lysosomal enzymes, and proteolytic enzymes (such as matrix metalloproteinase-9, MMP-9), which in turn activate other inflammatory and glial cells contributing to neuronal death [6], [11]. Neutrophils also release neutrophil extracellular traps (NETs) that further contribute to neuroinflammation and BSCB destruction[11]. Nevertheless, these cells can also have a beneficial role by removing microbial species and tissue debris and favoring macrophage phagocytosis [6].

Myeloid-derived monocytes infiltrate the spinal cord and differentiate into macrophages after the injury[6], [11]. Macrophages, as microglia, also have M1 (pro-inflammatory) and M2 phenotypes (anti-inflammatory). M1 is detected at high levels in the early phases of the injury and the levels are maintained, whereas M2 macrophages have a brief peak and return to the basal levels after 1-week post-injury. It has been suggested that this biased macrophage polarization may be due to the elevated levels of iron and myelin debris from the injury. Macrophages have a higher phagocytic ability than activated microglia. However, like microglia, macrophages also produce several cytokines and growth factors and clear myelin sheath fragments and necrotic tissue that need to be removed. The excessive phagocytosis of lipid-rich myelin sheaths has a downside: it leads to the formation of foam macrophages. This in turn leads to an impaired phagocytic ability and results in further damage to the neural tissue. [6]

Lymphocytes play a rather controversial role in a SCI context. The primary cell types involved in adaptive immunity are T and B lymphocytes [6]. After an injury, T cells peak at 7 dpi but can be detected as early as 1 dpi and remain sustained for as late as 180 dpi. These cells seem to have a detrimental role. CD8 T cells, for example, secrete perforin, which has been shown to damage the BSCB. This damage increases the barrier's permeability to inflammatory cells and its cytokines, thereby worsening the damage to the CNS. Moreover, T-cell infiltration in the dorsal spinal cord is a well-recognized factor contributing to neuropathic pain in adults. Furthermore, it has been shown that γδ T cells produce interferon-γ (IFN-γ), further contributing to the inflammatory response. In contrast to its unfavorable role, it has been shown that an increase in Th2 cells stimulates the phenotypic polarization of Th1 and M1 cells (proinflammatory role) into Th2 and M2 cells (anti-inflammatory role). This shift ameliorates the local microenvironment making it more permissive to repair[6].

Neurons and Neural stem cells (NSCs)/ Neural progenitor cells (NPCs)

SCI is marked by a profound loss of mature neurons, which is the principal cause of functional impairments in this context. Neuronal apoptosis is an early-stage event, being detected as early as 4 hours after an injury and peaking at 8 hours. This results in a significant reduction in the number of axons at the injury site. Some axonal sprouting may be observed at 6 hours post-injury, possibly due to Calpain activation or axonal protein synthesis. In addition, the spinal cord has endogenous neural stem cells (NSC) and neural progenitor cells (NPCs) that give rise to newly formed astrocytes and oligodendrocytes [6].

Astrocytes

Astrocytes are the most numerous supporting cells in the CNS. They are responsible for maintaining the homeostasis of the CNS, providing metabolites for neurons, and modulating local blood flow. Upon injury, astrocytes become reactive, presenting reversible alterations in gene expression and morphology. When activated, they protect the healthy spinal cord from inflammatory cell infiltration, minimizing the initial damage. However, over time, they take part of the permanent glial scar, that acts as a barrier to regeneration[6]. In the first 7 to 10 dpi astrocytes proliferate and organize alongside the margin of the injury completely covering the scar in the first 2 to 3 weeks following the injury[7]. Interestingly, microglia is the primary cell type that initiates reactive astrogliosis. Similarly, to other cell types, astrocytes can be classified into A1 or A2. A1 cells, induced by inflammation, are neurotoxic, while A2 cells, triggered by ischemia, possess neuroprotective properties[6].

Oligodendrocytes and OPCs

Oligodendrocytes undergo apoptosis within the first 24 hours after the injury, and the loss of these cells peaks at 8 dpi. However, OPCs serve as a source for generating new oligodendrocytes following a SCI, constituting approximately 5-8% of cells in the CNS. When damage is present, OPCs are activated and proliferate into new oligodendrocytes and Schwann cells, to regenerate damaged axons, repair damaged myelin sheaths, and participate in the astrocyte scar formation. The ability to remyelinate damaged axons is often restricted given the toxic environment established upon injury.

It is important to note that there is a complex interplay between different cell types upon an injury. For example, the inflammatory microenvironment induced by immune cells contributes to neuronal death. Reactive astrocytes can further enhance this inflammation by interacting with microglia through fibronectin within the glial scar [6].

1.2.4 Therapeutic Strategies

The adult mammalian CNS has minimal ability to repair itself following an injury[8]. These barriers to regeneration can be due to an inherent lower plasticity of the CNS when compared with the Peripheral Nervous System (PNS), which exhibits a higher capacity for axonal regeneration. The inhibitory nature

of the CNS myelin also constitutes another barrier. Myelin-associated proteins, for example, neurite outgrowth inhibitor A (Nogo-A), bind to specific receptors activating pathways that ultimately result in apoptosis and collapse of regenerating axons and neurite retraction. Moreover, hypertrophic astrocytes create a physical barrier for regeneration by forming the glial scar and a chemical barrier by secreting inhibitory molecules, such as growth-inhibitory chondroitin sulfate proteoglycans (CSPGs) [15].

The primary injury is irreversible and cannot be prevented. Therefore, it is not the main intervention target. However, in some cases, continuous pressure on the spinal cord due to repetitive or persistent mechanical insults can exacerbate the primary injury. In such cases, decompressive surgery and vertebrae stabilization are advised. This surgery aims to realign the spinal column, increase spinal stability, and reduce compression to the spinal cord[6].

In contrast, secondary injury is the hotspot for finding therapeutic interventions that aim to reduce the extent of the injury and improve the possibility of recovery[11]. Pharmacological approaches include the use of steroids, such as Methylprednisolone (MPSS), which exerts an anti-inflammatory effect and reduces oxidative stress, thereby promoting the survival of neural cells[6], [15]. In addition to the use of steroids, some neuroprotective and neuroregenerative strategies have been making their way into clinical research. Regarding neuroprotection, Riluzole, a sodium channel blocker, prevents the excessive influx of sodium in injured neurons and limits the release of glutamate at the presynaptic level. This in turn counteracts the effects of the ionic imbalance observed upon SCI, preventing cellular swelling and excitotoxicity. Magnesium is another strategy, as an NMDA receptor antagonist, magnesium reduces excitotoxic damage to neurons and decreases inflammation[15]. Finally, Minocycline is a structural analog of the antibiotic tetracycline and seems to exert an anti-inflammatory effect by inhibiting microglial activation, IL-1β, TNF-α, cyclooxygenase-2, and matrix metalloproteinases [6], [11], [15]. The anti-NOGO antibody is an example of a neuroregenerative therapy. This is a monoclonal antibody against Nogo-A, an inhibitory component of myelin, this can be a promising tool to promote axonal regeneration[15]. Cell-based therapies also hold an exciting promise, as transplantation of different cell types into the injured spinal cord, such as neural stem/precursor cells, mesenchymal stem cells, or even Schwann cells can provide trophic support, modulate the inflammatory response, regenerate lost neural circuits and remyelinate axons[11], [15]. The formation of a cystic cavity upon injury impairs cell migration and axon growth due to the lack of support to guide these processes. Biomaterials offer a promising solution by mimicking the intricate structure of the ECM, thereby filling the cavity. Additionally, these materials can be engineered to incorporate growth factors and stem cells, which further promote tissue regeneration. Furthermore, biodegradable biomaterials serve as temporary scaffolds that guide the regenerative process before gradually degrading as healing progresses[10]. Incredible technological research has also made its way into this field. Lorach et al. made a groundbreaking development in enabling an individual with chronic tetraplegia to stand and walk naturally again using a brain–spine interface. This cutting-edge approach involves a wireless implantable communication system that connects the brain and spinal cord, bypassing the injured area. Although this breakthrough was validated in only one individual and its efficacy in other SCI conditions remains uncertain, it represents a major and promising step forward [16] Finally, it is important to note that a combinatorial approach may be

more beneficial, as it targets several mechanisms simultaneously, thereby addressing the complexity of spinal cord injuries more effectively [6], [11].

1.3 Cellular Senescence– the identity on the making

The concept of cellular senescence was born in the 1960s when Hayflick and his colleagues discovered that human fibroblasts could not divide indefinitely in culture and enter a state of irreversible cell cycle arrest that was termed senescent[17], [18].
Various stressors, such as oxidative stress, chemotherapy, irradiation, and nutrient deprivation can trigger senescence **(Fig. 1.6)**[17], [19], [20]. Notably, mechanical stress can also lead to senescence. For instance, our laboratory has demonstrated that after an SCI, senescence is induced at the lesion's periphery [13]

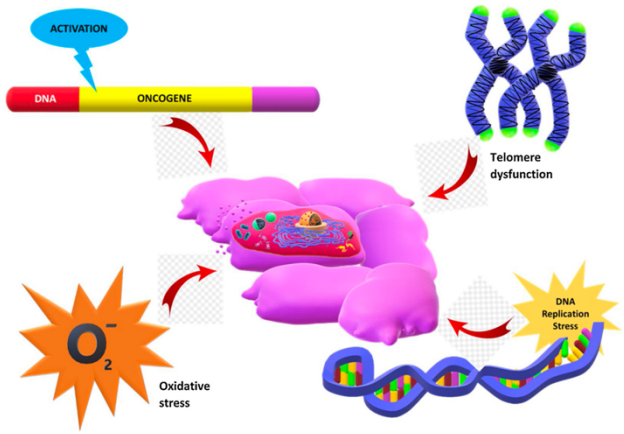

Figure 1.6. Different stimuli that induce cellular senescence. Cellular senescence can be triggered by a wide variety of stimuli. From Kamal et al. (2020) [21]

Senescence is far away from being a straightforward topic, nevertheless, it is generally defined by the onset of irreversible cell cycle arrest. This occurs due to the upregulation of cell cycle inhibitors, cyclin-dependent kinase inhibitors (CDKIs), such as $p16^{INK4a}$ (p16), $p21^{CIP1}$ (p21), and p53 with the retention of metabolic activity and viability[19], [21]. Regarding the induction mechanism of cell cycle arrest, DNA damage response signals initially stabilize p53 and activate p21. When the DNA damage persists, p16 is activated by the ETS family of transcription factors. Both CDKIs, p16 and p21, maintain the RB protein (a crucial cell cycle stopper) in its dephosphorylated form, thereby contributing to a stable cell cycle arrest [20], [21].

1.3.1 Hallmarks of Senescence

Senescent cells (SeCs) undergo a series of phenotypic changes that distinguish them from normal cells **(Fig 1.7)**. It is important to note that senescence is a highly heterogeneous process, and there is no one-

size-fits-all senescence marker. Not all SeCs express the same markers, and none of the markers are absolutely specific to label all SeCs[17], [21].

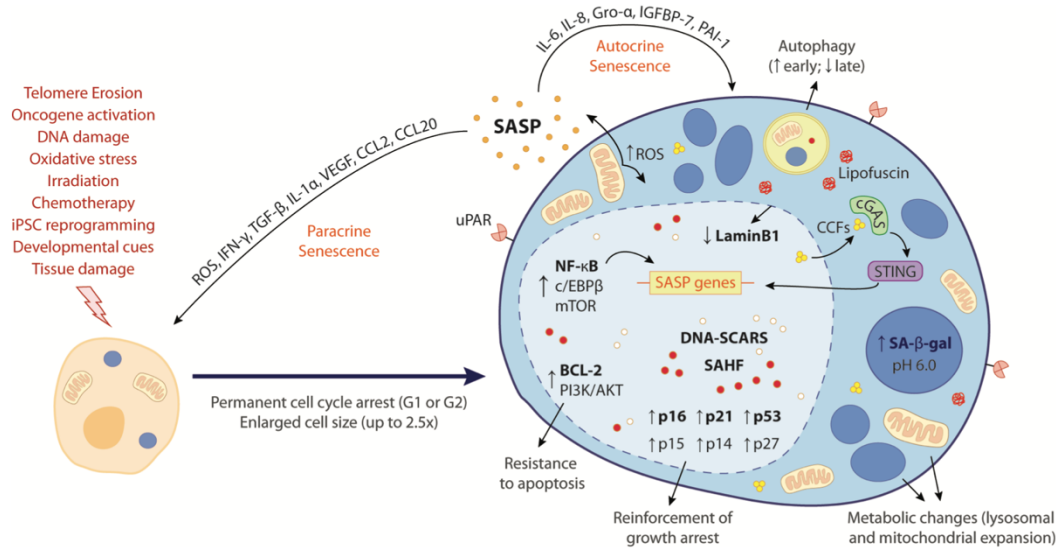

Figure 1.7. Hallmark features of cellular senescence. SeCs are enlarged in size, about 2.5 times its normal size. The cell undergoes permanent cell cycle arrest due to increased levels of inhibitors like p16INK4a and p21CIP1. It becomes resistant to apoptosis through enhanced BCL-2 and PI3K/AKT pathways. Metabolic shifts occur, with expanded mitochondria and lysosomes leading to increased reactive oxygen species (ROS) production. Senescence-associated β-galactosidase (SA-β-gal) activity rises, detectable at pH 6.0. ROS accumulation causes protein aggregation, forming lipofuscin aggresomes. Autophagy rates initially increase but become compromised in later stages. The cell develops a complex senescence-associated secretory phenotype (SASP), releasing various factors. Nuclear changes include lamin B1 downregulation, leading to chromatin extravasation. Chromatin undergoes remodeling, affecting DNA organization and gene expression. Bold text in the figure highlights the most common hallmarks of cellular senescence. From Paramos-de-Carvalho et al. (2021) [17]

Growth arrest

As mentioned above, cell cycle arrest is one of the hallmarks of senescence (Fig.8). SeCs undergo growth arrest at the G1 or G2 phase of the cell cycle[17]. Contrary to a quiescent state, this arrest is permanent and cannot be induced by physiological stimuli[21] SeCs also differ from terminally differentiated cells, which are also in a state of stable cell cycle arrest. In fact, senescence is induced by stress whereas terminal differentiation results from the activation of a specific genetic program. However, it has been shown that certain cell types known to be terminally differentiated can also develop a senescent phenotype[17]. For example, it has been shown that in a spinal cord injury context, a population of senescent neurons is induced upon injury [13]. Both p16 and p21 are amongst the most common markers used to identify SeCs. It has been proposed that p21 is important for the onset of cell cycle arrest and p16 for the perpetuation of growth arrest over time [21]. However, the presence of these CDKIs does not necessarily indicate senescence [18]. Cell cycle arrest is not exclusive to senescence, as p53 and RB

can participate in other contexts in which proliferation arrest occurs. Even p16, despite being one of the more robust senescent markers, is not present in all SCs and can also be expressed in non-senescent cells. Similarly, p21 activation does not always lead to senescence, as some tissues that exhibit other hallmarks of senescence may not be p21 positive [17], [18]. This highlights that there is a fine line between what is considered senescence and what is not; multiple hallmarks must be taken into account to accurately identify SeCs.

Apoptosis resistance

SeCs become resistant to apoptotic mechanisms. This is not only due to the up-regulation of anti-apoptotic pathways, such as anti-apoptotic phosphoinositide 3-kinase/protein kinase B (PI3K-AKT) but also due to the expression of anti-apoptotic proteins, such as anti-apoptotic B-cell lymphoma (BCL)-2 family proteins (BCL-2, BCL-xL). Additionally, epigenetic repression of pro-apoptotic proteins, such as BAX can also result in apoptosis resistance **(Fig.1.7)** [22], [23]. This resistance possibly explains why senescent cells remain stable in culture and why their number increases with age [21]. However, other non-senescent cells can also develop resistance to apoptosis, for example, blood cells, further reinforcing the idea that there are no exclusive hallmarks of senescence.

Morphological alterations

Some morphological features accompany the process of senescence. SeCs become enlarged in size and present multiple nuclei. When in culture, adherent SeCs adopt a flattened morphology and a non-specific orientation. There are also some changes at the organelle level. Overall, there is an increase in total organelle mass, the Golgi apparatus becomes more prominent and the cytoplasm vacuolated [19], [21]. Alterations in the cell morphology are not surprising, given the increase in RNA and protein content due to reduced RNA turnover, decreased protein degradation, and cell proliferative arrest [21].

Organelle dysfunction

Nuclear alterations

Senescence is accompanied by several nuclear changes. There is the formation of senescence-associated heterochromatin foci (SAHF), which are hotspots of DNA/chromatin condensation. In contrast to proliferating cells, that show a homogeneous 4′,6′-diamidino-2-phenyl-indole (DAPI) staining, SAHF can be detected by several fluorescent punctate [19], [21]. These specific heterochromatin structures are transcriptionally silent due to the association of chromatin-reorganizing proteins, including heterochromatin protein 1 (HP1) to the DNA, and histone modifications such as methylated lysine 9 on histone H3 (H3K9me). This allows the silencing of important proliferation genes, such as E2F-responsive genes cyclin A and E which are involved in cell cycle progression [19]. Additionally, during senescence, there is the loss of Lamin B1 (LMNB1), which is a structural protein of the nuclear lamina important for the maintenance of the nuclear architecture and stability [19], [21], [24]. The downregulation of LMNB1 also

promotes the formation of SAHF by allowing the reorganization of H3K9me-positive heterochromatin [21]. Nuclear instability, due to the loss of LMNB1, results in the formation of cytoplasmic chromatin fragments (CCFs). These fragments contain epigenetic traces of DNA damage and can be secreted via exosomes, thus inducing DNA damage responses in neighboring cells [19], [24]. LMNB1 reduction depends on the activation of p53 and p16, reflecting the complex interaction between different hallmarks of senescence [24]. Telomere shortening constitutes another nuclear alteration observed during this process. Short telomeres present DNA damage response factors such as γ -H2AX, these regions are referred to as dysfunction-induced-focus (TIF) [19].

Mitochondria

The accumulation of dysfunctional mitochondria is a reality when it comes to senescence, there is a higher mitochondrial mass, and mitochondria are enlarged in size. Senescent mitochondria present defects in the oxidative phosphorylation pathway. The electron transfer chain is the main site for ROS production, dysfunctions in this pathway result in ROS formation, which damages DNA, lipids, and proteins initiating a damage response that leads to oxidative stress underlying the senescent phenotype [25], [26]. Oxidative stress results in further DNA damage through oxidization of nucleotide bases and induction of single and double-strand breaks. This, in turn, promotes the activation of p53 and p16, creating a negative feedback loop that perpetuates cell cycle arrest. In addition, it has been suggested that dysfunctional mitochondria are also involved in the formation of CCFs possibly through ROS formation. Accumulation of defective mitochondria may be due to the cell's inability to control mitochondrial turnover through fission, fusion, and autophagic processes [27]. Normal mitochondria have dynamic fusion and fission mechanisms that allow the maintenance of mitochondrial homeostasis [19], [28]. In the context of senescence, fission cycles are downregulated, increasing the total mitochondrial mass. This may be a compensatory mechanism to counteract the decline of functional organelles observed in senescent cells. Additionally, this accumulation of damaged mitochondria may also be attributed to an impairment in the autophagic processes that compromise the formation of autolysosomes and reduce digestion [26].

Lysosome and Senescence-associated- β-galactosidase (SA-β-gal)

Lysosomes are the main catabolic organelles and suffer significant alterations during the senescence process. There is an increase in lysosomal mass and biogenesis, which increases the activity of the lysosomal enzyme β-galactosidase, encoded by the *glb1* gene. In SeCs, this activity can be detected at pH 6 in addition to optimal pH 4 in normal cells **(Fig 1.8)** [21], [24], [29]. Bearing this in mind, the most extensively used senescence biomarker is born, senescence-associated β-galactosidase (SA-β-gal), which reflects the increase in lysosomal content associated with senescence. The increase in size and volume of lysosomes can also be seen by the presence of lipofuscin in lysosomes, which is a fluorescent pigment that is indigestible, remaining retained in the lysosomes [19], [21], [24], [30]. In contrast to senescent cells, proliferating cells do not accumulate lipofuscin because it is diluted within each cell division [21]. It has been shown that lipofuscin accumulation induces the expression of BCL-2, promoting apoptosis

resistance [26]. Once again reflecting the complex interplay between the hallmarks of senescence. Nevertheless, high lysosomal activity is not a specific requirement to senescence, as some SeCs may not be positive for SA-β-gal. In addition, some non-senescent cells, such as macrophages, can exhibit high lysosomal activity and thus be SA-β-gal positive [17], [24].

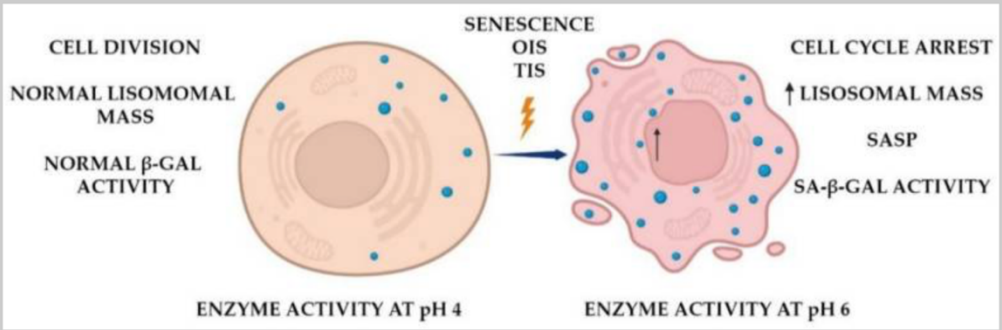

Figure 1.8.Lysosomal alterations upon senescence. β-galactosidase is active in the majority of cells at pH 4, indicating their normal state. Senescent cells accumulate pH 6 active β-galactosidase, undergo cell cycle arrest, and obtain senescence-associated secretory phenotype (SASP) overexpressing the GLB1 gene. From Valieva Y et al. (2022) [29]

Endoplasmic reticulum (ER)

During senescence, there is an increased demand for protein synthesis and correct folding, which places significant stress on the ER [26]. In response to this stress, the cell activates the Unfolded Protein Response (UPR) to prevent the accumulation of unfolded or misfolded proteins. When cells cannot cope with this stress, autophagy mechanisms are activated by the UPR. In SeCs, the activation of this response results in the decrease of protein synthesis, expansion of the ER, and export of misfolded proteins. However, in an established senescence state autophagy mechanisms are impaired, contributing to protein damage, the presence of aggregates, and abnormal protein synthesis [24], [26]. Autophagy has a dual role in senescence. In the early stages, the autophagy rate is increased, due to the cell cycle arrest, as CDKIs have been shown to promote autophagy. However, once senescence is established, autophagy is impaired, due to the cell's detrimental environment, such as oxidative stress. This, in turn, contributes to further loss of proteome homeostasis, and mitochondrial dysfunction **(Fig.1.7)** [17], [31].

Senescence-associated secretory phenotype (SASP)

Senescent cells have the potential to develop a secretory phenotype, known as senescence-associated secretory phenotype (SASP), which is likely one of the most important hallmarks of senescence [17]. Due to its complex nature and significance, it will be described further in the subsequent subsection.

1.3.2 SASP

Despite being in a state of proliferative arrest, SeCs remain metabolically active and modify their secretome by producing cytokines, interleukins, chemokines, proteases, growth factors, degradative enzymes such as matrix metalloproteases (MMPs), insoluble proteins and extracellular matrix (ECM) components **(Table 1.1)** [17], [21]. These SASP molecules impact the tissue microenvironment mediating senescence-associated pathophysiological events [20], [26]. SASP factors can act in two distinct manners: autocrine and paracrine. In an autocrine context, SASP molecules such as IL-6, IL-8, growth-regulated oncogene alpha (Gro)-α, insulin-like growth factor-binding protein (IGFB)-7, and plasminogen activator inhibitor (PAI)-1 reinforce the cells' own senescence. In parallel, in paracrine senescence, senescent cells induce senescence in nearby cells through the release of ROS, IFN-γ, transforming growth factor beta (TGF-β), IL-1α, vascular endothelial growth factor (VEGF), chemokine (C-C motif) ligand 2 (CCL2), and 20 (CCL20) [17], [20].

Table 1.1- Senescence-Associated Secretory Phenotype (SASP) factors. From Gorgoulis *et al.* (2019)[27]

Class	Component
Interleukins	IL-6; IL-7; IL-1; IL-1b; IL-13; IL-15
Chemokines	IL-8; GRO-a, -b, -g; MCP-2; MCP-4; MIP-1a; MIP-3a; HCC-4; eotaxin; eotaxin-3; TECK; ENA-78; I-309; I-TAC
Other inflammatory molecules	TGFβ; GM-CSE; G-CSE; IFN-γ; BLC; MIF
Growth factors; regulators	Amphiregulin; epiregulin; heregulin; EGF; bFGF; HGF; KGF (FGF7); VEGF; angiogenin; SCF; SDF-1; PIGF; NGF; IGFBP-2, -3, -4, -6, -7
Proteases and regulators	MMP-1, -3, -10, -12, -13, -14; TIMP-1; TIMP-2; PAI-1, -2; tPA; uPA; cathepsin B
Receptors; ligands	ICAM-1, -3; OPG; sTNFRI; sTNFRII; TRAIL-R3; Fas; uPAR; SGP130; EGF-R
Non-protein molecules	PGE2; nitric oxide; ROS
Insoluble factors	Fibronectin; collagens; laminin

Data are based on Coppé et al. (2010).

Due to the complex nature of SASP, a fundamental question is raised, how is SASP induced? Persistent DNA damage is highly observed in the senescence process, and it has been suggested that this leads to the reduction of histone-demethylating enzyme G9a expression. The lack of expression of this enzyme promotes a more accessible chromatin structure, which facilitates the expression of SASP genes. Furthermore, among the wide spectrum of nuclear changes observed in SeCs, the presence of CCFs described in the section above has an important role in SASP induction. CCFs can translocate to the cytosol where they accumulate and activate the DNA sensor cyclic GMP-AMP synthase-stimulator of interferon genes (cGAS-STING). The cGAS induces the production of the second messenger cyclic di-nucleotide, cyclic GMP-AMP (cGAMP). The cGAMP is recognized by the adaptor protein STING that triggers the type 1 interferon-producing pathway through the activation of IRF3 or nuclear factor kappa B (NF-κB) **(Fig.1.9)** [20]. This activation triggers innate immune responses and the release of SASP factors mainly pro-inflammatory cytokine production through NF-κB [17], [32]. The described process occurs not only because CCFs can travel to the cytosol but also due to their accumulation. In normal conditions, DNases, such as DNase2, would be responsible for degrading these cytoplasmic fragments, however, SeCs have a downregulated expression of such DNases allowing the buildup of CCFs and consequent cGAS-STING pathway activation[20].

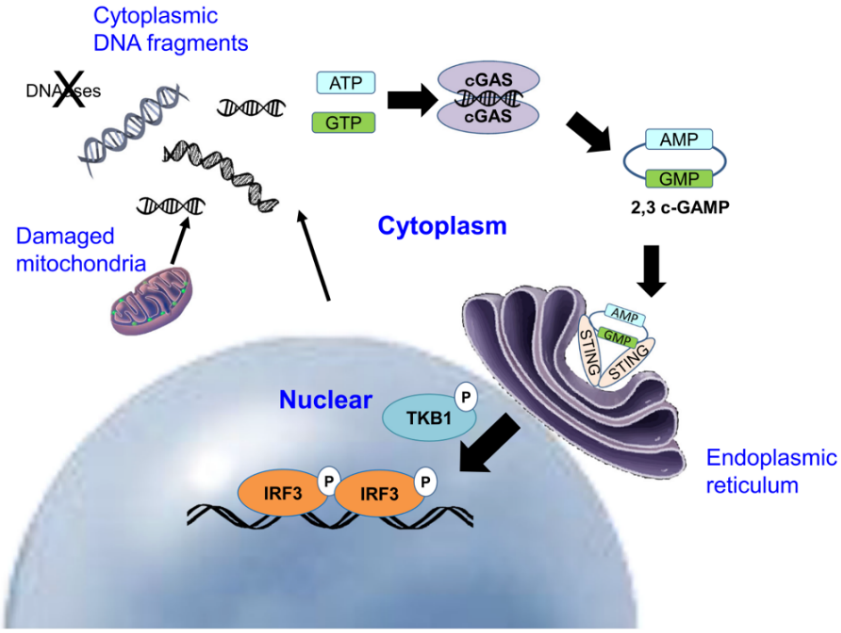

Figura 1.9. cGAS-STING - Intrinsic pathway of SASP induction. SeCs accumulated cytoplasmic DNA fragments. The DNA sensor cGAS binds these fragments, producing cGAMP, which activates STING. This triggers a cascade resulting in increased production of type I interferons and other SASP factors. From Naoko Ohtani (2022) [20]

SASP factors can have both beneficial physiological effects and pathological effects, making them a double-edged sword. The impact of these effects depends heavily on the specific context, as we will further explore in the following section. Additionally, there is an emerging concept that the role of SASP is a time-dependent process. SASP can have a transient or persistent profile **(Fig.1.10)** [17]. Beneficial effects are typically associated with transient SASP responses. In this context, SASP factors can promote the recruitment of immune cells to eliminate damaged cells from the lesion site and clear SeCs thereby preventing their accumulation. For instance, SASP factors released by senescent fibroblasts in injured skin facilitate the recruitment of immune cells to remove damaged tissues. Additionally, the growth factors released as SASP factors can stimulate the proliferation of skin progenitor cells, giving rise to new tissue. Afterwards, immune cells clear the senescent fibroblasts, thus creating a transient profile that positively influences tissue repair and regeneration[17], [33]. Similar events happen following hepatic injury, where SASP factors are produced by senescent hepatic stellate cells (HSCs), immune cells are recruited, and senescent HSCs are then eliminated preventing fibrosis caused by excess collagen production [20]. Adding to the beneficial effects, SASP factors can have a role in cell-fate reprogramming. For instance, during organ development in mammals, SeCs emerge transiently. This short-term appearance facilitates the differentiation of surrounding cells and the removal of unnecessary ones. The involvement of SASP in the development and repair of damaged tissues exemplifies some of the physiological roles of SASP [17], [20], [26], [32]. In contrast, long-term SASP can have deleterious effects by promoting proliferation, angiogenic, pro-inflammatory, and pro-fibrotic responses. For example, it has been shown that proteases, such as MMPs (1/2/3/7/8/9/13), secreted by SeCs may contribute to an

impairment in immune surveillance and immune clearance, thus resulting in deleterious and pro-tumorigenic effects. Interestingly, there is a link between proteases and inflammation creating a positive SASP feedback loop. As mentioned, SASP can recruit inflammatory cells such as neutrophils and mast cells. These cells secrete extracellular proteases, that in turn activate precursors of the IL-1 family, and the loop is established [32]. Also, in cases of persistent damage or aging, there is an increase in the number of SeCs, leading to chronic inflammation and fibrosis via persistent SASP [34]. The dichotomy between beneficial and detrimental SASP is challenging to define, but "time" seems to play an important role in regulating senescence and SASP effects.

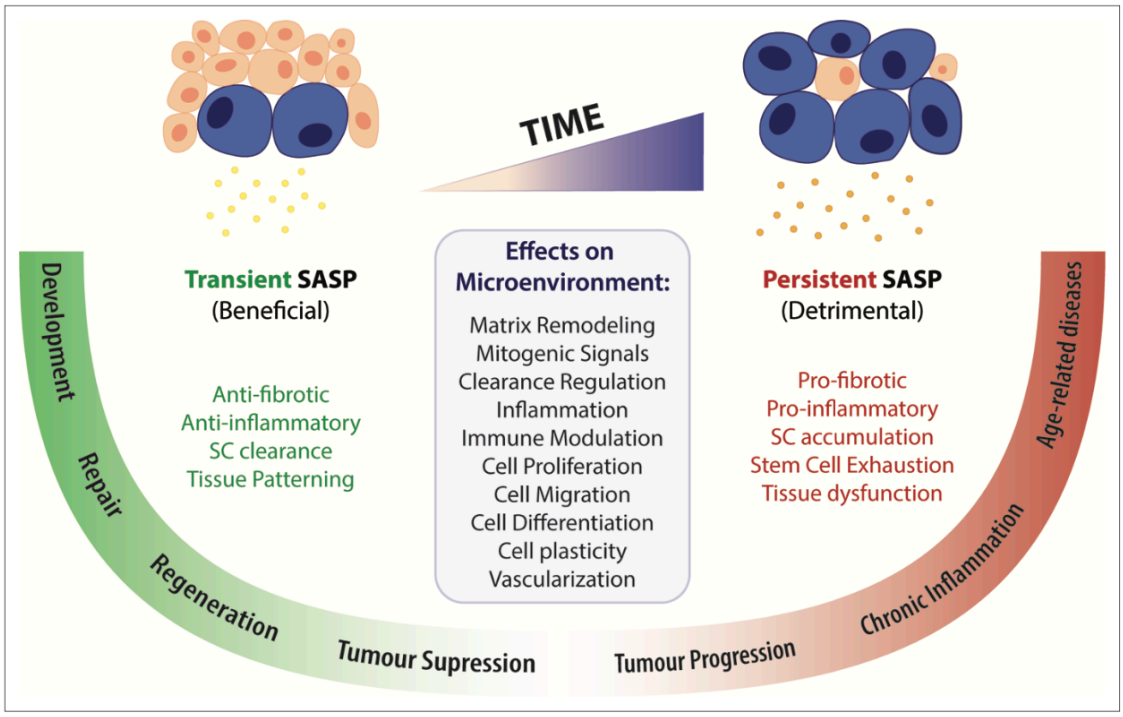

Figure 1.10. Time-dependent effects of SASP. Transient SASP responses can lead to beneficial outcomes such as tissue repair, immune clearance of senescent cells, and developmental patterning. In contrast, persistent SASP responses are linked to detrimental effects, including chronic inflammation, tissue dysfunction, and depletion of stem cell pools. From Paramos-de-Carvalho et al. (2021) [17]

1.3.3 A multiparametric approach is needed to identify SeCs

Senescence is a highly dynamic and heterogeneous process. The manifestation of the different hallmarks depends on the context, cell type, tissue, time at which senescence was initiated, and the stressor that triggered the pathway. Due to the lack of a specific marker to exclusively identify senescence, it is essential to move from a single-parameter approach to a multiparametric methodology. This approach should include the assessment of SA-β-gal activity and/or the accumulation of lipofuscin. However, as previously indicated, SA-β-gal activity is not unique to SeCs, making it necessary to include cell cycle regulators such as p16 and p21 in the analysis. To identify senescent cells more accurately, it is important to investigate additional factors that may be altered as a result of senescence [17], [26], [27].

The heterogeneity of senescence and the absence of specific markers present a significant knowledge gap. Advanced technologies, for example, RNA sequencing (RNA-seq)-based approaches, such as bulk RNA-seq using next-generation sequencing, can simultaneously detect thousands of RNA transcripts. This technological advancement enables a more accurate identification and characterization of SeCs, also holding the potential to uncover novel senescence marker candidates. Bulk RNA-seq data from human and mouse fibroblasts already uncovered differences in the transcriptomic profiles and SASP molecules which were dependent on the trigger of senescence, cell type, and the stage of senescence [18]. High-throughput technologies may be a powerful ally in this multiparametric workflow, enhancing our understanding of senescence and helping us define its identity.

1.3.4 Role of senescence

Given its heterogeneous nature, it is not surprising that the roles of senescence are not always consistent and greatly context-dependent. This section will focus on uncovering the roles of senescence in development, wound healing, and regeneration.

Embryogenesis and Development

SeCs are found in mice, humans, naked mole rats, amphibians, birds, fish embryos, and larvae. In the mammalian embryo, senescence is observed in several structures such as limbs, the nervous system, and the gut endoderm. In the developing kidney, SeCs accumulate and recruit immune cells, such as macrophages, that then phagocytize SeCs in the site, allowing mesonephros regression. Incredibly, senescent decidual cells in the endometrium of female mammals can secrete factors that facilitate embryonic implantation by creating a favorable environment [35]. SeCs in embryonic structures are SA-β-gal positive and exhibit increased activity of p21 without p53 or p16 expression, indicating differences between developmental senescence and mature tissue senescence [17], [33]. It is worth noting that developmental senescence does not seem to involve DNA damage response pathways, as no DNA damage or DNA damage pathway markers were observed in SeCs. p21 appears to be extra relevant in developmental senescence, as disruption of p21 leads to the loss of the senescence phenotype allied with patterning and morphological abnormalities [17], [36]. However, senescence plays a short-term role in development. For instance, when patterning defects are noticed during development, they are compensated by other pathways, such as apoptosis [17].
In conclusion, SeCs are involved in the remodeling of developing tissues and structures through several mechanisms, but they do not seem to play a long-term role.

Wound healing and regeneration

Wound healing is a multifaceted process involving inflammation, new tissue formation, and fibrosis. Research has indicated that senescence responses are triggered upon injury [33], [35]. The impact of these responses can vary; they may have a dual effect, beneficial or harmful, depending on the specific context and duration. For example, the skin is able to regenerate upon an injury. When a cutaneous wound is performed, there is the release of a matricellular protein CCN1, which activates p16 and p53,

thus inducing senescence in fibroblasts and myofibroblasts. These senescent cells activate DNA damage responses and p16-ROS signaling, which in turn controls fibroblast proliferation and ECM deposition limiting fibrosis [17], [34], [37]. Also in the skin, using the P16-3MR model, Demaria et all showed that upon injury there is a transient accumulation of senescent fibroblasts and endothelial cells that produce platelet growth factor AA (PDGF-AA) inducing myofibroblasts proliferation. Selective elimination of p16- positive ($p16^{+}$) cells impaired the wound healing processes and led to increased fibrosis. However, it was also reported that PDGF-AA may not be the main player since topical administration of PDGF-AA was able to revert the delay in wound closure but did not reduce fibrosis [17], [34], [37]. In a contrasting view, it has been shown that upon cardiac ischemia-reperfusion injury, senescence is also induced. However, in this case, it contributes to a prolonged oxidative stress response on cardiomyocytes and endothelial cells, subsequently leading to fibrosis and the production of pro-inflammatory SASP, ultimately impairing cardiac function. Current literature has suggested that damage-induced senescence represents a positive effect on wound healing by promoting cell proliferation, differentiation, and immune cell recruitment. Moreover, the elimination of SeCs using pharmacological or genetic approaches seems to hinder the regenerative processes. However, to avoid a detrimental effect, senescence induction needs to be limited in time and duration. When senescence is induced above physiological levels or when SeCs are not effectively eliminated, it appears to exacerbate fibrosis in the wounded tissue **(Fig.1.11)** [17], [33].

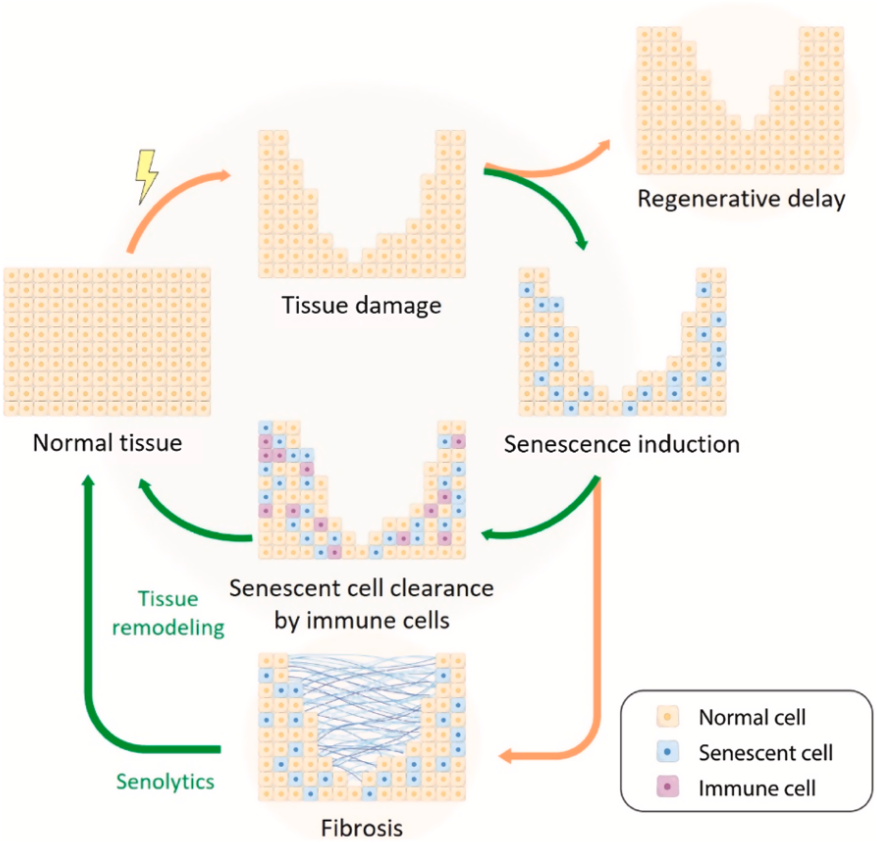

Figure 1.11- Dual-role of senescence in tissue remodeling. Following tissue damage, the induction of cellular senescence can support regeneration and repair. When senescent cells are effectively cleared by the immune system, the tissue can return to its normal state. However, if clearance is ineffective, the senescence-associated secretory phenotype (SASP) can contribute to fibrosis, leading to impaired tissue repair. Administering senolytic drugs may reverse this phenotype by eliminating senescent cells from the tissue. From Antelo-Iglesias et al. (2021) [33]

SeCs have also been recently linked with regeneration. In the salamander, upon limb amputation, senescence is transiently induced near the amputation site during regeneration and then SeCs are cleared by macrophages. Moreover, in injured hearts of zebrafish and neonatal mice, senescent SA-β-gal positive fibroblasts were also shown to be transiently induced upon injury. In contrast, in the mouse model of biliary injury, persistent senescence induction showed detrimental outcomes. Secretion of TGF-β by cholangiocytes and hepatocytes was shown to induce paracrine senescence on surrounding cells having a negative impact on the local microenvironment, hindering liver regeneration. When TGF-β signaling was inhibited, senescence was not propagated, collagen deposition was reduced, and liver function was restored. In conclusion, as in wound healing, in regeneration one must also consider the dual role of persistent versus transient senescence [17], [34].

1.3.5 Targeting senescence

Literature has shown that SeCs are induced following injury/tissue damage, and that persistent senescence has detrimental consequences. Therefore, interventions aimed at targeting cellular senescence seem to be an appealing strategy, the so-called senotherapeutics. These interventions encompass a variety of approaches, including senolytics, which selectively eliminates senescent cells, and senomorphics, which inhibits its SASP. Additionally, there are exogenous cell-based products and non-pharmacological methods **(Table 1.2)**.

Table 1.2- Senotherapeutic strategies from Gorgoulis *et al*. (2019) [27]

Senotherapeutic approach	Type	Examples	Refs.
Senolytic interventions	Apoptosis inducers	Quercetin, AP20187, navitoclax, A-1331852, A-1155463, EF24 and venetoclax, antibody-engineered toxic drugs, ginsenoside	6,186,217,225,230,231,235
	Immunotherapies	Chimeric antigen receptor T cells, activator of invariant natural killer T cells, vaccines targeting GPNMB (which is overexpressed in senescent cells)	236–238
Senomorphic drugs	SASP regulators	Metformin, ruxolitinib, rapamycin, resveratrol, melatonin, androgen, oestrogen, oestradiol, glucocorticoids	239,243,244,247,250,254–257
Stem cells and their products	Stem cells	Bone marrow MSCs, pluripotent stem cells, umbilical cord-derived MSCs	258,259,261
	Stem cell-derived extracellular vesicles	MSC-derived extracellular vesicles, dental pulp stem cell-derived extracellular vesicles, antler stem cell-derived extracellular vesicles	262,264,282
Non-pharmacological therapies	Lifestyle interventions	Habitual moderate exercise, healthy diet, calorie restriction	268,269,271,273
	Others	Fractional micro-needling radiofrequency treatment, radio-electric asymmetric conveyer technology	234,275

MSC, mesenchymal stem cell; SASP, senescence-associated secretory phenotype.

For the scope of this dissertation, the primary focus will be on senolytics. The mechanism of action of senolytics is to induce pre-programmed cell death, circumventing apoptosis resistance pathways that are typically exhibited by SeCs. These compounds target pathways and mechanisms that are upregulated in senescent cells, which otherwise allow them to evade apoptosis and accumulate, thereby contributing to aging and various age-related diseases [17], [35]. Senolytics are the primary type of intervention used for the elimination of SeCs. Examples of senolytics include Dasatinib, Quercetin, and Navitoclax (also known as ABT-263) [17]. Dasatinib and Quercetin were among the first set of senolytics used. A combinatorial approach of these two senolytics led to a decrease in p16 expression, tissue function was improved and healthspan was extended in aged and progeroid mice [17], [20], [23]. In our lab, we observed that, upon SCI, senescence is induced; however, zebrafish and mice, representing regenerative and non-regenerative models respectively, display distinct senescence profiles [13]. In zebrafish, there is a transient accumulation of SCs at the lesion periphery, which subsequently return to basal levels. Conversely, in mice, SeCs are not only induced upon injury but also accumulate over time. In both models, the SeCs at the lesion periphery were predominantly SA-β-gal positive cells, with the majority being neurons. Injured mice were treated with Navitoclax (ABT-263) within the first 14 dpi, during which the BSCB remains leaky, allowing free access to the CNS [13]. ABT-263 is a potent senolytic

that inhibits BCL-2/BCL-xL, thereby inducing apoptosis in SeCs and allowing their effective elimination in injured mice [13], [17], [23], [35]. By targeting SeCs in the mouse SC and preventing their accumulation upon injury we were able to promote the recovery of locomotor, sensory, and bladder functions. Additionally, improvements in myelin preservation and axonal growth were observed. Furthermore, ABT-263 treatment reduced pro-fibrotic and pro-inflammatory components in the injured SC, leading to less fibrosis and inflammation [13].

1.3.6 p16 in senescence, aging and beyond

While p16 is recognized as a key hallmark of senescence, its function extends beyond this role. The p16 gene also referred to *CDKN2 gene* is located on the short arm of the chromosome (9p21.3), in humans. This gene encodes for two proteins, p16Ink4A and p14ARF (p19ARF in mice). As previously highlighted, p16 is intrinsically related to senescence, acting as a cell cycle regulator that mediates cell cycle arrest, which is a pivotal component of the senescence process. p16 is also recognized as a hallmark of aging and age-related diseases, notably due to its elevated expression in the tissue of aged rodents, including the lungs, lymph nodes, adrenal glands, and uterus. Additionally, the targeted removal of p16-positive cells has been shown to not only slow the progression of age-related diseases *in vivo* in mice but also to extend their lifespan [34]. Beyond its canonical functions, p16 suppression has been shown to promote tumor development, unveiling the p16 role as a tumor suppressor. Mutation or promotor methylation of the p16 gene is linked to a vast variety of cancers, such as familial or sporadic melanoma. Furthermore, p16 can be a melanoma predictive and prognostic marker, with lower levels being associated with higher proliferation, as indicated by Ki67, a proliferative marker. Metastatic melanoma is associated with even lower p16 levels, correlating with a poor prognosis [34]. Moreover, in the bone of osteosarcoma patients, lower expression of p16 was correlated with a reduced response to primary chemotherapy. An increase in p16 expression has also been observed in an injury context. For example, upon Acute muscle injury (AMI), fibro-adipogenic progenitors (FAPs) exhibit a transient upregulation of p16. Moreover, p16 loss was linked with poor survival upon lung injury. In fact, p16 expression was found to protect the lung epithelium against lung injury. Injured p16-positive mesenchymal cells promoted epithelial progenitor proliferation, whereas p16 deletion in the lungs attenuated normal epithelial repair. In the case of the injured heart, after myocardial infarction, p16 overexpression has been detected in the injured zone. This upregulation was associated with the protection of cardiac function and the promotion of cardiac remodeling. [34] p16 has also been implicated in stem cell renewal and differentiation processes, however, this expression needs to be tightly regulated for these processes to occur correctly. For example, p16 repression by epigenetic mechanisms allows stem cell proliferation. In keratinocytes, the primary cell type found in the outer layer of the skin, p16 needs to be expressed in a highly regulated and orchestrated manner, alongside other differentiation genes, for proper differentiation to occur. In fact, Id-1, Id-2, and Id-3 are negative regulators of p16 that are upregulated in dividing keratinocytes, still in the growth phase, and become downregulated in differentiated cells [38]. This shows that the role of p16 in stem cell renewal and differentiation is highly context-dependent, it needs to be repressed to allow stem cell renewal but needs to be expressed in a regulated

manner for the differentiation of cells like keratinocytes [34] [38]Altogether, data shows that p16 is much more than a senescence marker. It has several roles in aging, tumor suppression, stress, stem cell renewal, and cell differentiation, among others. Additionally, its functions are context and tissue-dependent.

1.3.7 p16-FDR mouse model

The p16-FDR mouse line was developed by Haston et al. and kindly provided by our collaborator Juan Pedro Martinez-Barbera (University College London, Developmental Biology and Cancer, Birth Defects Research Centre, United Kingdom) [39]. This model was generated by inserting a bicistronic *FDR* cassette in the 3' end of the Cdkn2a (p16) locus using CRISPR/Cas9 **(Fig. 1.12)** [40]. For this, a multicistronic vector was generated, which contains a mammalian optimized FLP recombinase, and a diphtheria toxin receptor (DTR) fused with mCherry fluorescent reporter - hence the name FDR (Flipase, Diphtheria toxin receptor, and Reporter). This vector also contains P2A sequences upstream and downstream of the FLP-recombinase, facilitating ribosomal skipping during mRNA translation and the generation of multiple protein products (p16, FLP, and DTR-mCherry). This cassette is flanked by two sequences homologous to regions 2.5 kb upstream and 1.9 kb downstream of the $p16^{INK4A}$ protospacer adjacent motif (PAM) site. Therefore, this construct allows the expression of a FLP-recombinase and a diphtheria toxin receptor-mCherry fusion construct under the control of the p16 promotor [39].

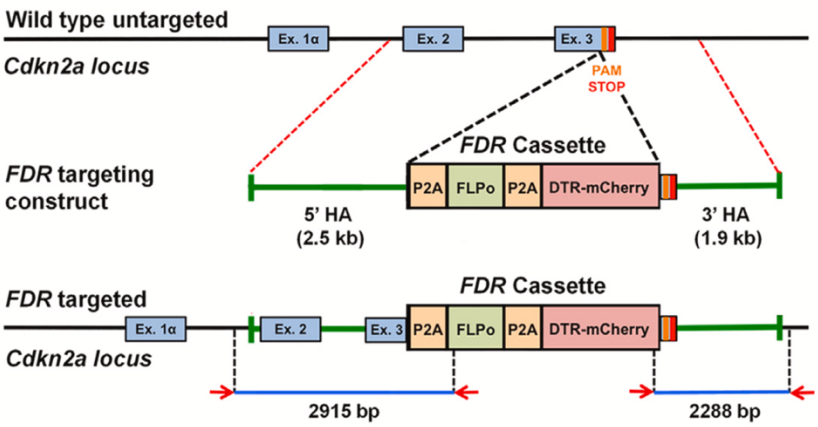

Figure 1.12. Schematic representation of the FDR cassette inserted into the Cdkn2a locus via CRISPR-Cas9. The FDR cassette includes a Flipase (FLP) region flanked by two P2A sites, enabling ribosomal skipping. It also contains the diphtheria toxin receptor followed by an mCherry reporter protein. At the end of the cassette, a Protospacer Adjacent Motif (PAM) allows Cas proteins to recognize and bind to the genomic DNA. The cassette was inserted after exon 3 of the Cdkn2a locus, ensuring proper transcription of Cdkn2a transcripts along with the FDR cassette. From Haston et al. (2019) [40]

The way this transgenic line was built not only allows the direct visualization of p16-expressing cell populations, through the expression of mCherry reporter but also its effective pharmacogenetic elimination through diphtheria toxin (DT) administration. Lastly, this line also allows for lineage tracing of

p16-expressing cell populations, though not explored in this dissertation. For this work, we used heterozygous (p16FDR/+) and wild-type p16-FDR (wt p16+/+) mice for experimental settings, while maintaining homozygous (p16FDR/FDR) mice as breeding pairs to ensure the continuity of the transgenic line. This approach was chosen due to an early lethality rate and a higher incidence of spontaneous tumorigenesis, particularly in the liver and spleen, registered in homozygous animals (**Fig.1.13)** [39].

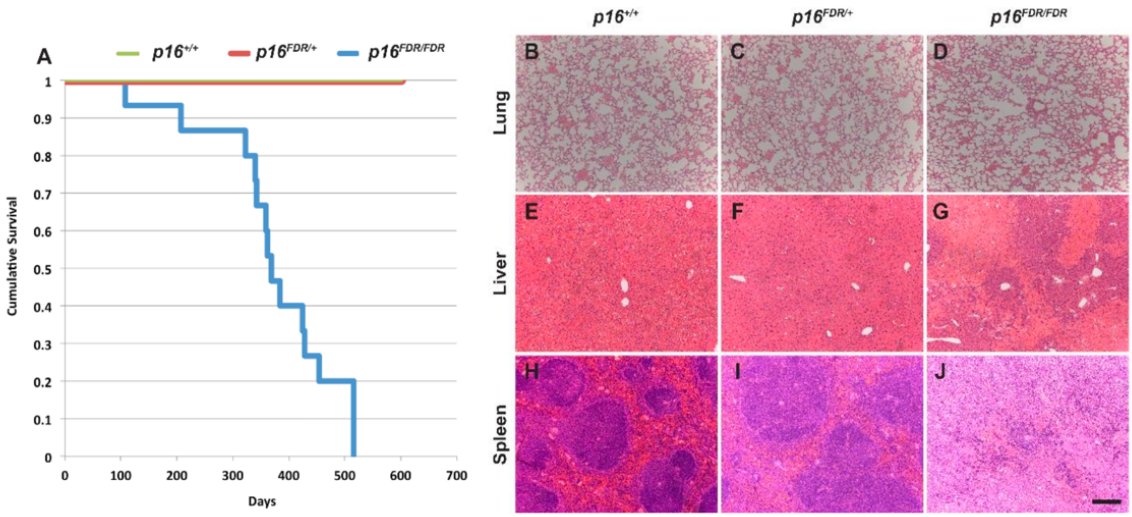

Figure 1.13. Homozygous p16FDR/FDR animals exhibit early lethality and increased tumor incidence. On the left, the survival curve compares p16+/+, p16FDR/+, and p16FDR/FDR animals, showing early lethality in p16FDR/FDR mice, reaching to 0% survival by 600 days. On the right, spontaneous tumors are observed in the lungs, liver, and spleen of p16FDR/FDR animals, which are absent in their littermates. From Haston et al. (2019) [40]

1.4 Models of SCI

1.4.1 Mammalian animal models

In vivo models in SCI research have significantly advanced our comprehension of pathophysiological and recovery mechanisms and allowed the development of potential therapeutic interventions [41]. However, it is important to note that animal models of SCI do not perfectly replicate the complex nature of human SCI. When selecting an animal model, it is crucial to consider the scientific objectives, the ability to replicate the complex nature of SCI pathophysiology, and the model's availability and reproducibility. Equally important are animal welfare considerations, including minimizing and avoiding suffering, and accordance with the 3R principles: replacement, reduction, and refinement [42], [43]. For the past 30 years, rodent models have been extensively utilized and remain the most commonly used species in SCI scientific research, due to their availability and easy maintenance [43]. Rat models are favored due to their ease of care, cost-effectiveness, and well-studied anatomy. Additionally, surgical infections are relatively rare in these models and functional analysis techniques are well established. Rat models also exhibit notable similarities to human spinal cord injuries regarding alterations in

function, electrophysiology, and morphology [41], [43], [44]. Specifically, both rats and humans, develop large cystic cavities at the injury site, whereas in mice, this cavity is filled with dense fibrotic tissue [41]. On the other hand, mouse models are particularly advantageous for genetic studies, as establishing genetic rat models is considerably more challenging [41]. Mice have a similar genome to humans, they are easy to handle, cost-effective for use and maintenance, and possess high reproductive rates. Therefore, mice are also extremely useful for SCI studies.
The spiny mouse (*Acomys*) has become an intriguing model for studying tissue regeneration, particularly due to its remarkable ability to heal skin injuries without scarring. In the context of SCI, *Acomys* exhibits unique responses when compared to standard laboratory mouse models (*Mus musculus*, namely the C57BL/6 strain). This includes the upregulation of genes associated with neurogenesis, accelerated bladder function recovery, and a significant reduction in fibrotic tissue formation. These exceptional regenerative capabilities position *Acomys* as a promising mammalian model for investigating adaptive responses following SCI [45]. Large animal models including canine, porcine and non-human primate models can also be used in SCI scientific research. Non-human primates are particularly relevant due to their close genetic resemblance to humans, and similarities in spinal cord length and caliber, as well as their physiological and biological responses to injury. Utilizing large mammals enhances the potential for successful translation from laboratory findings to clinical applications, owing to their greater similarity to human spinal cord injuries. However, the use of these animals is limited by high maintenance and operational costs, the need for specialized infrastructures, and significant ethical considerations [41], [43], [44].

1.4.2 Experimental injury models

Spinal cord injury models are typically categorized into contusion, compression, and transection [46]. Among these, transection and contusion models are the most frequently utilized [9]. The transection model involves either a full transection or a hemisection of the spinal cord using a sharp instrument. Hemisection is often preferred because it preserves the integrity and function of one side of the spinal cord. In these models, the severed spinal cord can either be left *in situ* or a small section can be removed to allow for the implantation of a specific device [46]. While this model is not commonly observed in clinical human cases, and thus may not perfectly replicate the pathophysiology of SCI, it is relevant for studying axonal regeneration and functional recovery [43], [44], [46]. In a contusion model, a transient blunt force is applied to the exposed spinal cord, causing damage and displacement [44], [46]. Various methods, such as weight drop, electromagnetic, and air pressure devices, can be utilized to induce this type of injury [44], [47]. This model is often achieved by using an impactor, such as the Infinite Horizon (IH) impactor, which is a computer-controlled instrument that employs a force-controlled impact. The IH impactor allows the measurement of injury severity by measuring and monitoring biomechanical parameters like impulse, velocity, power, and energy. Notably, it is the first device capable of producing reproducible injuries without prior contact with the spinal cord, thus mitigating pre-impact trauma [43], [44], [46]. The contusion model is particularly valuable because it closely mimics the complex pathophysiological events following SCI. These events encompass hemorrhagic necrosis, ischemia, inflammation, and eventually the formation of a chronic lesion encapsulated by a glial scar [47]. However, this

model also has limitations. Distinguishing between spared and regenerated tissue is challenging, and variability in the use of clamps to firmly secure the spinal cord during the IH procedure can affect the consistency of the results [43], [46]. In the compression model, the spinal cord undergoes compression over a predetermined period. This model can be established using various techniques, including a modified aneurysm clip, forceps, a compression balloon, or clip compression methods [43], [44], [46]. By adjusting the compression strength, duration, or both, researchers can recreate different severity levels of SCI. This model effectively mirrors key stages observed in SCI, such as early hemorrhagic necrosis and edema, followed by partial repair and reorganization. Culminating in the chronic phase characterized by axonal atrophy and glial scar formation [46]. Commonly, hybrid models—such as contusion-compression models—are employed, where an acute impact is succeeded by sustained spinal cord compression [44]. Each of these models present unique advantages and limitations, and none perfectly replicates the intricate pathophysiological events of human SCI [46]. Therefore, the selection of an appropriate model should be dictated by the specific objectives of the study, alongside the particular considerations and available resources for the research [44].

1.5 The aim of this study

As previously mentioned, published data from the lab revealed that upon a spinal cord injury (SCI), senescent cells are induced and persist over time, having devastating consequences to the tissue. p16 is a known marker of senescence, however, its expression did not follow the same tendency as other senescent cell populations and not much was known regarding this population. We aimed to perform a phenotypic characterization of these p16-mCherry-positive cells using a new p16-FDR mouse line. For a more comprehensive cellular characterization, we began by optimizing a robust single-cell spinal cord dissociation protocol for flow cytometry and fluorescence-activated cell sorting (FACS). With an established protocol we aimed to characterize this population through flow cytometry using a wide variety of cell surface markers that would represent both recruited cells and resident cells in the spinal cord. To confirm and expand previous results we aimed to characterize this population with standard techniques such as immunohistochemistry. To assess a possible functional role of the p16-mCherry population we performed their selective elimination and evaluated locomotor outcomes. Additionally, the transient profile of the p16-mCherry population, made us question the canonical senescence nature of these cells. Therefore, we aimed to investigate the effects of the senolytic drug ABT-263 on the p16-positive population. Finally, with the optimization of a FACS protocol we wanted to know the transcriptomic profile of FACS-sorted mCherry-positive cells after spinal cord injury using bulk RNA sequencing to identify gene expression profiles and potential functional roles of this population, possibly adding to previous findings. Ultimately, through an integrated approach, we aimed to characterize the p16-mCherry population.

1.6 Contributions to this project

Our Project had 4 main tasks; **(1) Optimize a spinal cord single-cell dissociation protocol suitable for Flow cytometry; (2) Unravel the identity of p16-mCherry-positive cells through Immunohistochemistry and Flow cytometry; (3) Perform an ABT-263 study in the p16-FDR mouse model to find out if the p16-mCherry-positive cells are being eliminated by this senolytic drug and how they compare with the SA-β-gal population;** In the latter task, all of our main results are mentioned in this thesis. Regarding this task, I had an active role in all of the surgeries, and animal care, provided assistance in the drug administration, and performed behavioral analysis. Immunohistochemistry staining and data analysis were performed by Ana Isidro (PhD student) as also part of her PhD project. Materials and methods regarding these techniques are thus not included in this thesis. **(4) Sort p16-mCherry positive cells and access their transcriptomic profile to identify gene expression profiles and potential functional roles of this population, through bulk RNA sequencing.** Data analysis of our bulk-RNA sequencing data was performed by our lab bioinformatician Daniel Ribeiro (PhD). Details on this analysis are not depicted in this dissertation. Adding to these main 4 tasks I also participated in the p16-mCherry cell ablation protocol, during this project, I aided in all of the surgeries, animal care, assisted in drug administration, and performed behavioral analysis. Immunohistochemistry staining and data analysis were performed by Ana Isidro (PhD student) as also part of her project and thus the respective methodology is not depicted in this dissertation.

2 MATERIALS & METHODS

2.1 Ethics Statement

All procedures for handling, surgery, and post-operative care were approved by the Instituto de Medicina Molecular Internal Committee (Orgão de Bem-Estar e Ética Animal - ORBEA) and the Portuguese Animal Ethics Committee (Direção-Geral de Alimentação e Veterinária - DGAV) and were performed by a user licensed by DGAV. These procedures are in accordance with the European Community guidelines (Directive 2010/63/EU) as well as the Portuguese national legislation on animal care (DL 113/2013). Every effort was made to reduce the number of animals used as well as their suffering during the study complying with the 3Rs– Replacement, Reduction, and Refinement. We have established humane endpoints that include any signs of bladder rupture, 30% loss of weight within 2-3 days after injury, and signs of infection (prostration, the animal is not moving/apathetic/lethargic, cold to touch, lack of grooming and poor hygiene). The information provided is in the addendum approved by DGAV and ORBEA (AWB_2021_12_LS_SCRepair_Addendum3).

2.2 Mouse (*Mus Musculus*)

2.2.1 Transgenic line – p16-FDR

Our collaborator Juan Pedro Martinez-Barbera (University College London, Developmental Biology and Cancer, Birth Defects Research Centre, United Kingdom) kindly provided the p16-FDR transgenic line. P16-FDR experimental mice were initially bred using p16-FDR mice crossed with *wt* C57BL/6J mice to maintain the line on a consistent genetic background. After that, inbred crosses were made to generate p16-FDR-expressing offspring and *wt* littermates. For all experimental procedures, only heterozygous ($p16^{FDR/+}$) and *wt* p16-FDR ($p16^{+/+}$) mice were used, while homozygous ($p16^{FDR/FDR}$) mice were maintained as breeding pairs to ensure the continuity of the transgenic line. This approach was chosen due to an early lethality rate and a higher incidence of spontaneous tumorigenesis observed in the homozygous animals, as mentioned in section **1.3.7**. For the purpose of this dissertation, male mice were used predominantly over the course of the experiments, unless stated otherwise.

2.2.2 Husbandry

Animals were housed in the Rodent Facility of Instituto de Medicina Molecular João Lobo Antunes, under the standard conditions of 12-hour-light-dark cycles with access to food and water ad libitum, monitored temperature between 20 to 24 °C and relative humidity of 55±10%.

2.2.3 Genotyping

Genomic DNA (gDNA) was extracted from ear tissue samples collected through ear punching at the time of weaning. Each ear sample was transferred to a 1.5 mL Eppendorf tube and either processed immediately or stored at -20°C for later use. To extract gDNA, a 25 mM NaOH / 0.2 mM EDTA solution was added to each tube. The tubes were then incubated at 98°C for 1 hour. After the incubation, the samples were vortexed until the tissue material became colorless, indicating complete lysis. To neutralize the solution, 100 mM Tris-HCl pH 8.0 was added to each tube. The samples were centrifuged at full speed for 10 minutes at room temperature (RT). Following centrifugation, the resulting gDNA was stored at 4°C. For DNA fragment amplification, a standard polymerase chain reaction (PCR) protocol was performed using NZYTaq II 2× Green Master Mix (250 U, NZYtech, Batch YO091) and primers specifically designed to hybridize to the p16-FDR target sequence (consult **Table 2.1**). The PCR was carried out with an initial denaturation step at 95°C for 3 minutes, followed by 15 cycles of a three-step temperature cycle comprising denaturation at 95°C for 30 seconds, primer annealing at 62°C for 30 seconds, and polymerase extension at 72°C for 45 seconds, at each cycle the temperature decreased 0.4°C. This was followed by an additional 15 cycles with the same denaturation and extension steps but with a reduced annealing temperature of 56°C. The PCR concluded with a final extension step at 72°C for 5 minutes. DNase/RNase-free water was used as a negative control, while gDNA from p16-FDR heterozygous progenitors or wt served as the positive control. The PCR products were analyzed by electrophoresis on a 2% agarose gel prepared in TAE buffer (1x). For visualization of the DNA, 1:20,000 RedSafe™ Nucleic Acid Staining Solution (iNtRON, 21141) was incorporated into the gel. A 1 kb Plus DNA ladder was used as a molecular weight marker to determine the sizes of the amplified fragments.

Table2.1- Primer sequencing and details for p16-FDR genotyping.

Mouse Line	P16 WT Forward primer (5′ -3′)	P16 WT Reverse primer (5′ -3′)	FLP RT Reverse primer (5′ -3′)	Annealing temperature (°C)	Expected product length (BP)
p16-FDR	CCAAGCACAA GCGGCTATC	TAAAGCCACA TGCTAGACACGC	CGTTGTAAGG GATGATGGTG	62	**WT:** 342 **MUT:** 621

2.2.4 Spinal Cord contusion injury and post-operative care

Before being subjected to SCI, mice underwent a one-week period of handling and acclimatization. During this time, the animals became familiar with the experimenters, and their body weight was monitored to ensure they were within the optimal range for surgery (18-25g). At 8-10 weeks of age, mice were anesthetized via intraperitoneal (IP) injection of a ketamine (120 mg/kg) and xylazine (16 mg/kg) cocktail. For the spinal contusion injuries, a laminectomy was performed at the ninth thoracic vertebra (T9), identified through anatomical landmarks. This was followed by a moderate-to-severe contusion (force:

74-79 Kdyne; displacement: 550-750 μm) using the Infinite Horizon Impactor (Precision Systems and Instrumentation, LLC.). The laminectomy involved making a midline incision from just above the inferior angle of the scapulae in a rostral-caudal direction, cutting through the fat and muscle layers to reveal the spinous processes. The dorsal surface of the lamina was then exposed. Using spring scissors (Fine Science Tools, 15024-10) and Extra Fine Graefe Forceps (Fine Science Tools, 11153-10), the muscles overlying the T8-T10 laminae were cleared, exposing the foramen where the modified clamps of the Impactor stabilization platform were positioned. While the T8 vertebral body was held in place, the T9 lamina was carefully removed with spring scissors, exposing the spinal cord. The dura was then gently removed with fine-tipped forceps (Fine Science Tools, 11255-20), and the animal was positioned on the stabilization platform for the contusion injury. Following SCI, the muscle and skin layers were closed using 4.0 polyglycolic absorbable sutures (Safil, G1048213). In sham control mice, the wound was closed and sutured after the T9 laminectomy without manipulation of the spinal cord or removal of the dura. After surgery, animals received a subcutaneous (sq) injection of 0.5 ml of 0.9% NaCl and were placed in warmed cages (35ºC), remaining there for the following three days. To prevent dehydration, mice were supplemented daily with 0.5 ml of 0.9% NaCl for the first five days post-injury (dpi). Bladders were manually voided twice daily over the course of the experiment, and body weight was monitored weekly. All surgical instruments were sterilized using the Germinator 500 (World Precision Instruments) and disinfected with Virkon S (Bony Farma - Pigeon Products) and 70% ethanol before the surgery and between procedures. The mean force applied and tissue displacement for each experimental group are shown in Annex (refer to **figure 6.1**).

2.2.5 Drug Treatment

Pharmacological ablation of senescent cells using the senolytic ABT-263/*Navitoclax*

To selectively eliminate SeCs, the senolytic drug ABT-263 (Navitoclax), a targeted inhibitor of the anti-apoptotic proteins BCL-2 and BCL-xL, was employed. ABT-263 (Selleckchem, S1001, 50 mg/kg/day) , diluted in corn oil (Sigma, C8267) or vehicle (Corn oil + 5% DMSO), was administered via oral gavage for 10 consecutive days, starting at 5 days post-injury (dpi) and continuing until 14 dpi, following established protocols [13]. After SCI, mice were randomly assigned to treatment groups for the 15-dpi experimental endpoint (n = 3 per group). To control for environmental influences, different treatments were administered to animals within the same cage. The experimenters remained blinded to the treatment groups throughout the study by using coded identifiers.

Genetic ablation of p16+ cells using Diphtheria toxin

To target p16-positive cells in the p16-FDR mouse line, a protocol for the delivery of diphtheria toxin (DT) was optimized, following the methodology outlined in earlier studies [39]. DT (Sigma, D0564-1MG) was diluted in TE buffer (pH 7.5) to create a stock concentration of 2 mg/mL, then further diluted in PBS to achieve a working concentration of 1 ng/μL. Mice were administered 0.5 ng/g BW of DT or PBS via sq injection twice a week for 10 days, resulting in a total of four administrations. After

SCI, animals were randomly assigned to three treatment groups: DT-treated $p16^{(FDR/+)}$ mice, PBS-treated $p16^{(FDR/+)}$ mice, and DT-treated *wt* p16-FDR ($p16^{+/+}$) mice. To reduce environmental variables, different treatments were given to mice housed in the same cage. Throughout the study, experimenters were blinded to the treatment groups using coded labels to ensure unbiased results.

2.2.6 Behavior analysis – Basso Mouse Scale

To minimize anxiety and distress, mice were acclimated to the open-field arena for one week before the commencement of the study. The evaluation of locomotor behavior was conducted using the Basso Mouse Scale (BMS) to score and assess hind limb function and locomotion[48]. For ABT-263-treated mice, assessments were performed at baseline (day 0) and then at 1, 3, 5, 7, 10, 12, and 15 dpi. In the case of DT-treated mice, evaluations occurred at 1, 3, 7, 14, 21, and 30 dpi, to minimize over habituation and exhaustion. On the day of each behavioral assessment, two investigators, blinded to the treatment groups, independently evaluated the mice using the BMS scoring system[48] (Bas. The BMS test involves a four-minute observation period during which the investigators identify visually apparent attributes of locomotor recovery, including plantar stepping, weight support, limb coordination, paw positioning, and trunk stability. These observations are then translated into a ranked scale based on the frequency and quality of these attributes.
Detailed definitions for scoring, subscoring parameters, and the specific criteria used for evaluation are provided in **Tables 2.2, 2.3, and 2.4**, respectively.

Table 2.2-Basso Mouse Scale scoring definitions adapted from Basso *et al.*, (2006) [48]

Score	Definition
0	No ankle movement
1	Slight ankle movement.
2	Extensive ankle movement.
3	Plantar placing of the paw with or without weight support. **OR** Occasional, frequent, or consistent dorsal stepping but no plantar stepping.
4	Occasional plantar stepping.
5	Frequent or consistent plantar stepping, no coordination. **OR** Frequent or consistent plantar stepping, some coordination, paws rotated at initial contact and lift off (R/R).
6	Frequent or consistent plantar stepping, some coordination, paws parallel at initial contact (P/R, P/P). **OR** Frequent or consistent plantar stepping, mostly coordinated, paws rotated at initial contact and lift off (R/R).
7	Frequent or consistent plantar stepping, mostly coordinated, paws parallel at initial contact, and rotated at lift off (P/R). **OR** Frequent or consistent plantar stepping, mostly coordinated, paws parallel at initial contact, and lift off (P/P), and severe trunk instability.
8	Frequent or consistent plantar stepping, mostly coordinated, paws parallel at initial contact, and lift off (P/P), and mild trunk instability. **OR** Frequent or consistent plantar stepping, mostly coordinated, paws parallel at initial contact, and lift off (P/P), and normal trunk stability and tail down or up & down.
9	Frequent or consistent plantar stepping, mostly coordinated, paws parallel at initial contact, and lift off (P/P), and normal trunk stability and tail always up.

Table 2.3-Basso Mouse Scale subscoring parameters adapted from Basso *et al.*, (2006) [48]

Feature	Scoring
Plantar stepping	Frequent = 0; Consistent =1 (scored for each paw)
Coordination	None = 0; Some = 1; Most = 2
Paw Position	Rotated thru out = 0; Parallel and rotated = 1; Parallel thru out = 2 (scored for each paw)
Trunk stability	Severe = 0; Mild = 1; Normal = 2
Tail position	Down = 0; Up & Down = 0; Up = 1

Table 2.4-Basso Mouse Scale scoring criteria adapted from Basso *et al.*, (2006) [48]

Criteria	Definition
Slight	Moves less than half of the ankle joint excursion.
Extensive	Moves more than half of the ankle joint excursion.
Plantar placing	Paw is actively placed with both the thumb and the last toe of the paw touching the ground.
Weight support	(Dorsal or plantar): The hindquarters must be elevated enough that the hind end near the base of the tail is raised off the surface and the knees do not touch the ground during the step cycle.
Stepping	(Dorsal or plantar): Weight support at lift-off, forward limb advancement, and reestablishment of weight support at initial contact.
Occasional	Stepping less than or equal to half of the time moving forward.
Frequent	Stepping more than half the time moving forward.
Consistent	Plantar stepping all of the time moving forward with less than 5 missed steps (due to medial placement at initial contact, butt down, knee down, skiing, scoliosis, spasms, or dragging) or dorsal steps.
Coordination	For every forelimb step a hindlimb step is taken and the hindlimbs alternate during an assessable pass. For a pass to be assessable, a mouse must move at a consistent speed and a distance of at least 3 body lengths. Short or halting bouts are not assessable for coordination. At least 3 assessable passes must occur in order to evaluate coordination. If less than 3 passes occur, then the mouse is scored as having no coordination.
Some coordination	Of all assessable passes (a minimum of 3), most of them are not coordinated.
Most coordination	Of all assessable passes (a minimum of 3), most of them are coordinated.
Paw position	Digits of the paw are parallel to the body (P), turned out away from the body (external rotation: E) or turned inward toward midline (internal rotation; I).
Severe trunk instability	Severe trunk instability occurs in two ways: (1) The hindquarters show severe postural deficits such as extreme lean, pronounced waddle and/or near collapse of the hindquarters predominantly during the test. **OR** (2) Five or more of any of the following events stop stepping of one or both hindlimbs: • Haunch hit: the side of hindquarters rapidly contacts the ground. • Spasms: sustained muscle contraction of the hindlimb which appears to immobilize the limb in a flexed or extended position. • Scoliosis: lateral deviation of the spinal column to appear "C" shaped instead of straight
Mild trunk instability	Less than 5 events listed above and some sway in the hindquarters. Mild trunk instability is scored when the pelvis and haunches predominantly dip, rock, or tilt from side-to-side (tilt). If the tail is up, the swaying of the pelvis and/or haunches produces side-to-side movements of the distal third of the tail which also indicates mild trunk instability (side tail)
Normal trunk stability	No lean or sway of the trunk, and the distal third of the tail is steady and unwavering during locomotion. No severe postural deficits or events and less than 5 instances of mild instability

2.2.7 Bladder Function

Bladder function was evaluated twice daily by assigning a gross score based on the volume of urine retained. Bladders were manually voided twice per day, with the timing of each collection kept consistent throughout the experiment to minimize any potential influence from environmental factors. The scoring system used to assess bladder function is detailed in **Table 2.5.**

Table 2.5-Criteria to assess bladder function

Score	Designation	Amount of urine collected
0	empty	0
1	small	< 4
2	medium	4-8
3	Large	>8

2.2.8 Spinal cord extraction for cryosectioning

Mice were anesthetized with an overdose of anaesthesia and transcardially perfused first with 0.9% NaCl, followed by 4% paraformaldehyde (PFA). After confirming the laminectomy level post-mortem, a 1 cm segment of the spinal cord, centered at the injury epicenter or the equivalent region in uninjured controls, was carefully measured and dissected. The spinal cord tissue was then post-fixed in 4% PFA for 2 hours at 4°C, washed overnight in 0.2M phosphate buffer (PB), and cryoprotected in a 30% sucrose solution at 4°C for at least 72 hours, or until the tissue reached equilibrium and sunk to the bottom of the tube. Following this, the samples were prepared for embedding described in section **2.2.9**.

2.2.9 Gelatin embedding

The spinal cord samples were transferred from a 30% sucrose solution to a 7.5% gelatin (Sigma, G6144)/ 15% sucrose/0.12 M PB solution and incubated at 37°C for 1 hour and 30 minutes. Cryomolds were prefilled with a thin layer of gelatin and allowed to solidify at 4°C for 30 minutes. The samples were then placed onto the gelatin layer and carefully oriented for longitudinal or transversal cryosectioning. The cryomolds were then filled with 7.5% gelatin and incubated at 4°C for 30 minutes. To freeze the sample blocks, a plastic beaker containing isopentane was cooled in liquid nitrogen until it reached a temperature of -70/-80°C. The gelatin-embedded blocks were then submerged in the chilled isopentane and removed once frozen. Finally, the blocks were stored at -80°C until they were ready for cryosectioning.

2.2.10Cryosectioning

Tissue sections were prepared using a Cryostat LEICA CM 3050S for immunofluorescence. The cryochamber was maintained at an optimal temperature of -24°C during sectioning. After cutting, the sections were allowed to dry for 15 minutes at RT before being stored at -20°C or proceeded to the immunofluorescence protocol. For transverse sections, tissues were sectioned at 10 μm thick, with 10 slides

obtained per series. Samples were evenly distributed across sections taken along both the coronal (rostral-caudal).

2.3 Immunohistochemistry

To perform immunostaining in sections, the frozen gelatin-coated slides were thawed for 30 minutes. The gelatin was removed from the cryosections using PBS heated to 37°C (4 washes, 5 minutes). Subsequently, the slides were washed in 1x PBS/0.2% Triton X-100 (Sigma, T8787) for approximately 5 minutes. The slides were then incubated with a blocking solution consisting of 2% BSA and 0.2% Triton X-100 in 1x PBS for 2 hours at RT. Following blocking, the slides were incubated overnight at 4°C in a dark, humidified chamber with the appropriate combination of primary antibodies diluted in blocking solution. The next day, the slides were washed three times with PBS/Triton X-100 solution for 10 minutes each. After washing, the slides were incubated with the appropriate secondary antibodies and 1 mg/mL DAPI (Sigma, D9564) for 2 hours at RT in the dark. This was followed by three washes in PBS/Triton X-100 for 30 minutes each and two additional washes in 1x PBS for 15 minutes each. Finally, the slides were mounted using Mowiol mounting medium (CALBIOCHEM #475904, glycerol, Tris buffer, and MilliQ water) and stored in the dark at 4°C until imaging. All steps were performed at RT unless described otherwise. Details on blocking solutions and primary antibodies are reported in **Table 2.5** and secondary antibodies in **Table 2.6**.

Table 2.6-List of antigen retrieval protocol, blocking solutions and primary antibodies.

Antigen	Host	Dilution	Retrieval	Blocking solution	Reference
NeuN	Rabbit	1:100	_	2% bovine albumin serum/0.2% Tx in PBS	ProteIntech/26975-1-AP
Iba-1	Goat	1:100	_	2% bovine albumin serum/0.2% Tx in PBS	Novus Biologicals/NB100-1028
CD31	Goat	1:100	_	2% bovine albumin serum/0.2% Tx in PBS	R&D Systems/AF3628
CD13	Rat	1:100	_	2% bovine albumin serum/0.2% Tx in PBS	BioRad/ MCA2183T
GFAP	Rat	1:400	_	2% bovine albumin serum/0.2% Tx in PBS	ThermoFisher Scientific/13-0300
Olig2	Goat	1:100	_	2% bovine albumin serum/0.2% Tx in PBS	R&D Systems/AF2418
Atf3	Rabbit	1:200	_	2% bovine albumin serum/0.2% Tx in PBS	Cell Signalling/ 18665S
mCherry	Rat	1:200	_	2% bovine albumin serum/0.2% Tx in PBS	ThermoFisher Scientific/ M11217
DsRed	Rabbit	1:200	_	2% bovine albumin serum/0.2% Tx in PBS	Takara/ 632496

Table 2.7-List of secondary antibodies.

Antibody	Host	Dilution	Reference
Alexa Fluor anti-rabbit 647	Donkey	1:1000	Invitrogen/A-31573
Alexa Fluor anti-goat 488	Donkey	1:1000 or 1:500	Invitrogen/A-11055
Alexa Fluor anti-rat 647	Donkey	1:1000 or 1:500	Invitrogen/A-48272
Alexa Fluor anti-rabbit 488	Donkey	1:1000	Invitrogen/A21206
Alexa Fluor anti-rat 594	Donkey	1:1000	Invitrogen/ A-21209
Alexa Fluor anti-rabbit 594	Donkey	1:1000	Invitrogen/ A-21207

2.4 Image acquisition

Transversal sections

For high-resolution imaging of transversal sections, SC close-up images were captured using a Zeiss LSM 880 laser scanning confocal microscope equipped with a Plan-Apochromat 20x / 0.80 Ph dry objective. Fluorescence detection was performed as follows: DAPI fluorescence was detected using 405 nm for excitation, and a 415–480 nm detection window. Alexa Fluor 488 fluorescence was detected using a 488 nm laser line of an argon laser for excitation, with detection in a 497–541 nm window. Alexa Fluor 594 was detected using 561 nm for excitation, with detection between 571–610 nm. Alexa Fluor 647 was excited at 633 nm, with a detection window of 643–750 nm. The pinhole size was adjusted to 1 Airy Unit (AU) to maintain consistent optical slice thickness across all four channels. Z-stacks were acquired with the zoom set to 1, covering a 212.55 × 212.55 μm area at a 1024 × 1024 frame size, resulting in a pixel size of 0.21 μm. Each image presented is a maximum intensity projection of a z-stack obtained from 10 μm cryosections, processed using Zeiss ZEN 2.3 Black Edition software. Maximum intensity projections were conducted using Fiji software (Schindelin et al., 2012). Six sections were acquired per biological replicate, 3 on the rostral side and 3 on the caudal side.

2.5 Image Data analysis

2.5.1 Quantification of Double-positive mCherry-positive cells after immunohistochemistry for each of the cell markers NeuN, Iba-1, CD31, CD13, GFAP and Olig2

Immunohistochemistry data was analyzed in Qupath (v.0.5.1). To characterize the p16-mCherry-positive cells, transversal sections selected from the lesion periphery, spaced 200 μm apart (ranging from 0.5 to 2 mm rostrally or caudally to the lesion), were analyzed. A total of 3 sections rostral and 3 sections caudal to the lesion were processed. For each section, pixel classification was performed to identify p16-mCherry-positive areas. Nuclei were detected using QuPath's nuclei detection tool applied to the DAPI channel, allowing for the enumeration of mCherry-positive nuclei. Object classifiers for each marker (CD31, CD13, NeuN, Iba-1, GFAP and Olig2) were applied on top of mCherry-positive nuclei allowing the classification of these cells. This established workflow was applied to both rostral and caudal regions as well as for the entire dataset within each timepoint and group of markers. Quantifications were performed at 7, 15, and 30 dpi.

2.6 Flow cytometry – single cell dissociation protocol for flow cytometry

2.6.1 Spinal cord isolation

For flow cytometry, it is essential to use fresh tissue to ensure accurate results. In these studies, P16-FDR mice were predominantly used, along with C57BL6J mice. Mice were anesthetized with isoflurane until an anesthetic overdose occurred. Following anesthesia, the spinal cord was exposed, and the injury site was located at the T9/T10 vertebrae. A 2 mm segment of the spinal cord was transected both rostrally and caudally around the lesion site. In the case of sham injuries, the laminectomy site at T9/T10 served as the anatomical landmark for tissue dissection. For uninjured mice, the T9 vertebra was used as the reference point. After dissection, the tissue was immediately placed in a petri dish containing 1 mL of ice-cold, freshly carbox (95% O_2, 5% CO_2) bubbled 1x aCSF (Ecocyteshop, LRE-S-LSG-1000-2), prepared according to the manufacturer's instructions. The surgical instruments were sterilized in advance using the Germinator 500 (World Precision Instruments). Between each mouse, the instruments were disinfected with Virkon S (Bony Farma - Pigeon Products) and cleaned with RNaseZAP (Sigma-Aldrich, R2020) to prevent cross-contamination between samples.

2.6.2 Single-cell spinal cord tissue dissociation

After isolating the spinal cord, the tissue was minced and mechanically dispersed using a sterile blade to increase the total surface area. The tissue was then subjected to enzymatic dissociation using a buffer

containing the following components: 20U/ml of 200 U/ml papain (15 U/mg; STEMCELL Technologies, 07466), 1x aCSF (Ecocyteshop, LRE-S-LSG-1000-2), 453 CDU/mL collagenase from *Clostridium histolyticum* (125 CDU/mg; Sigma-Aldrich, C2674), 1561 μM of 1M CaCl2, 1.25 U/mL DNase I recombinant, RNase-free (Roche, 04716728001), and 1mM L-cysteine (Sigma-Aldrich, W326305). This enzyme solution was specifically designed to break down the extracellular matrix (ECM) and disrupt cell-cell junctions, thereby preventing cell aggregation through the degradation of free DNA and prevent cell death via inclusion of antioxidant components. The enzymatic dissociation step was performed at 37°C for 10 + 10 minutes. During this time, mechanical dissociation was concurrently carried out to further facilitate cell separation. This was achieved using a P1000 micropipette and a fire-polished Pasteur glass pipette with a diameter of approximately 0.5-0.8 mm and rounded edges. Care was taken to perform this step gently to avoid the formation of air bubbles. Following enzymatic and mechanical dissociation, an equal volume of ice-cold aCSF was added to the cell suspension (1:1 ratio). To remove any undigested tissue, the suspension was filtered through a 70 µm cell strainer (Falcon, 352350) into tubes coated with 30% BSA. Following this step, a gradient centrifugation was conducted to further purify the cell suspension from myelin, small ECM components, and dead cells that might have escaped the cell strainer. This was accomplished using a discontinuous gradient of 5% and 15% Optiprep™ solution (STEMCELL Technologies, 07820). Briefly, the lightest 5% layer is pipetted into the bottom of a 50mL falcon that contains the cell suspension, followed by pipetting of the dense 15% layer. The centrifugation was performed at 200 g for 5 minutes at RT, with slow acceleration and deceleration to maintain the integrity of the gradient and achieve effective separation. Cells were collected from the interface between the Optiprep™ solutions and transferred to a new Falcon tube. Next, cells were washed by adding ice cold aCSF until a final volume of 20 mL is reached and centrifuging at 290 g for 7 minutes at 4°C. After discarding the supernatant, the cells were kept on ice, aCSF was added to achieve the recommended staining volume of 100µL with a maximum of $1e10^6$ cells per staining. In the early stages of protocol optimization, a Trypan Blue exclusion test was performed (1:10) to assess cell viability (ThermoFisher, 15250061). In flow experiments for each biological replicate, two technical replicates were accounted

2.6.3 Staining – labeling for specific cell types

Cells were incubated with a panel of flow cytometry antibodies for different cell types, Zombie Violet fluorescent dye and Fc block for 20 minutes at 4°C. Zombie Violet is an amine-reactive fluorescent dye that is impermeable to live cells but permeable to cells with compromised membranes; thus, zombie-positive cells are apoptotic/necrotic cells. Fc Block was also used to reduce nonspecific Fc receptor antibody binding. After incubation, cells were washed with aCSF by centrifugation at 290 g for 5 minutes at 4°C. The cells were then incubated with DRAQ5 (1:2500) for 10 minutes at RT. DRAQ5 is a compound that labels nucleated cells. After incubation, additional aCSF was added, and the samples were kept at 4°C until analysis. The data was acquired using the LSRFortessa™ X-20 flow cytometer. The antibodies, dyes, and their staining conditions, as well as the compounds used to establish a live/dead cell exclusion analysis are detailed in **Table 2.7** and **Table 2.8**, respectively.

Table 2.8-List of antigen antibodies used in flow cytometry and respective host, clone, fluorophore, dilution reference, and cell marker. * Represent the original antibodies used that were replaced during protocol optimization.

Antigen	Host	Clone	Fluorophore	Dilution	Reference	Cell marker
ACSA-2 [1]	Rat	IH3-18A3	PE	1:100	Miltenyi Biotec/130-123-284	Astrocytes
CD13 [2]	Rat	R3-242 (RUO)	BV650	1:100	BD OptiBuild/ 740488	Pericytes
CD45 [3]	Rat	30-F11	FITC	1:100	BioLegend/103108	Common leukocyte marker
CD31* (PECAM-1) [4]	Rat	390	APC	1:200	Invitrogen /17-0311-82	Endothelial cells
CD31 (PECAM-1) [4]	Rat	390	PerCP-eFluor 710	1:200	eBioscience/46-0311-80	Endothelial cells
CD11b [5]	Rat	M1/70	BV750	1:100	BioLegend/ 101267	Macrophages and microglia
O4 [6]	Mouse	O4	APC	1:400	Miltenyi Biotec/ 130-119-155	Oligodendrocytes
Thy1.2/CD90.2* [7]	Rat	30-H12	Alexa Fluor 700	1:100	BioLegend/105320	Neuron/T cell marker
Thy1.2 [7]	Rat	30-H12	BV605	1:100	BioLegend/105343	Neurons/T cell marker
Tmem119 [8]	Rat	V3RT1GOsz	PE-Cyanine7	1:100	Invitrogen /25-6119-82	Microglia-biased
Fc Block/CD16/32 [9]	Rat	93	-	1:100	BioLegend/101301	-

[1]: astrocyte cell surface antigen-2; [2]: cluster of differentiation 13;[3]: cluster of differentiation 45; [4]: cluster of differentiation 31; [5]: Cluster of differentiation molecule 11b; [6]: Oligodendrocyte Marker O4; [7]: Cluster of Differentiation 90; [8]: Transmembrane protein 119;

Tabela 2.9-List of compounds that were used to perform a live/dead cell exclusion analysis and respective detector, dilution, reference, and target.

Compound	Detector	Dilution	Reference	Target
Zombie Violet	Violet laser (405)	1:250	BioLegend /423113	Cells with compromised membranes
DRAQ5	Alexa Fluor® 647, APC and Alexa Fluor® 700	1:2500	BioLegend /424101	Nuclei in live cells

2.6.4 Gating strategy and data analysis

Data analysis was performed using FlowJo software (v10.10). The gating strategy remained conserved throughout all of the analysis. From the total events acquired from the flow cytometer, a Forward Scatter (FSC) vs Side Scatter (SSC) gate was applied to exclude debris and select the main cell population. Next, a Forward Scatter-Height (FSC-H) vs Forward Scatter-Width (FSC-W) is then used to identify and gate on single cells, excluding doublets and cell aggregates. A viability dye gate is applied to select only live cells by using FSC-H vs Zombie-Violet-AF405. The following gates were established inside the live cell population.

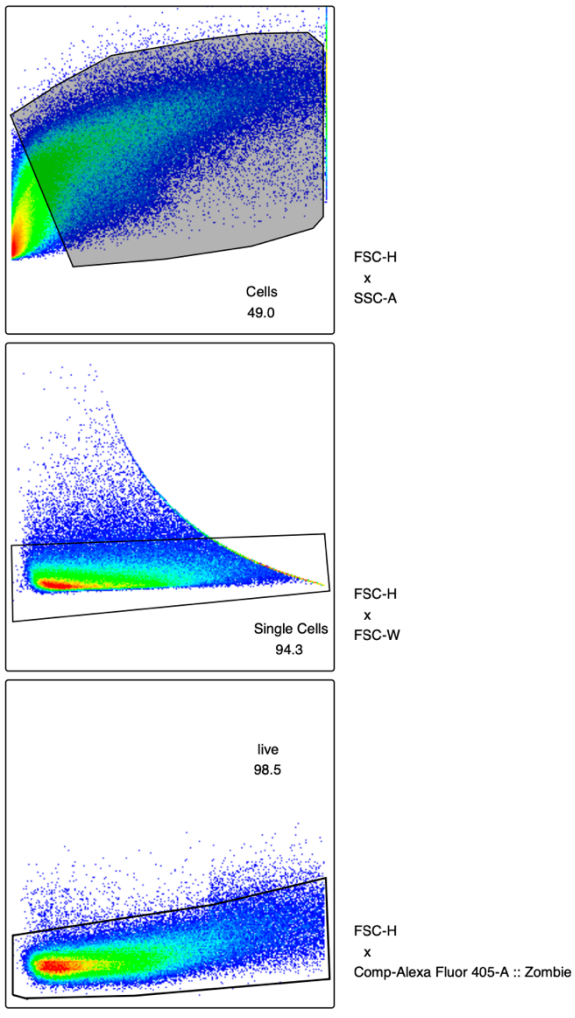

Figure 2.1-Representative image of the gating strategy that allows the selection of live cells. Forward Scatter-Height (FSC-H); Side Scatter-A (SSC -Area); Forward Scatter-Width (FSC-W); Zombie-Violet-AF405

2.7 Single-cell preparation for fluorescence-activated cell sorting (FACS) and RNA extraction of sorted p16-mCherry cells

To isolate mCherry-positive and mCherry-negative population cells via FACS sorting, cells were isolated into a single-cell suspension as described previously, followed by staining with Zombie Violet to discriminate live cells from dead cells/debris. Live cell gate was performed on the Zombie Violet negative population. A gating strategy was used to differentiate and establish gates for mCherry-positive and mCherry-negative populations. To be able to investigate cell type enrichment and perform differential gene expression, both p16-expressing/mCherry-positive and mCherry-negative cells (control) were sorted from the same sample. Sorting was performed using a BD FACSAria III equipped with a 100 μm nozzle. Given the rarity of mCherry-positive cells, sorting was performed for yield. Cells were sorted into collection tubes containing 1x aCSF supplemented with 2% BSA. After sorting, cells were centrifuged at 200 g for 5 minutes at 4°C. The supernatant was discarded, and 500 μL of TRIzol (Invitrogen/15596018) was added to each sample. The pellet was destroyed by vigorous pipetting and left to rest for 5 min at RT to ensure complete nucleic acid dissociation from protein complexes. Samples were stored at -80°C until RNA extraction. Total RNA was extracted using the miRNeasy Mini Kit (Qiagen/217004) using a phenol: chloroform starting protocol, following the manufacturer's instructions. RNA quality was assessed with a Fragment Analyzer and bulk sequenced at the Genomics Unit of the Instituto Gulbenkian de Ciência (IGC). For more information regarding RNA quality refer to Annex 2 (**Table A.1**). The bioinformatic analysis was conducted by the lab's bioinformatician, Daniel Ribeiro (PhD).

Gene Expression Quantification

Using the STAR v2.7.10a pipeline (DOI: 10.1093/bioinformatics/bts635), gene expression quantification is performed by aligning RNA-seq reads against the mouse GRCm39 reference transcriptome and counting those mapping to each given gene. Raw read counts for 17,072 genes were obtained. To prepare count data for differential gene expression analysis, normalization factors to scale raw library sizes were obtained using the function calcNormfactors from package edgeR (DOI: 10.1093/bioinformatics/btp616) after converting the filtered count matrix into a DGEList object. The voom method with quantile normalization (DOI: 10.1093/nar/gkv007) was then applied to count data to obtain gene expression estimates in log2-counts per million (logCPM).

Differential Gene Expression Analysis

Differential gene expression analysis was performed with linear models using the limma R package (DOI: 10.1093/nar/gkv007). Global empirical Bayes statistics were calculated for each gene, allowing for the identification of genes significantly differentially expressed those with an associated adjusted p-values < 0.05 and the magnitude of difference in expression measured in log2 fold-change between the

two conditions. Using this approach, 6040 genes were identified as significantly differentially expressed.

Derivation of Gene Expression Signatures for the Major Spinal Cord Cell Types

We employed CIBERSORTx (doi.org/10.1038/s41587-019-0114-2) to infer gene signatures of major cell types present in the mouse spinal cord. The tutorials provided at the CIBERSORTx portal (https://cibersortx.stanford.edu/) were used as a basis for our analysis. The Zeisel dataset (DOI: 10.1016/j.cell.2018.06.021) was used to extract single-cell gene expression data from spinal cord mouse tissue (l5_all.loom file from mousebrain.org). Cells in the dataset are hierarchically classified according to TaxonomyRank2. Signatures were generated with the default parameter except for the following: Min. Expression: 1; Replicates: 20; Sampling: 0.

Estimation of Cellular Composition on FACS-Sorted Samples

We used CIBERSORTx deconvolution to estimate the cellular composition of FACS-sorted samples from bulk RNA sequencing. To build the mixture file containing bulk RNA-seq expression profile, we built a count matrix derived from the RNA-seq normalized counts. We ran the CIBERSORTx deconvolution algorithm with default parameters except for the following: Batch correction mode: S-mode; Permutations: 500.

2.8 Statistical analysis

Statistical analysis was conducted using GraphPad Prism v9.0.0. Flow cytometry data was either analyzed using an unpaired t-test or one-way ANOVA followed by Bonferroni correction, depending on the data. Immunohistochemistry data was analyzed using one-way ANOVA followed by Bonferroni correction. All data are presented as mean ± SEM, with statistical significance set at p-values ≤ 0.05. Details on statistical parameters, including sample sizes and precision measures (e.g., p-values), are provided in the figure legends. For BMS, Two-way ANOVA, followed by a Bonferroni's post-hoc test was performed.on GraphPad Prism v9.0.0.

3 RESULTS

3.1 Optimization of a single-cell spinal cord tissue dissociation protocol for flow cytometry

Flow cytometry can be a great complementary technique to immunohistochemistry (IHC) as it allows for faster and less laborious identification of different cell populations. It also allows for the identification of weakly expressed surface antigens. Our end goal was to identify and isolate mCherry/p16-positive cells from the spinal cord (SC) through flow cytometry and determine the cell types that are mCherry-positive. Currently, there are no suitable optimized single-cell SC tissue dissociation protocols. Therefore, to achieve our end goal, we needed to optimize a good single-cell SC tissue dissociation protocol in the lab suitable for flow cytometry. With this protocol, we aimed to successfully dissociate spinal cord tissue while retaining the cells viability and retrieve different cell populations representative of those in the CNS, particularly in the SC.

3.1.1 Key features of the optimized protocol

The new protocol for SC single-cell isolation was designed based on the protocol performed by *Huettner et al* [49]. We introduced some key features and made optimization steps along the way. A notable aspect of our protocol was using cold freshly bubbled aCSF to maintain oxygenation and a balanced pH to increase the likelihood of cell survival. Initially, we tested a "homemade" aCSF solution prepared in the lab, however, we switched to a commercially available aCSF. To perform the dissociation of the SC tissue, we opted to perform both mechanical and enzymatic dissociation, given the intrinsic tissue-related barriers to a successful SC single-cell dissociation. The process was challenging as nervous tissue, in particular SC tissue, has a complex and dense network of neurons and glial cells (astrocytes, oligodendrocytes, and microglia). Neurons, for example, present highly ramified processes that interconnect with each other, making them very delicate and prone to breakage. This, in turn, poses a challenge in dissociating cells without compromising their viability. Moreover, given the high cell heterogeneity, optimizing a "one-size-fits-all" protocol suitable for each SC cell type remains difficult. Finally, SC cells are embedded in a very robust ECM forming strong connections between cells, making it difficult to break down ECM components without damaging cells in the process. Establishing the enzyme cocktail and the concentrations used was vital to the success of the dissociation step. We ought to find a perfect balance between promoting both disruption of cell-to-cell junctions and extracellular matrix components while retrieving an increased yield of cells. In addition, the retrieved cells must remain viable without cleavage of essential membrane proteins and cell surface receptors that could halt flow cytometry detection. In the enzyme mix, we included components such as papain. Papain has been described as a cysteine peptidase C1 protease. It has been shown that papain is less destructive and more efficient when compared to other proteases used such as trypsin [50], [51]. L-cysteine was included as an

activator of Papain and to help scavenge some of the ROS generated during aCSF bubbling [52]. However, L-cysteine was used in small amounts as this amino acid can be excitotoxic to neurons. The use of papain promotes the release of free DNA that could promote cell aggregation, for that reason DNase I was used [50]. The temperature of incubation was maintained at 37ºC [50]. A gradient of Optiprep was used to isolate the cells of interest, as the high density of Optiprep facilitates the fractioning of the cells into layers. Initially, a continuous gradient was used (15%) as this gradient would retrieve a single-cell suspension, but we soon realized that we could be losing less dense cells. To allow for better fractioning and purification, a 5% gradient was added. Some optimizations were also made in the centrifugation parameters, speed, duration, temperature, acceleration, and deacceleration steps to increase cell separation and decrease cell death, ensuring that the dissociated cells could endure several centrifugation steps important for flow cytometry protocols. We started our optimization with uninjured p16FDR/+mice. We isolated 8 mm of SC tissue (4 mm rostrally and 4 mm caudally from the T9 vertebrae level) and further refined the protocol to achieve 4 mm (2mm rostrally and 2 mm caudally). This is relevant as it allowed a narrow window view into the perilesion site for each animal. After this optimization, we proceeded to the analysis of injured p16FDR/+ mice. Cells were always maintained at 4ºC to slow down biological processes and improve cell viability.

3.1.2 Viability analysis

To access the outcome of the single-cell dissociation protocol optimizations, we performed a Trypan blue exclusion test **(Figure 3.1)**. Before optimization, there were more dead/blue cells labeled with Trypan Blue, small cell aggregates, and there seemed to be some crystal formation **(Figure 3.1.A)**. After optimization, the cell suspension seemed to have more live (fewer cells with Trypan Blue labeling) and individual cells, with different morphologies, fewer aggregates, and no crystals **(Figure 3.1.B)**. This suggests that the protocol with the modifications implemented allows for better tissue dissociation and cell viability. The observation of different morphologies suggests the possibility that the protocol is retrieving different SC cell types.

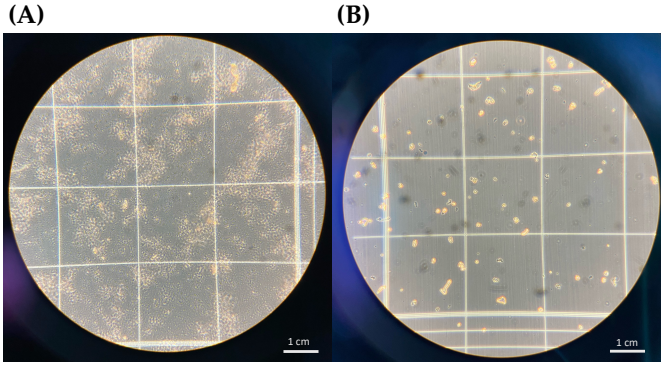

Figure 3.1-Trypan blue exclusion test in uninjured p16-FDR mice after protocol optimization shows improvement in single-cell recovery. Trypan blue test after recovering cells, with the protocol adapted from Huettner et al [49], before (A) and after (B) protocol optimization. In (A) there are more dead cells (labeled with trypan blue), more clumps and aggregates as well as crystal formation. In (B) more individual live cells (with different morphologies) were recovered. Fewer aggregates, better separation, and no crystal formation after optimization can also be

observed. Each image represents n=1 p16FDR/+uninjured mice. Images were captured at 40x 20x magnification, respectively.

We also assessed cell viability through flow cytometry by staining the cells with a combination of dyes at 3 and 7 days post-injury (dpi) **(Figure 3.2)**. Zombie Violet, an amine-reactive fluorescent dye, identifies cells with compromised membranes, while DRAQ5 stains nucleated cells. Our protocol retrieved around 91.9% and 94.5% of live cells (Zombie-/DRAQ5+), with minimal debris and dead cells observed at both timepoints, respectively **(Figure 3.2 A)**. There seemed to be more debris at 3 dpi than those observed at 7 dpi **(Figure 3.2 A)**. Additionally, it is important to note that these results remained consistent as the percentage of live cells recovered in the p16-FDR mice is the same in laminectomized (sham) and injured conditions at both timepoints with no significant differences **(Figure 3.2 B)**. Altogether, the protocol we developed is able to retrieve live cells independently of the animal condition (injured vs sham) and timepoint, with low percentages of debris and dead cells. Additionally, a successful double gaiting strategy of Zombie-Violet and DRAQ5 staining showed that the dissociated cells seem to be suitable for flow cytometry.

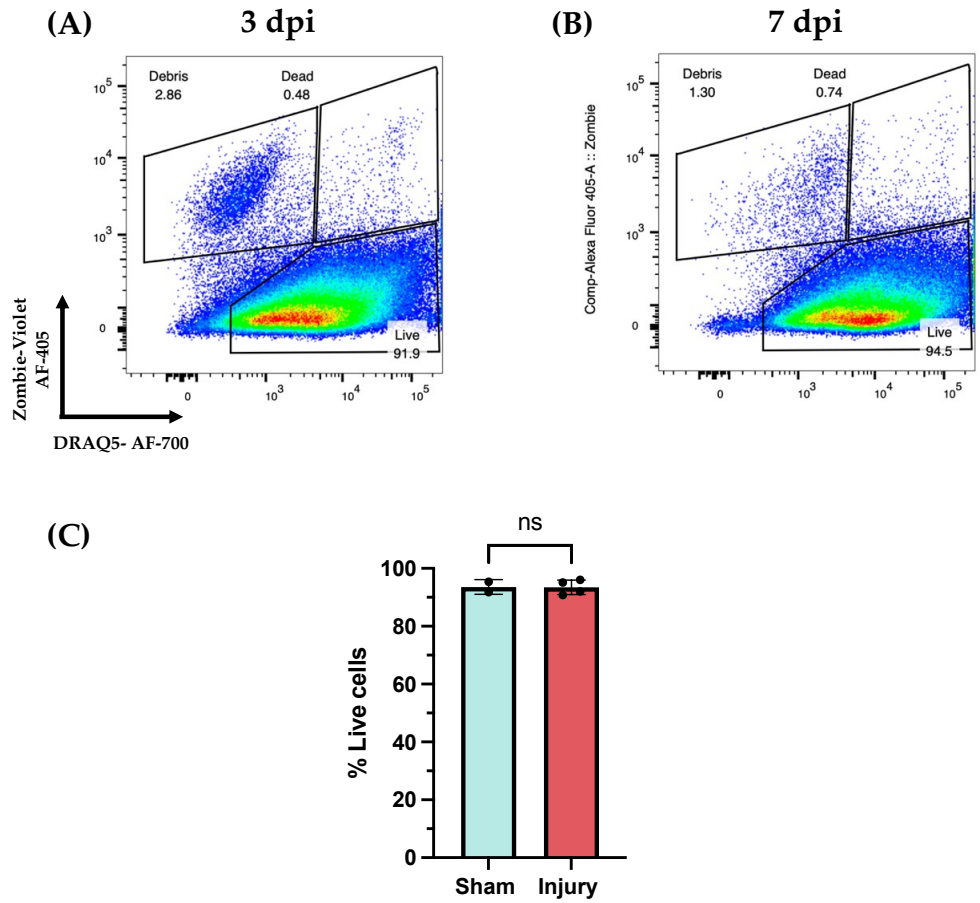

Figure 3.2- Single-cell dissociation protocol recovers a high percentage of live cells in both sham, 3 and 7 dpi conditions. A single-cell dissociation protocol for flow cytometry described above was performed in spinal cord sections of laminectomized (sham) and injured p16-FDR mice, followed by Zombie Violet and DRAQ5 staining. A) and B) Percentage of live cells (Zombie-/DRAQ5+), dead cells (Zombie+/DRAQ+), and debris (Zombie+/DRAQ-) in injured p16FDR/+mice at 3 and 7dpi, respectively. This data revealed that around 90-95% of the cells retrieved at both timepoints are live cells. C) The percentage of live cells remained consistent in sham and injured p16FDR/+mice at 3 and 7 dpi. Each bar represents means ± SEM, and data from both timepoints was pooled together, n=2-4 independent samples per group. Statistical analysis was performed using an unpaired t-test (95% confidence interval). No significant statistical differences were observed, non-significant (ns).

3.1.3 Analyzing spinal cord cellular diversity after SCI through flow cytometry

After having succeeded in isolating a population of live SC cells, we wanted to see if they were representative of the cell type heterogeneity present in the SC. Having this objective in mind, we optimized and established a multi-color panel that would allow to discriminate between cell types known to be present in the SC in both physiological and injury conditions. We aimed to complete the challenging task of using all the different markers simultaneously; therefore, the panel was optimized accordingly. Not only did we try to include the highest number of cell membrane markers for better cell type discrimination, but also the fluorophores selected for each marker had to be carefully selected to avoid spectrum overlaps. Ultimately, we were able to achieve a final panel of 7 markers **(Table 3.1).**
Unfortunately, due to the high spectral overlap between fluorophores and the fact that DRAQ5 has multiple emission peaks, thus being detected in several channels (Alexa Fluor 647, APC, and Alexa Fluor 700), we decided to perform live cell gates with Zombie Violet exclusively. Nevertheless, the gating strategy remained conservative to the live population already discriminated above **(Figure 2.1)**.

Table 3.1-The final color panel achieved post-optimization containing the cell surface marker, the respective fluorophore, and the cell type labeled.

Detected cell surface marker	Fluorophore	Labelled cell type
ACSA-2	PE	Astrocytes
CD13	BV650	Pericytes
CD45	FITC	Common leukocyte marker
CD31 (PECAM-1)	PerCP-eFluor 710	Endothelial cells
CD11b	BV750	Macrophages and microglia
Thy1.2	BV605	Neurons/T cell marker
Tmem119	PE-Cyanine7	Microglia-biased
mCherry	mCherry	p16 positive cells
Fc Block/CD16/32	-	-
Zombie Violet	Violet laser (405)	Apoptotic/necrotic cells

After the dissociation protocol, cells from sham and injured $p16^{FDR/+}$ 7 dpi mice were stained with the antibodies against the cell surface markers listed in **Table 3.1** and analyzed by flow cytometry. Based on our results, regardless of the condition (sham and injury), we were able to successfully isolate various types of cells from the SC, such as immune cells (CD45+), astrocytes (ACSA-2+), macrophages/microglia (CD11b+), neurons (Thy1.2+), pericytes (CD13+), and endothelial cells (CD31+) **(Figure 3.3)**. It is important to note that both parenchymal cells (neurons and astrocytes) and vascular-associated cells (pericytes and endothelial cells) were retrieved. Additionally, approximately 75% of the total cell population were Thy1.2+ cells, which is a good indicator for the preservation of neuronal populations with our protocol (**Figure 3.3.A**). This neuronal enrichment is very difficult to achieve, as most neurons do not survive flow cytometry conditions. Thus, this outcome was expected and is consistent with our

protocol's aim to enrich for neurons. The distribution of the remaining cell types seemed relatively even **(Figure 3.3.A)**. When comparing the sham and injury conditions, there was a tendency to have more cells present of a specific type in the injured condition compared to the sham condition **(Figure 3.3.C)**. This could indicate an increased representation of specific cell populations upon injury. In fact, in the dot plots presented on panel **3.3 B**, we can observe the prevalence of injury-specific populations in injured mice compared to sham controls **(Figure 3.3.B)**. For example, in the injured condition, there was a noticeable difference in the presence of immune cells (CD45+), macrophages/microglia (CD11b+) **(Figure 3.3.B)**, **C)**. These cell types were increased in the injury condition, and subpopulations of macrophages/microglia with high and low CD11b expression were observed. The CD11b high population is not observed in the Tmem119+ population; this possibly indicates the presence of an injury-specific macrophage population (CD11b+/Tmem119-) **(Figure 3.3.B).** This outcome was expected because, in a SCI context, various cells are recruited to the injury site, including tissue-resident microglia and astrocytes, as well as blood-derived macrophages [6]. We did not observe a similar trend in the neuronal population, which is not surprising given that, in injury conditions, there is neuronal death [6]. We also lack data on oligodendrocytes due to our inability to optimize the O4 antibody.

Furthermore, we acknowledge that Thy1+ cells can also be immune cells (CD45+), 75% of Thy1+ cells may include a portion of cells that are also CD45+ **(Figure 3.2 A)**). However, when compared to the 2.67% of CD45+ cells, we can safely assume that the majority of Thy1+ cells seem to be neurons. Nevertheless, it is important to interpret all these results cautiously given the low sample size (*n*) that prevents us from drawing significant conclusions when comparing conditions. The optimized protocol presented in this thesis successfully isolates a diverse subset of neural and non-neural populations from the SC that can be identified with canonical markers used in flow cytometry. The relatively high proportion of neurons is a good indicator of neuronal preservation which was one of the main objectives behind this protocol design and optimization. However, even though this protocol overrepresents the neuronal population, it still reflects the cellular diversity found in the SC. In addition, this protocol appears to replicate the changes in cell proportion seen in injury conditions, but further testing is required to obtain significant results.

(A)

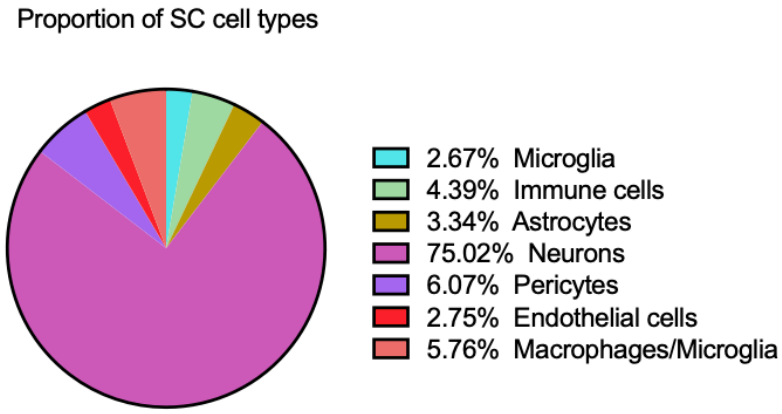

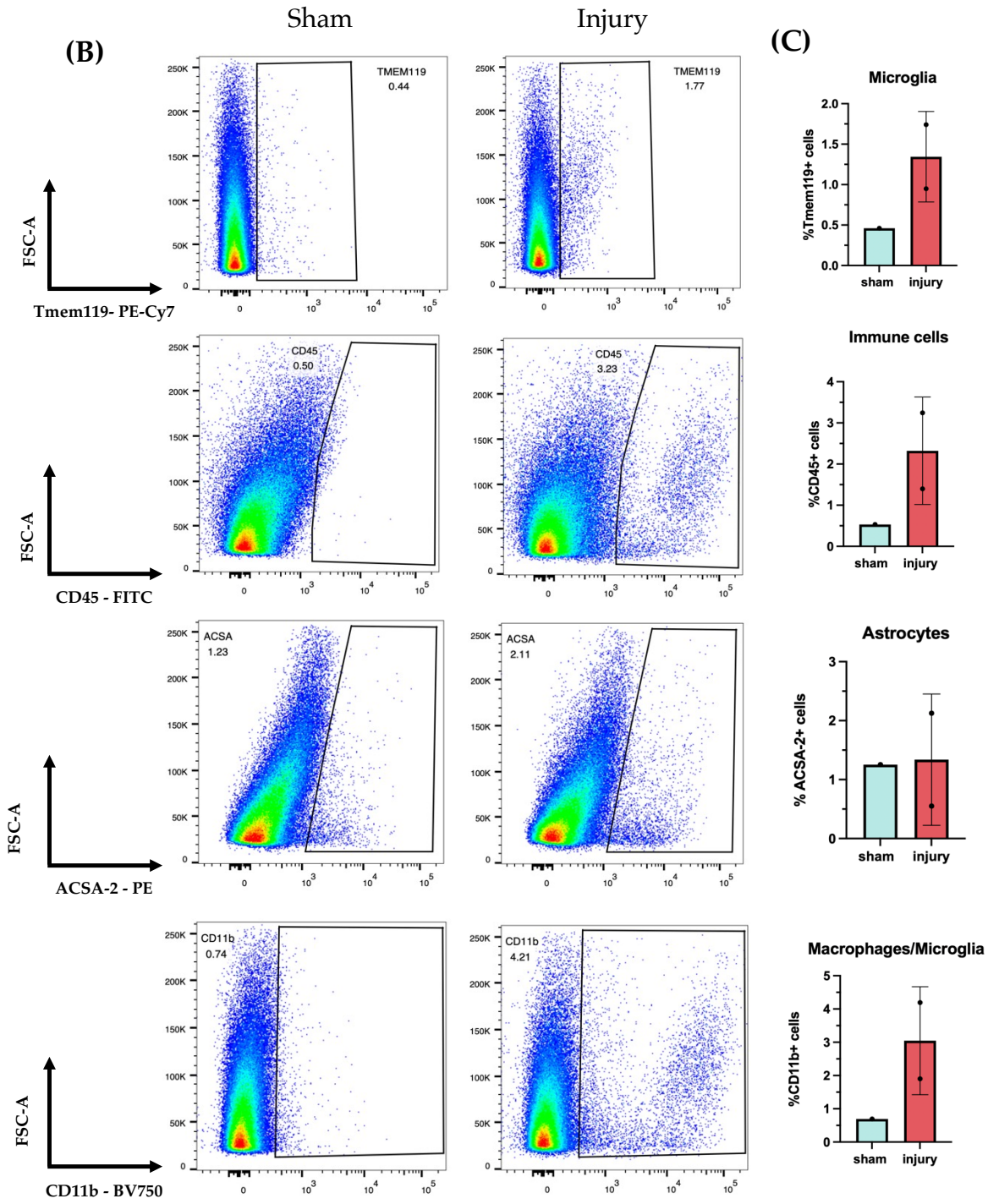
Sham
Injury
(B)
(C)
TMEM119
0.44
TMEM119
1.77
FSC-A
Tmem119- PE-Cy7
Microglia
%Tmem119+ cells
sham
injury
CD45
0.50
CD45
3.23
CD45 - FITC
Immune cells
%CD45+ cells
ACSA
1.23
ACSA
2.11
ACSA-2 - PE
Astrocytes
% ACSA-2+ cells
CD11b
0.74
CD11b
4.21
CD11b - BV750
Macrophages/Microglia
%CD11b+ cells

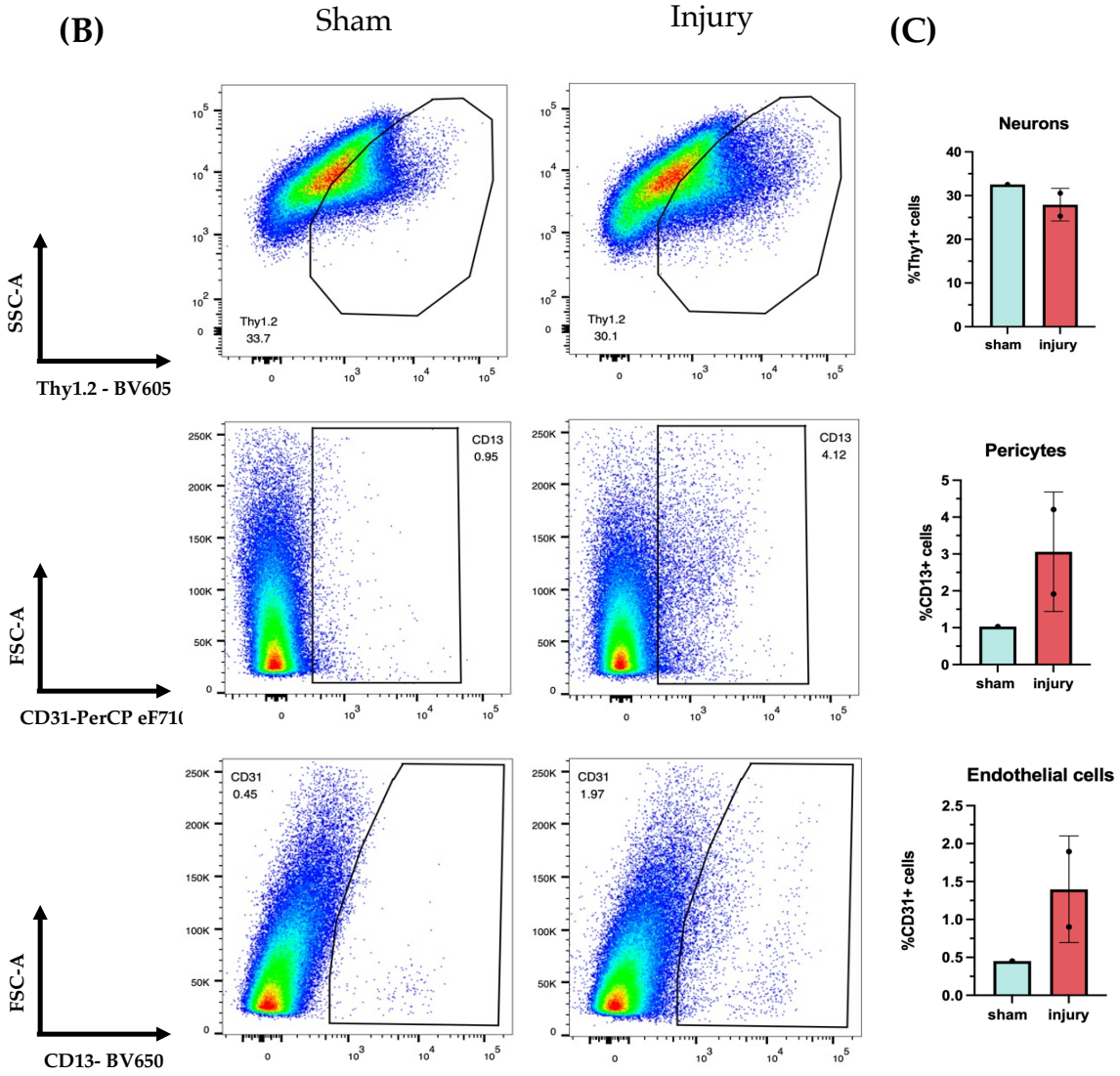

Figure 3.3- Optimized single-cell protocol reveals diverse cell populations in spinal cord tissue at 7dpi. Cells from sham and injured p16$^{FDR/+}$mice retrieved with the optimized protocol and labelled with canonical markers for different cell types known to be present in the spinal cord and/or recruited upon injury: Microglia (Tmem119+), immune cells (CD45+), astrocytes (ACSA-2+), Macrophages and Microglia (CD11b+), Neurons (Thy1.2+), Pericytes (CD13+), Endothelial cells (CD31+). **A)** Proportion of cell types retrieved independently on the condition (pool of n =3 samples sham and injured). Cells from different cell types were retrieved with the optimized protocol; the majority of isolated cells were Thy1.2+. **B)** Representative flow cytometry plots showing gating strategy for different cell populations in spinal cord tissue in sham and injury conditions. These results indicate that injury-specific populations seem to be present. In this representation, there is n=1 sham n=1 injured p16$^{FDR/+}$mice at 7 dpi. **C)** Quantification of each cell type proportion isolated between conditions, sham and injury. Each bar represents means ± SEM (n =1-2 independent samples per group). Scale bar: Not applicable for flow cytometry plots. No statistical testing was performed. FSC-A: Forward Scatter Area; SSC-A: Side Scatter Area.

3.2 A p16-positive cell population is induced upon spinal cord injury

Previous immunohistochemistry data from our lab indicated that p16/mCherry-positive cells were induced upon injury, being detected as early as 7 dpi and presented a transient profile (see Annex, **figure 6.2**). The quantifications behind these results are quite labor-intensive and are typically estimates, as the quantification is not carried out on the entire dissected tissue but rather at intervals of 200 μm between sections. Following the optimization of a robust flow cytometry protocol, we wanted to validate and possibly expand previous observations indicating the induction of mCherry-positive cells in response to injury. This flow cytometry approach would allow us to analyze the entire dissected sample instead of relying on individual sections and, thus, process and analyze more cells. Moreover, flow cytometry goes beyond the binary classification of IHC (positive and negative), with this technique, we can measure the mCherry expression intensity (high and low). Furthermore, a multiparametric analysis is also possible, allowing us to simultaneously identify distinct mCherry-positive cell populations using different markers. Fluorescence-activated cell sorting (FACS) can also be employed to isolate mCherry-positive cells for further molecular and functional analysis. SC tissue from sham and injured 7 dpi $p16^{FDR/+}$ mice comprising the perilesion site (2 mm rostral and 2 mm caudal) was processed according to our optimized protocol. The same protocol was employed to SC tissue from uninjured mice as negative controls to establish baseline mCherry expression levels and account for autofluorescence.

Previously in our lab, in an independent experiment, we also attempted to quantify mCherry-positive cells in injured $p16^{FDR/+}$ at 3 dpi through IHC, however, we were unsuccessful (refer to Annex, **Figure 6.3** for more details). For that reason, we wanted to test if we could see mCherry-positive cell induction at an earlier timepoint, therefore, SC tissue from 3 dpi mice was also processed. Our results indicated that mCherry-positive cells were significantly increased in injured $p16^{FDR/+}$ compared to sham controls at 7 dpi, indicating that this increase is injury-specific **(Figure 3.4 A) and B)).**

Therefore, the induction of mCherry-positive cells in injured 7 dpi mice through flow cytometry validated the results previously obtained by the lab through IHC. In addition, some mCherry-positive cells seemed to express more mCherry than others, indicating the presence of mCherry high and low cells. This was expected since the different levels of reporter expression had already been described [39]. **(Figure 3.4 A).** Moreover, mCherry-positive cells showed a wide range of SSC-A values, indicating heterogeneity in their internal complexity or granularity **(Figure 3.4 A).** Compared to uninjured $p16^{FDR/+}$, sham-injured mice presented significantly more mCherry-positive cells, suggesting that this difference stems from the laminectomy injury performed in sham-injured mice. Due to the lack of animals available, 3 dpi sham injury mice were not included in this data. However, when we compared 3 dpi injured mice to uninjured controls, we found no significant differences between these two groups. This indicated that mCherry protein, and thus the expression of the *cdkn2a* locus, is either not expressed or is below detection levels in injured $p16^{FDR/+}$ mice at 3 dpi. Furthermore, upon injury, the percentage of mCherry-positive cells at 7 dpi was significantly higher when compared to 3 dpi. This suggested a time-dependent increase in mCherry-positive cells upon injury, as the number of mCherry-positive cells peaked at 7 dpi but not at 3 dpi, complementing previous results from the transient profile of mCherry-

positive cells (see Annex, **Figure 6.2**). However, sham 3 dpi samples should be included in the future to discard any technical bias that would influence the prevalence of mCherry-positive cells.
Nevertheless, the mCherry-positive population seems to be heterogeneous in complexity and granularity, suggesting the presence of different mCherry-positive cell types or even injury-specific cellular modifications.

Finally, it should be noted that the observed trends are reproducible, as this data is representative of multiple independent experiments (4), with a high statistical significance (****$p < 0.0001$) at 7 dpi, and that these data underscore the robustness of the injury-induced cellular response.

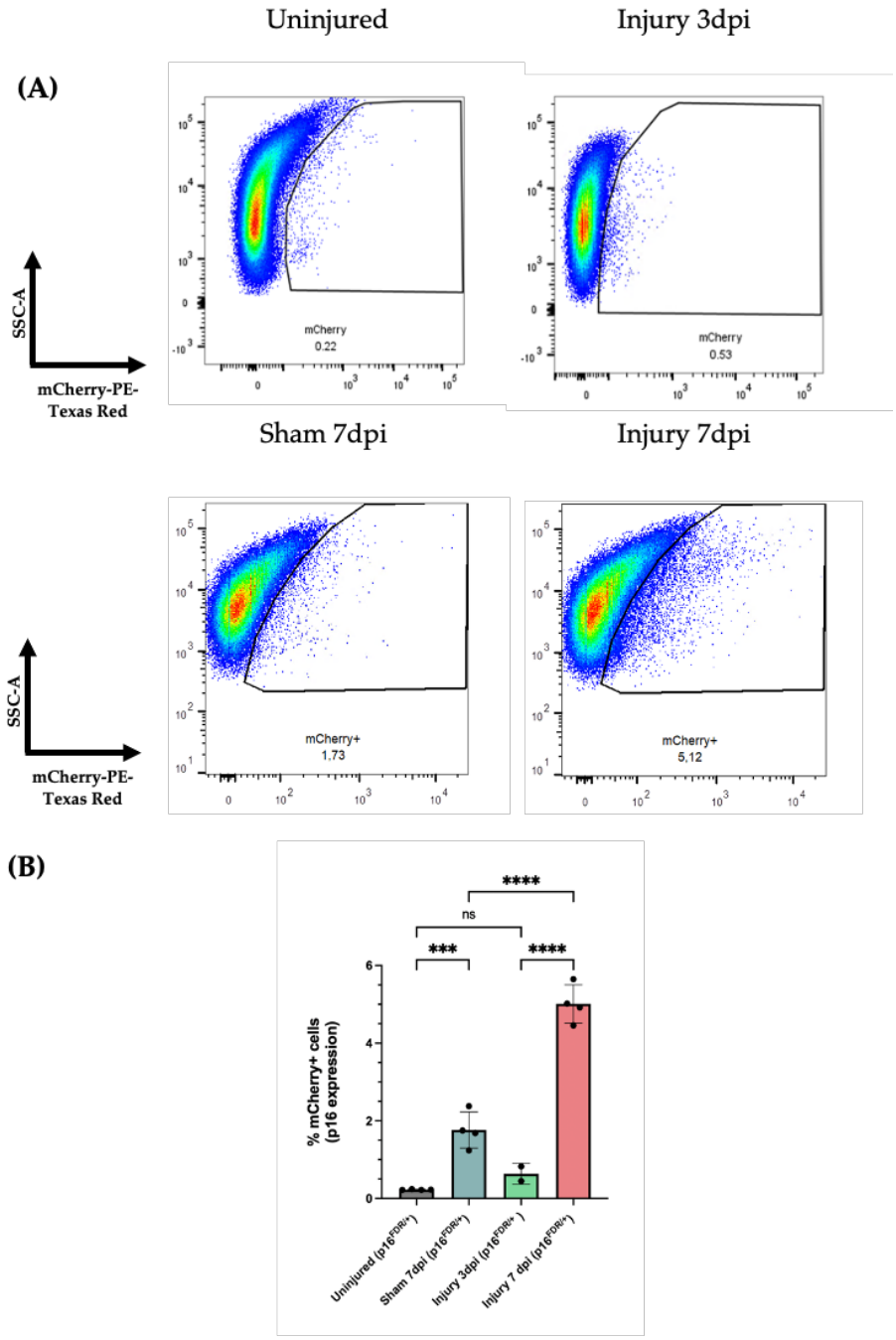

Figure 3.4- Spinal cord injury induces a significant increase in mCherry-positive cells at 7 but not 3 days post-injury **(A)** Representative flow cytometry dot plots showing mCherry expression versus side scatter area (SSC-A) in cell populations under different conditions: uninjured, sham 7 dpi, injured 3 and 7 dpi. These plots demonstrate an increase in mCherry-positive cells following injury, with the most pronounced effect at 7 dpi. Data shown is from one representative experiment (n=1 for each condition) out of multiple experiments conducted (*n*=2-4). **(B)** Quantification of mCherry-positive cells across different conditions. The graph shows a significant increase in the percentage of mCherry-positive cells at 7 dpi compared to uninjured, sham, and 3 dpi conditions. No significant difference is observed at 3 dpi compared to controls. Data are presented as means ± SEM, based on *n* =2-4 independent experiments per group, each dot in the graph represents data from a single animal. Statistical analysis was performed using one-way ANOVA with Bonferroni's multiple comparisons test (95% confidence interval). Statistical significance is indicated as follows: *p < 0.05, **p < 0.01, ***p < 0.001, ****p < 0.0001.

3.3 Characterization of the injury-induced p16-positive cell population after a spinal cord injury

We have seen that an injury-specific population of mCherry-positive cells appears upon a SCI. A couple of important questions almost immediately arise. Why do these cells appear? What role do they play? While all questions are equally significant, we believe that understanding the identity of these cells is the first crucial step in learning more about them. To unravel their identity, we designed an immunohistochemistry panel with canonical markers to identify different cell types in injured SC of $p16^{FDR/+}$mice. Immunofluorescence co-localization of mCherry with other markers for mature neurons (NeuN), activated macrophages/microglia (Iba-1), astrocytes (GFAP), oligodendrocytes (Olig2), pericytes (CD13), and endothelial cells (CD31) was conducted at 7, 15 and 30 dpi **(Figure 3.5 A)**. At 7 dpi, mature neurons (NeuN+) represented the largest proportion of mCherry-positive cells, approximately 30%, followed by oligodendrocytes (13%). Notably, no mCherry-positive endothelial cells or pericytes were observed at this timepoint. While neurons seemed to be the predominant cell type, no statistically significant differences were noted when compared to astrocytes (GFAP+), oligodendrocytes (Olig2+), and microglia (CD11b+) **(Figure 3.5 B)**. These results suggested a trend towards neuronal predominance within the mCherry-positive cell population at 7 dpi.

At 15 dpi, approximately 45% of the mCherry-positive population was neuronal. This proportion was significantly higher compared to the other cell markers examined within the same timepoint, indicating that neurons were the predominant mCherry-positive cell type at 15 dpi. No statistical significance was observed between different cell types at 30 dpi, which suggests that neuronal predominance observed at 15 dpi was lost at this timepoint **(Figure 3.5 B)**. Although not statistically significant, neurons and microglia seem to be the cell types in higher proportions at 30 dpi compared to the other cell types. These results suggested a shift in the cellular composition of mCherry-positive cells at 30 dpi with the loss of neuronal predominance. However, the lack of statistical significance at this timepoint indicates that further investigation may be needed to confirm these trends. We also examined the percentage of cells expressing mCherry for each cell type marker at 7, 15, and 30 dpi. However, most of the differences were not significant (see **Figure 3.5 C**). There appeared to be an increase in the proportion of mCherry-positive neurons from 7 to 15 dpi, followed by a slight decrease at 30 dpi. The microglial/mCherry population seemed to increase from 15 to 30 dpi. Both mCherry-positive astrocytes and oligodendrocytes showed a tendency to decrease over time. This decrease was significant from 7 to 15 dpi in the oligodendrocyte/mCherry population and maintained at 30 dpi as no statistical differences were found. Both endothelial cells and pericytes remained the same throughout all three timepoints. From this analysis, we can deduce that there are dynamic changes in some populations of mCherry-positive cells across different timepoints.

Altogether, our results indicate that neurons comprise the majority of mCherry-positive cells at 7 and 15 dpi, with this predominance being statistically significant when compared to all other cell types at the latter timepoint. By 30 dpi, the clear neuronal predominance is no longer observed, indicating that mCherry-positive cell types exhibit time-dependent changes.

(A) **Endothelial cells and Pericytes**

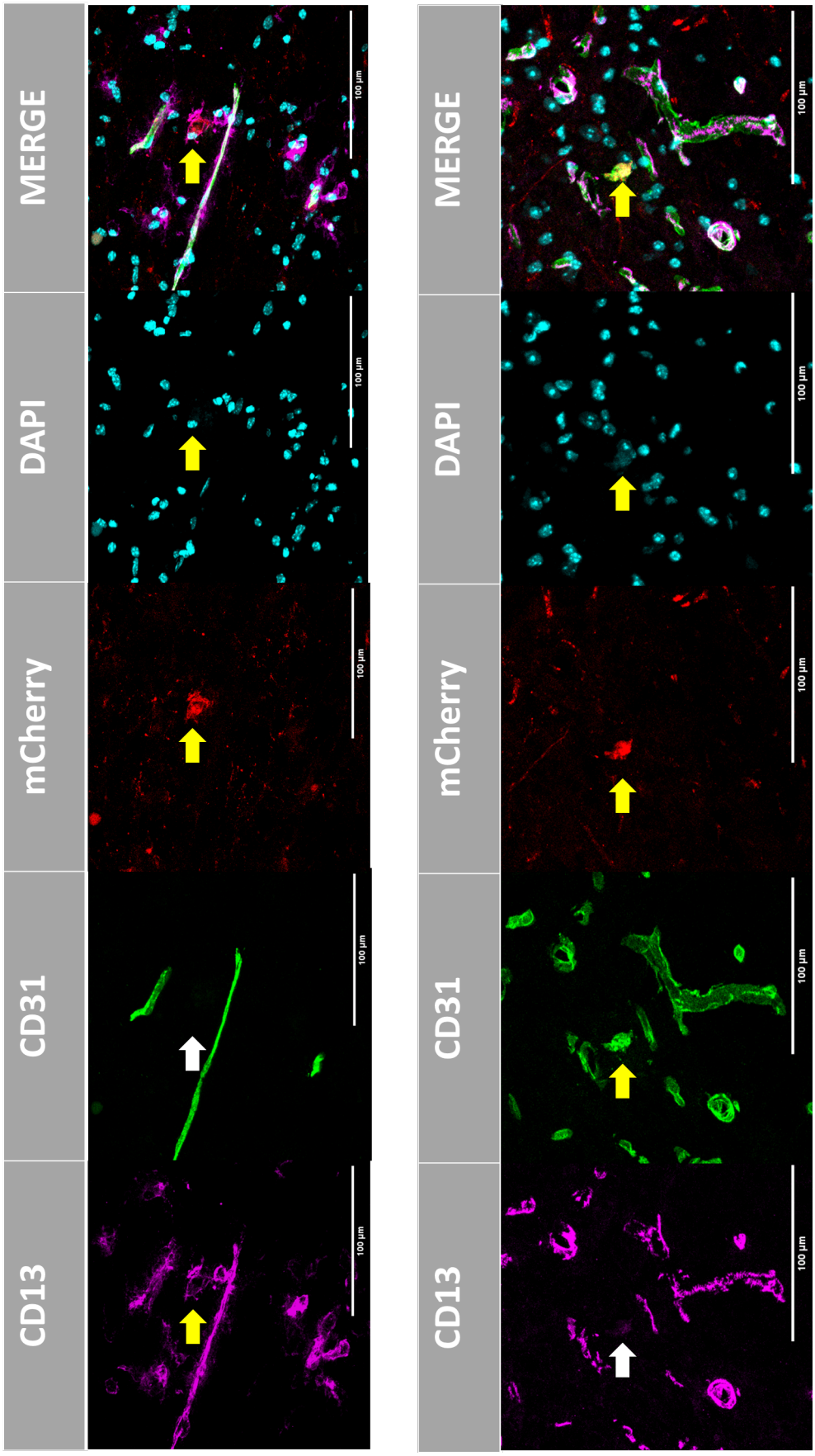

(A) **Astrocytes and Oligodendrocytes**

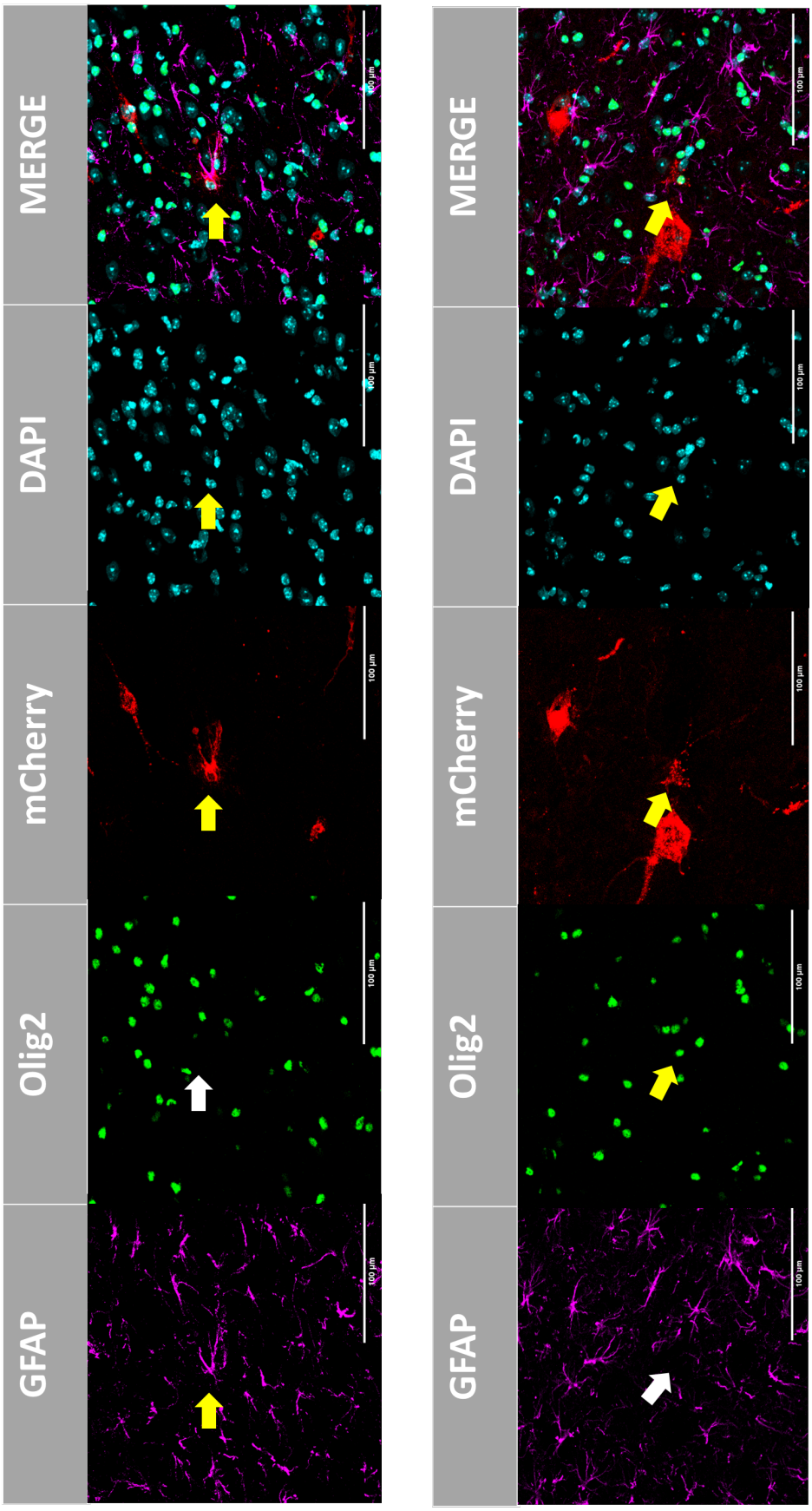

(A)

Mature neurons and Microglia

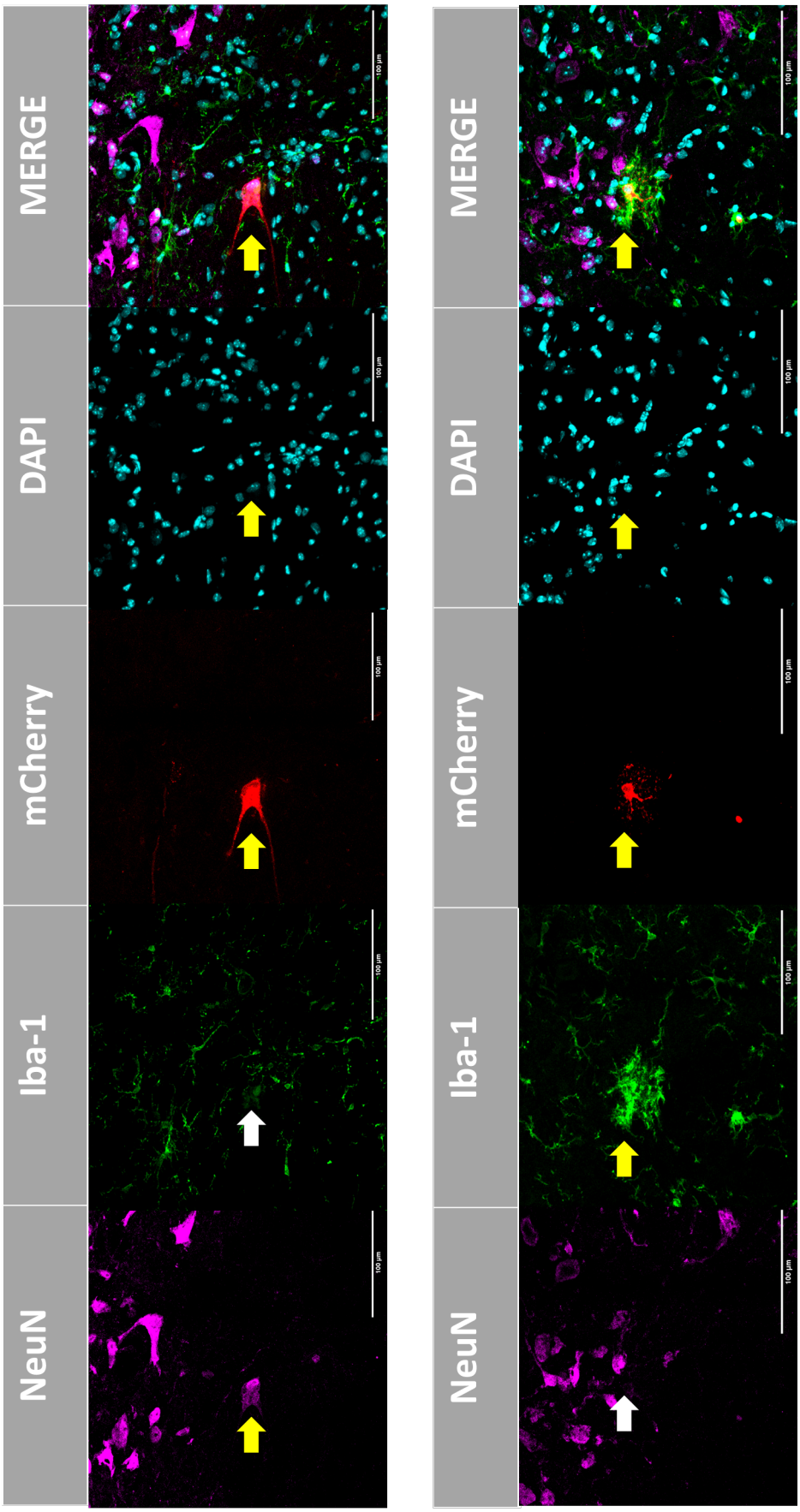

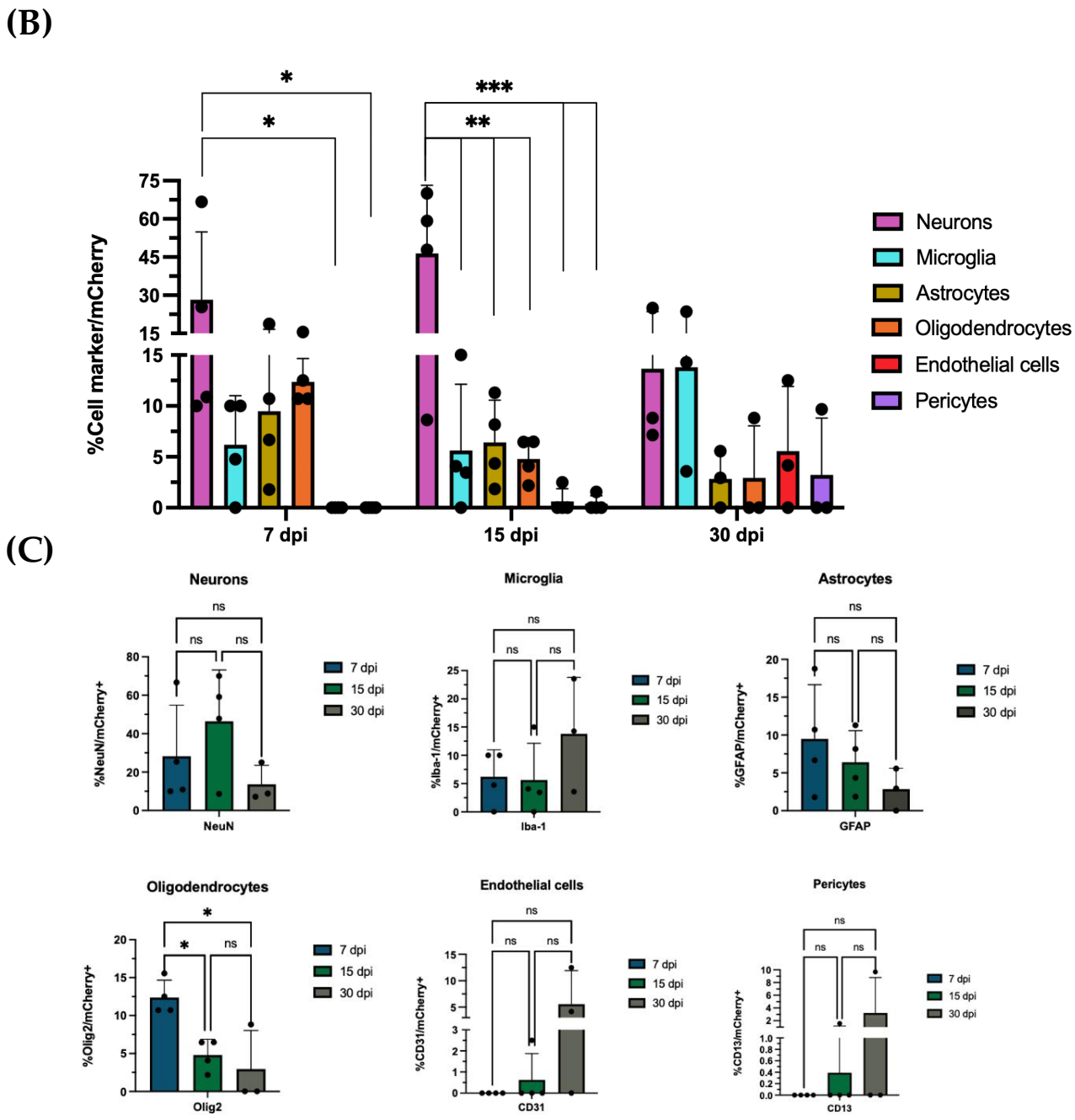

Figure 3.5- Neuronal predominance of mCherry-positive cells is observed at 15 dpi. A) Representative images of the immunohistochemistry performed at 7, 15 and 30 dpi for each pair of cell markers (IHC were performed by groups of markers.) Images show the co-localization of mCherry with various cell markers: CD31 (endothelial cells)/CD13 (pericytes), GFAP (astrocytes)/Olig2 (oligodendrocytes), NeuN (mature neurons)/Iba-1 (microglia), at 15 dpi. Scale bar: 100 μ m, 20x magnification. Yellow arrows point to Co-localization, and white arrows no Co-localization. **B)** Quantification of mCherry-positive cells expressing different markers. Bar graph showing the percentage of mCherry-positive cells co-expressing cell markers at 7, 15, and 30 dpi. A significant neuronal predominance (NeuN+) is observed at 15 dpi, followed by a shift towards increased microglial (Iba-1+) presence at 30 dpi. **C)** Temporal profile of mCherry-positive cells for each cell marker. Bar graphs depicting the percentage of mCherry-positive cells for each cell marker at 7, 15, and 30 dpi. There is an increase in the proportion of mCherry-positive neurons from 7 to 15 dpi, followed by a slight decrease at 30 dpi. The microglial/mCherry population seems to increase from 15 to 30 dpi. Both mCherry-positive astrocytes and oligodendrocytes show a tendency to decrease over time. Data are presented as means ± SEM, based on n =3-4, each dot in the graph represents data from a single animal. Statistical analysis was performed using one-way ANOVA with Bonferroni's correction (95% confidence interval). Statistical significance is indicated as follows: *$p < 0.05$, **$p < 0.01$, ***$p < 0.001$.

To validate and possibly expand on previous IHC findings, we aimed to characterize the mCherry-positive cell population using our optimized flow cytometry protocol. This experiment was conducted on sham and injured $p16^{FDR/+}$mice at 7 dpi. This timepoint was chosen to maximize the representation of the mCherry-population, as noted in Figure **3.4 B)**. The cell types we aimed to identify were immune cells (CD45+), astrocytes (ACSA-2+), microglia (Tmem119+), macrophages/microglia (CD11b+), neurons (Thy1.2+), pericytes (CD13+) and endothelial cells (CD31+). Most of these cell types correlate with the ones analyzed through IHC. New broad markers, such as immune cells and macrophages/microglia, were added to complement the previous analysis and improve population discrimination. Flow cytometry data is shown with quadrant plots for sham and injury conditions at 7 dpi; the upper right quadrant of each plot represents a double-positive population (cell marker+/mCherry+) **(Figure 3.6 A-G)**. Analysis of the upper right quadrants revealed subtle differences between sham and injury conditions for most cell markers. mCherry-positive astrocytes (ACSA-2+), neurons (Thy1.2+), pericytes (CD13+), and endothelial cells (CD31+) were already present in sham conditions, but some variations in size can be seen in injured conditions **(Figure 3.6. B, E, F, G).** There appeared to be an increase in these populations upon injury. The most noticeable differences were seen in immune cells (CD45+), macrophages/microglia (CD11b+), and microglia (Tmem119+) mCherry-positive cells **(Figure 3.6. A, C, D)**. The injury condition revealed a distinct CD45+/mCherry+ cell population absent in the sham condition, indicating an injury-specific population of immune cells expressing mCherry **(Figure 3.6. A)**. Microglia (Tmem119+) showed similar results with injury-specific populations of microglia cells that express mCherry **(Figure 3.6 C).** In the macrophages/microglia (CD11b+) mCherry-positive population, we observed a small population in the sham condition that increased in the injury condition **(Figure 3.6 D)**. Interestingly, in the injury condition, two distinct populations of CD11b+/mCherry+ cells can be seen: CD11b-low (left in the CD11b axis) and CD11b-high (far right in the CD11b axis) **Figure 3.6 D)**. Tmem119 is a microglia-biased marker. However, CD11b labels both macrophages and microglia; these two markers were chosen to be able to differentiate between microglia (Tmem119+ and CD11b+) and macrophages (Tmem119– and CD11b+) [53]. The CD11b-high population did not appear in the microglia (Tmem119+)/mCherry+ right upper quadrant **(Figure 3.6 C)**, only in the microglia/macrophages (CD11b+)/mCherry+ quadrant **(Figure 3.6 D)**, indicating that the CD11b-high population was Tmem119-/CD11b+ cells. These results suggested that the CD11b-low population likely represents resident microglia (Tmem119+/CD11b+) that upregulate mCherry expression upon injury and that the CD11b-high population being Tmem119-/CD11b+ likely represented infiltrating macrophages that strongly express mCherry upon injury. This suggests the appearance of an injury-specific population p16-mCherry macrophages. It is important to note that both macrophages and microglia can be labeled with CD45+ as these cells also belong to the immune compartment **(Figure 3.6 A)**. Moreover, it is important to recognize that this injury-specific population can also contain other immune cells such as T cells (CD45+). A bar graph was generated to quantify the percentage of mCherry cells positive for the different cell markers in the injured condition. The highest percentage of mCherry-positive cells were found to be neurons (Thy1.2+), followed by mCherry-positive astrocytes (ACSA-2+), which was consistent with IHC results from the same timepoint **(Figure 3.6 H and 3.5 B).**

However, we acknowledge the limitation that a proportion of Thy1.2+ cells may also include CD45+ cells, as T cells are also positive for Thy1.2. Nevertheless, our results suggested that, although not statistically significant, within the population of mCherry-positive cells the majority are neurons (Thy1+/CD45-) when compared to immune cells (Thy1-/CD45+) and other mCherry-positive cells (Thy1-/CD45-) **(Figure 3.7 C and D.).** These results also confirm the presence of an injury-specific mCherry immune population, as no immune compartment is observed in sham injury mice within the mCherry-population **(Figure 3.7 C and D.)**

In contrast with IHC results **(Figure 3.5, B)**, where no endothelial cells and pericytes were observed at this timepoint, a small percentage of these cells were mCherry-positive through flow cytometry analysis **(Figure 3.6, H)**. Nonetheless they showed the lowest percentages. These differences can be due to the higher sensitivity of flow cytometry techniques in detecting rare populations that might be missed in limited tissue detections examined in IHC. Additionally, flow cytometry has a wider dynamic range, allowing it to detect very low or very high marker expression levels. Finally, in IHC the two-dimensional analysis of 10 um tissue sections can lead to the loss of cell integrity that can be present in a different plane of the section, a problem circumvented by flow cytometry as it analyses whole cells of the dissected tissue. Also complementing previous IHC results, a proportion of mCherry-positive immune cells, possibly macrophages, was observed. These results indicate that there is indeed an immune compartment in the mCherry-positive cell population, but the majority of these population appears to be represented by neurons at 7 dpi.

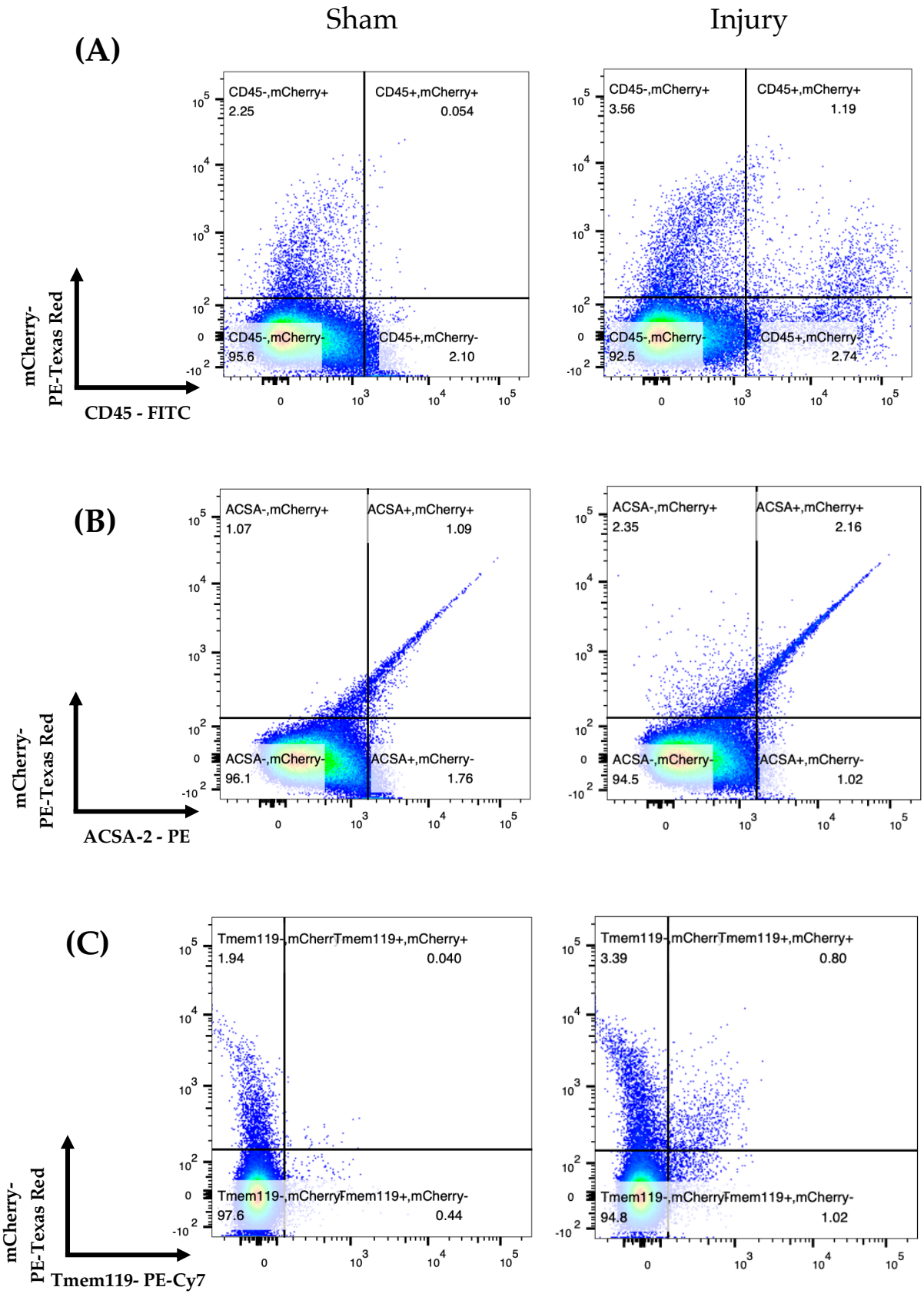
Sham
Injury
(A)
CD45-,mCherry+
2.25
CD45+,mCherry+
0.054
CD45-,mCherry-
95.6
CD45+,mCherry-
2.10
CD45-,mCherry+
3.56
CD45+,mCherry+
1.19
CD45-,mCherry-
92.5
CD45+,mCherry-
2.74
mCherry-
PE-Texas Red
CD45 - FITC
(B)
ACSA-,mCherry+
1.07
ACSA+,mCherry+
1.09
ACSA-,mCherry-
96.1
ACSA+,mCherry-
1.76
ACSA-,mCherry+
2.35
ACSA+,mCherry+
2.16
ACSA-,mCherry-
94.5
ACSA+,mCherry-
1.02
mCherry-
PE-Texas Red
ACSA-2 - PE
(C)
Tmem119-,mCherrTmem119+,mCherry+
1.94
0.040
Tmem119-,mCherryTmem119+,mCherry-
97.6
0.44
Tmem119-,mCherrTmem119+,mCherry+
3.39
0.80
Tmem119-,mCherryTmem119+,mCherry-
94.8
1.02
mCherry-
PE-Texas Red
Tmem119- PE-Cy7

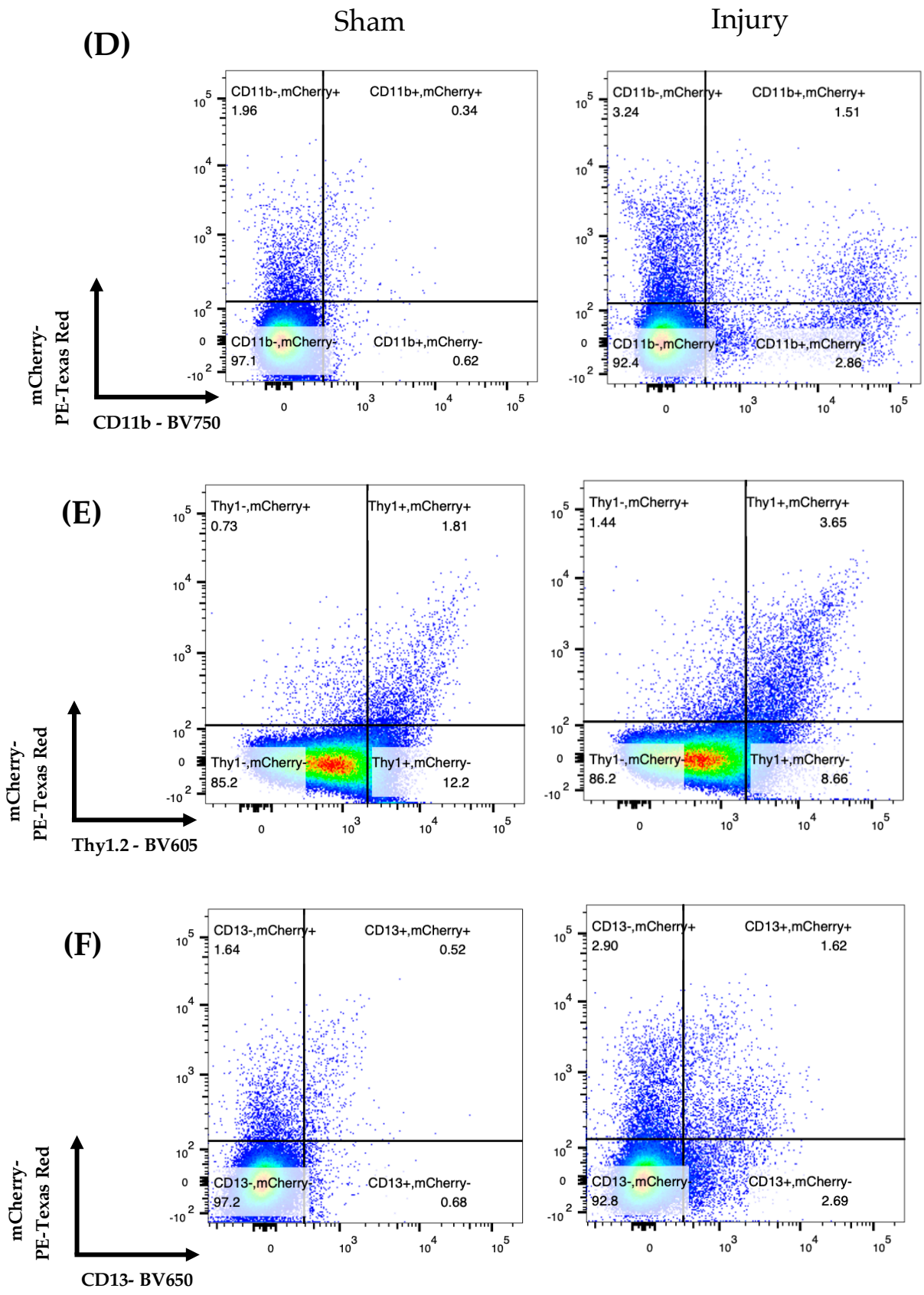
Sham
Injury
(D)
CD11b-,mCherry+
1.96
CD11b+,mCherry+
0.34
CD11b-,mCherry-
97.1
CD11b+,mCherry-
0.62
CD11b-,mCherry+
3.24
CD11b+,mCherry+
1.51
CD11b-,mCherry-
92.4
CD11b+,mCherry-
2.86
mCherry-
PE-Texas Red
CD11b - BV750
(E)
Thy1-,mCherry+
0.73
Thy1+,mCherry+
1.81
Thy1-,mCherry-
85.2
Thy1+,mCherry-
12.2
Thy1-,mCherry+
1.44
Thy1+,mCherry+
3.65
Thy1-,mCherry-
86.2
Thy1+,mCherry-
8.66
mCherry-
PE-Texas Red
Thy1.2 - BV605
(F)
CD13-,mCherry+
1.64
CD13+,mCherry+
0.52
CD13-,mCherry-
97.2
CD13+,mCherry-
0.68
CD13-,mCherry+
2.90
CD13+,mCherry+
1.62
CD13-,mCherry-
92.8
CD13+,mCherry-
2.69
mCherry-
PE-Texas Red
CD13- BV650

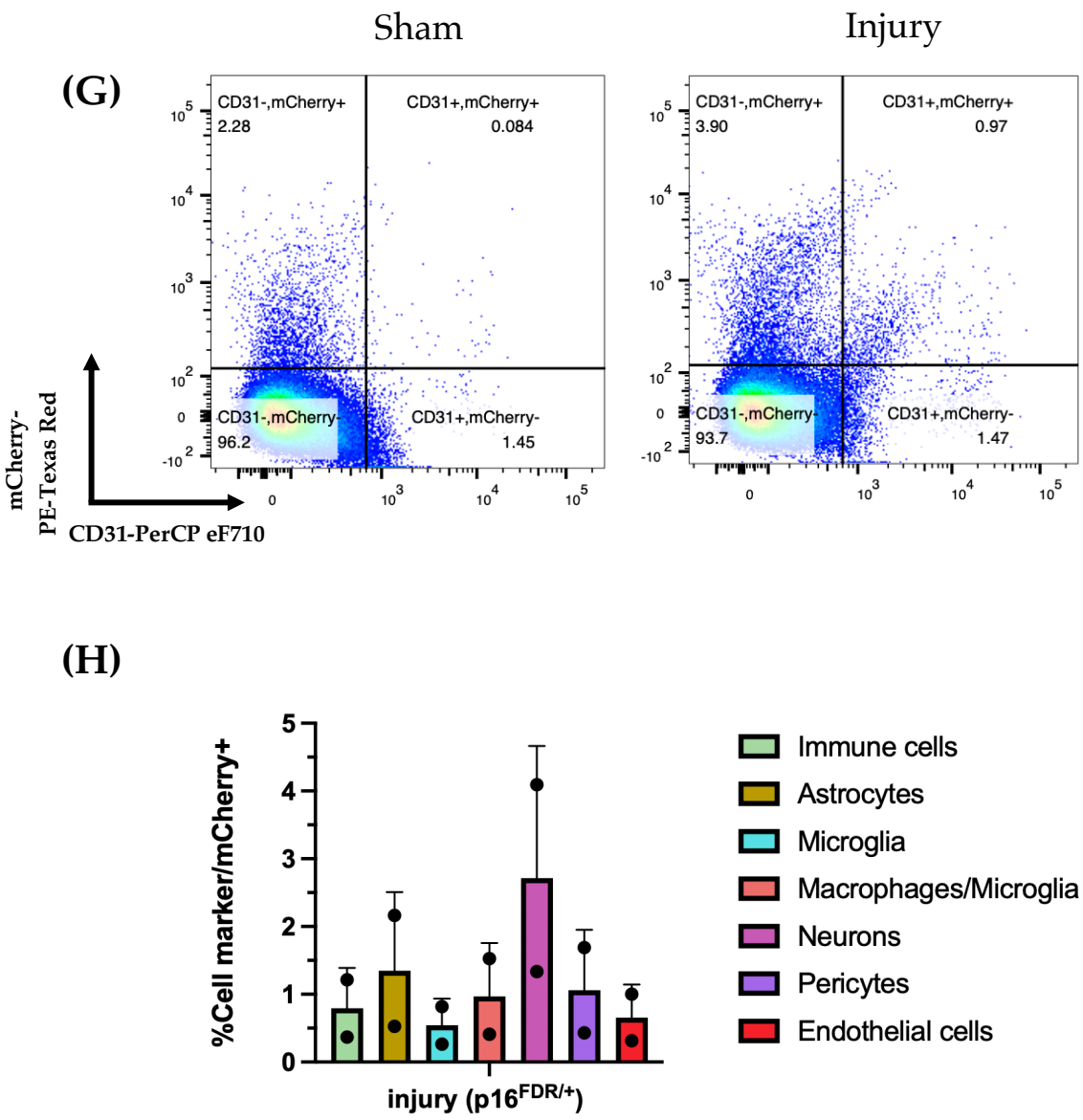

Figure 3.6- Flow cytometry reveals injury-specific mCherry-positive immune cell population, complementing previous immunohistochemistry findings. Flow cytometry dot plots showing the distribution of mCherry-positive cells against various cell markers **A)** immune cells (CD45+); **B)** astrocytes (ACSA-2); **C)** microglia (Tmem119+); **D)** macrophages/microglia (CD11b+); **E)** neurons (Thy1.2+); **F)** pericytes (CD13+) and **G)** endothelial cells (CD31+) in sham and injury conditions at 7 dpi. The upper right quadrant represents the double-positive population for each marker and mCherry. Each dot represents a single cell, and the axes show fluorescence intensity for the respective markers. Dot plots show shifts in mCherry-positive cell populations following injury, with a notable increase in immune cells (CD45+), macrophages/microglia (CD11b+), and microglia (Tmem119+) mCherry-positive cells. **H)** Percentage of mCherry-positive cells for different cell markers in the injury condition at 7 dpi. Quantification of mCherry-positive cells in the injury condition reveals neurons (Thy1.2+) as the highest percentage, followed by astrocytes (ACSA-2+), immune cells (CD45+), and other cell types. Bars represent the mean percentage of mCherry-positive cells for each marker. Error bars indicate the standard error of the mean (SEM). No statistical testing was performed.

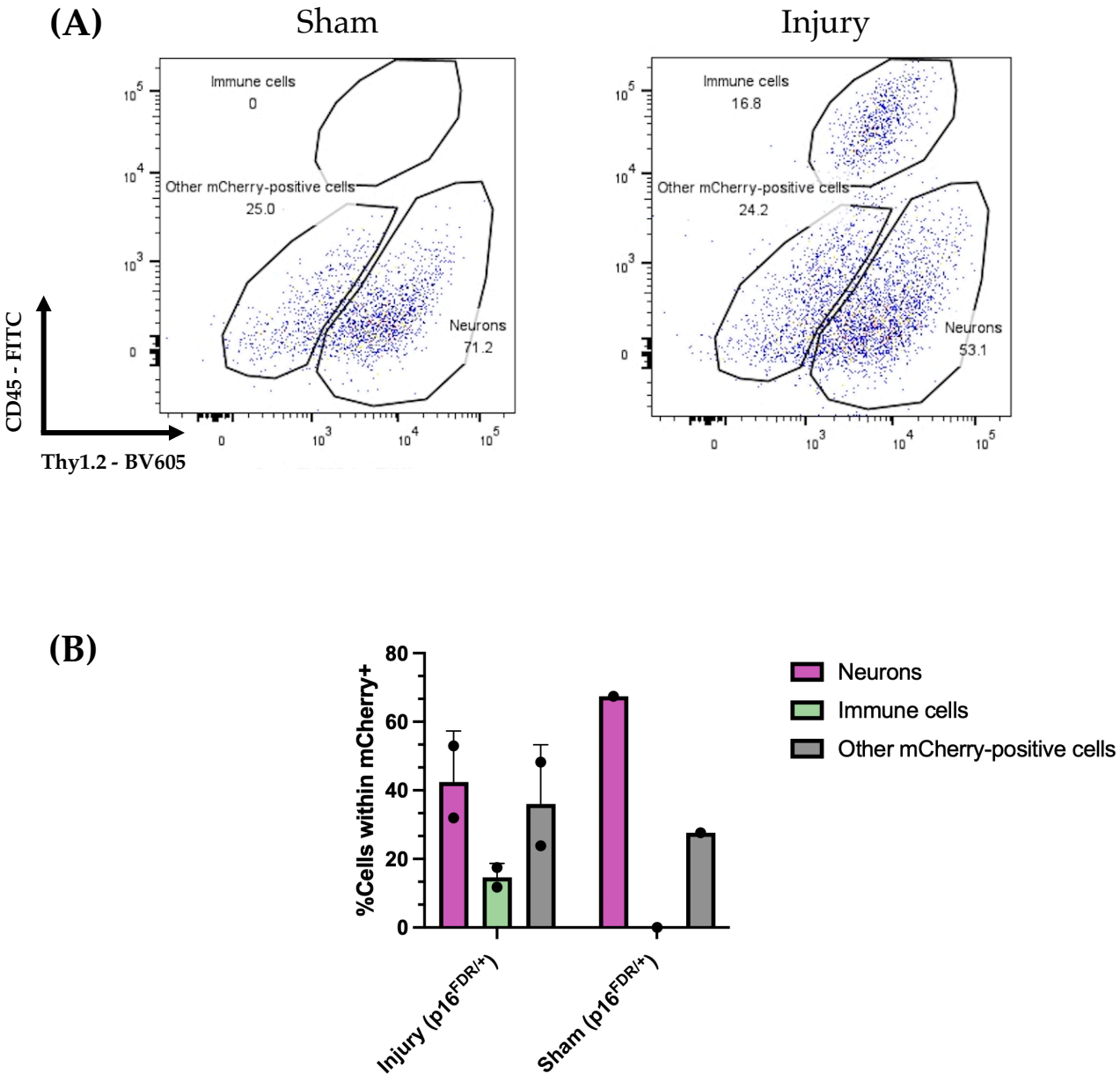

Figure 3.7- The Majority of p16-mCherry positive cells are neurons (Thy1.2+/CD45-)

A) Sham vs injury dot plots with % neurons (Thy1.2+/CD45-), immune cells (Thy1.2+/CD45+) and other mCherry-positive cells (Thy1.2-/CD45-) within mCherry-positive cells. Comparison of sham vs. injury conditions highlights the emergence of a distinct injury-specific mCherry-positive immune cell population specifically. **B)** Quantification of mCherry-positive neurons (Thy1.2+/CD45-), immune cells (Thy1.2+/CD45+), and other cell types (Thy1.2-/CD45-) in sham and injury conditions at 7 dpi. Data shows that most of the mCherry population appears to be Thy1.2-positive and CD45-negative (neurons). Bars represent the mean percentage of mCherry-positive cells for each population. Error bars indicate SEM. No statistically significant differences were observed between injury populations (ns, $p > 0.05$, one-way ANOVA with Bonferroni correction). *n* =1-2

3.4 Injury-induced p16-positive cells do not seem to respond to the ABT senolytic treatment

After establishing the nature of mCherry-positive cells, it is important to remember that p16 is a well-known marker of senescent cells (SeCs). One of the hallmarks of SeCs is their apoptosis resistance through the expression of anti-apoptotic proteins such as BCL-2. Our lab's previous research revealed that SeCs, especially those positive for SA-β-gal, were induced upon injury and accumulated at the injury periphery over time and were not removed unless mice were treated with senolytic drugs, such as ABT-263/Navitoclax. ABT-263 is an BCL-2 inhibitor that induces apoptosis of SeCs. Interestingly, independent results from our lab using the p16-FDR model indicated that mCherry/p16-positive cells displayed a transient profile **(see Annex, Figure 6.2)**, in contrast with the SA-β-gal cumulative profile previously described. This raised three fundamental questions that we wanted to tackle. How come SeCs, traditionally apoptosis-resistant, are present transiently? Are mCherry/p16-and SA-β-gal-positive cells different populations? Or are mCherry/p16 cells transit to a SA-β-gal-positive state? Co-stainings of SA-β-gal with immuno detection of mCherry are quite challenging due to the different signal-detection methods. SA-β-gal is detected by colored blue contrast in brightfield microscopy and mCherry with fluorescence microscopy, making it difficult to capture both signals simultaneously with different optical setups being required. Additionally, observing both signals in a traditional brightfield microscope, with monocolour cameras, makes it hard to distinguish the real SA-β-gal signal, as it appears indifferent shades of grey. To address the possibility of mCherry-positive cells also being the same population as SA-β-gal-positive cells with the resources available at the time, we decided to treat p16-FDR mice with ABT-263 from 5 to 14 dpi and collect the tissue at 15 dpi **(Figure 3.8 A)**. Stainings for SA-β-gal and mCherry were then performed on different sets of sections in the ABT- and vehicle-treated groups **(Figure 3.8.C).** Firstly, we wanted to confirm that injured p16-FDR mice treated with ABT-263 showed the expected reduction in SA-β-gal-positive cells, which was based on published results [13]. Secondly and most importantly, we also aimed to see if p16 cells suffered a reduction after ABT treatment, following the same pattern as SA-β-gal. This would suggest they comprise the same population of cells. There were no statistically significant differences in the BMS score between treated and vehicle groups, however, ABT-treated mice seemed to present a better locomotor recovery as expected. **(Figure 3.8 B).** In the treated group, there was a significant decrease in SA-β-gal-positive cells compared to the control group **(see Figure 3.8 D)**. The reduction in SA-β-gal-positive cells in the treated group is visually evident in the staining images, observable by the naked eye **(Figure 3.8 C)**. These results indicate that the ABT treatment was effective as expected. However, when comparing the percentage of mCherry-positive area, there were no noticeable differences between the two groups, suggesting that the treatment did not affect the number of these cells **(Figure 3.8 D)**. Although images showed a slight increase in the percentage of mCherry-positive area in the treated group, this only reflected a tendency in the respective quantifications **(Figure 3.8 .C) and D))**. We can conclude that the ABT treatment results in a significant decrease of SA-β-gal positive cells but not in the percentage of mCherry-positive area. Moreover, this data suggests that mCherry-positive cells and SA-β-gal cells are not the same population of cells. However, we cannot discard the possibility of co-localization of both markers in a small

population of cells that may respond to the treatment, but whose elimination is not statistically significant in relation to the total mCherry-positive population. The major limiting factor is the small sample size which can make it challenging to detect subtle changes in area percentage, especially if the overall number of mCherry-positive cells is low.

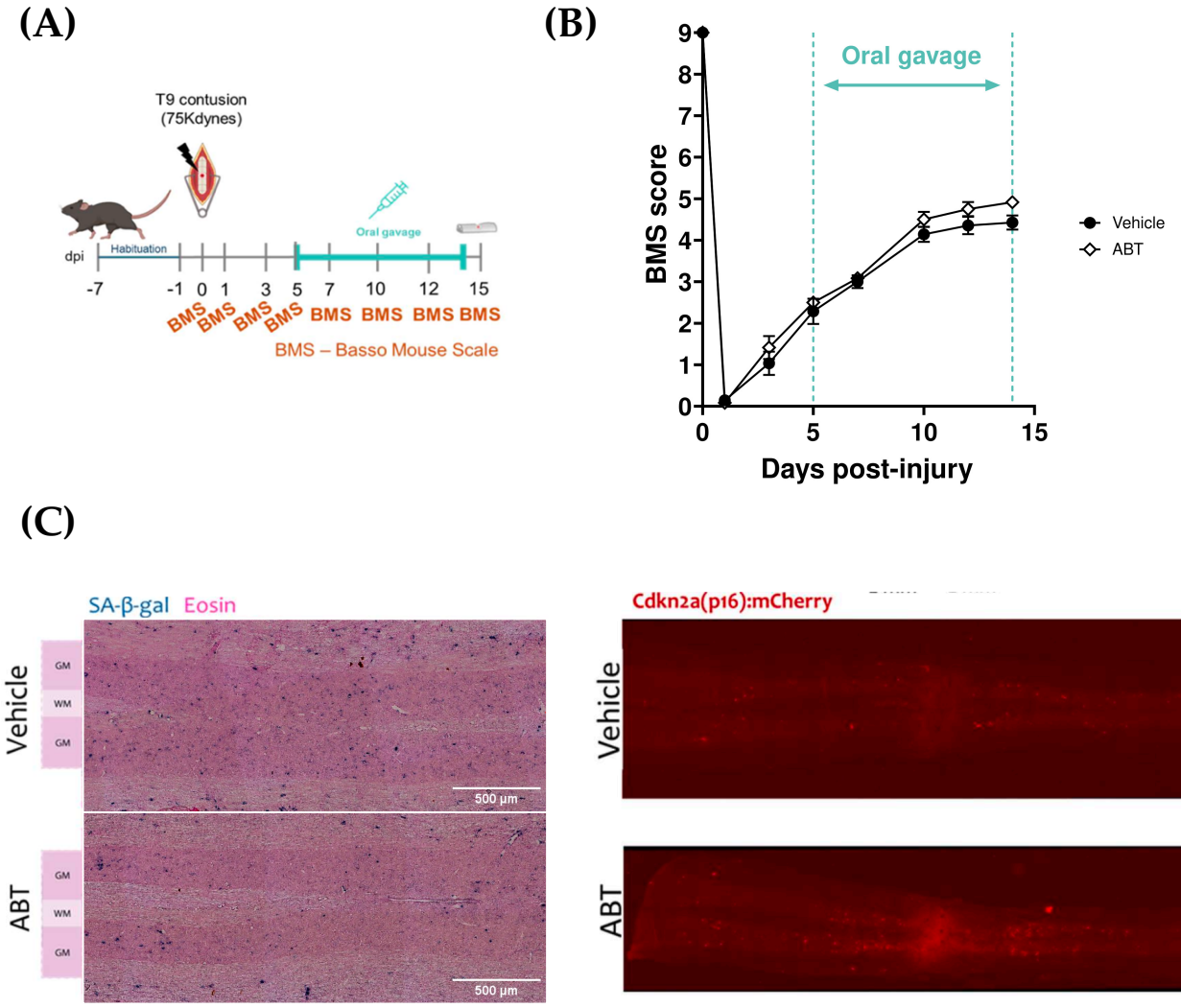

(D)

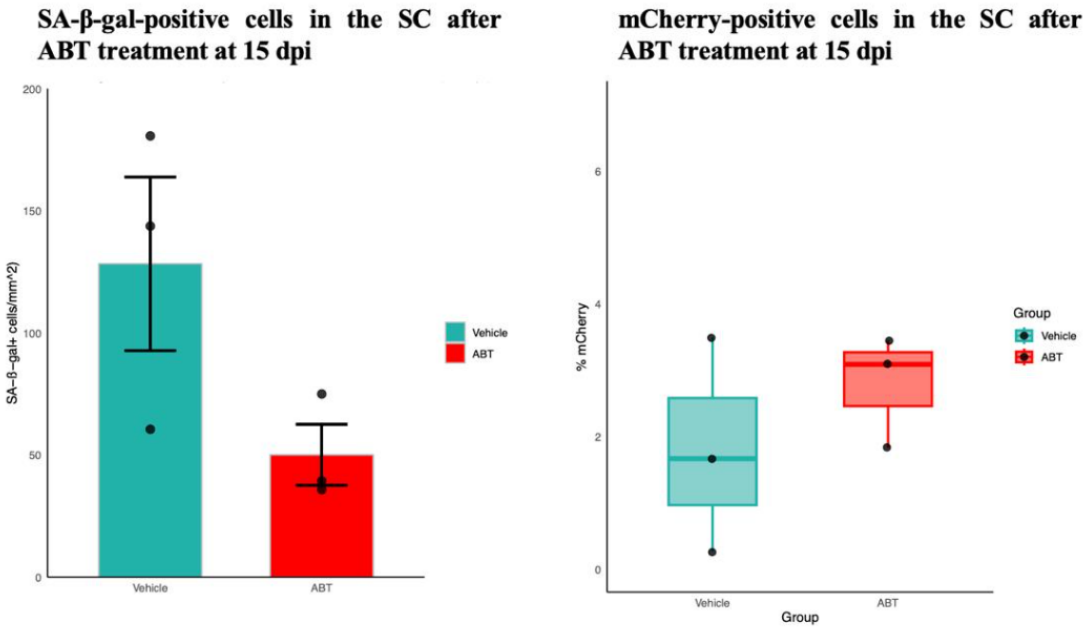

Figure 3.8- ABT-263 promotes the depletion of SA-β-gal-positive cells but not mCherry-positive cells in the injured spinal cord at 15 dpi. (A) Schematic representation of the experimental protocol. **(B)** Basso Mouse Scale (BMS) scores of vehicle-treated and ABT-263-treated mice over time after spinal cord injury. No significant differences were observed between the two groups n =3 female $p16^{FDR/+}$ mice per group. **(C)** Representative images of SA-β-gal and mCherry staining in the spinal cord (SC) of vehicle-treated and ABT-263-treated mice at 15 days post-injury (dpi) (n =1 female per group). Scale bar = 500μm **(D)** Quantification of SA-β-gal-positive cells and percentage of mCherry-positive area in the SC after vehicle or ABT-263 treatment at 15 dpi. ABT-263 treatment significantly reduced the number of SA-β-gal-positive cells compared to vehicle treatment. No significant difference was observed in the number of mCherry-positive cells between the two groups. Data are presented as mean ± SEM, n =3 female $p16^{FDR/+}$ mice per group. Statistical analysis was performed using a two-way ANOVA with Bonferroni correction for (B) (*p<0.05) and unpaired t-tests for D) (*p<0.05, p=0.012 for SA-β-gal; ns = not significant for mCherry-positive area).

3.5 What is the role of the injury-induced p16-positive cell population?

So far, in this exciting and surprising plot, we have seen that most of the mCherry-positive cell population is constituted by neurons. We also saw, in independent data, that these cells present a temporary profile being eventually eliminated, and not much is known regarding their senescence nature. The lingering question is why? Why do these p16-positive cells appear upon injury? Why are neurons activating p16? What is their role? Why do they eventually disappear? We performed a couple of experiments to begin answering these questions.

3.5.1 What happens when we eliminate p16-mCherry-positive cells?

To better understand the role of these p16-mCherry cells in the SC after SCI, we decided to conduct a genetic ablation study. The lab optimized a Diphtheria toxin (DT) administration protocol that allowed for the targeted elimination of mCherry-positive cells. After SCI, p16-FDR mice were treated twice a week for 10 days starting at 1 dpi with DT according to the experimental design depicted in **Figure 3.9 (A)**. Their locomotor behavior was also assessed at specific timepoints (**Figure 3.9 C)**). We first confirmed the successful elimination of mCherry-positive cells. DT administration resulted in a significant decrease in percentage of mCherry-positive area in injured $p16^{FDR/+}$ mice treated with DT compared to PBS-treated $p16^{FDR/+}$ controls at 10 dpi, confirming the efficient targeted elimination of mCherry-positive cells (**Figure 3.9, B)**). BMS scores showed a significant decline in locomotor function in DT-treated $p16^{FDR/+}$ mice compared to PBS-treated $p16^{FDR/+}$ and *wt* p16-FDR ($p16^{+/+}$) mice at 15 dpi (**Figure 3.9, C)**). This decline was specific to DT-treated injured mice carrying the cassette. Two important controls were included to allow this statement. *Wt* p16-FDR ($p16^{+/+}$) mice do not have the cassette and, therefore, do not respond to DT treatment. As expected, DT treatment did not impact their post-injury locomotor behavior. PBS-treated $p16^{FDR/+}$ mice contain the cassette but were treated with PBS instead of DT, and no alteration was observed in their locomotor behavior. This locomotor impairment is transient as there were no differences in BMS scores after 15 dpi. As a conclusion, we were able to demonstrate that DT administration promotes the effective and targeted elimination of mCherry-positive cells in injured $p16^{FDR/+}$ mice. Moreover, the selective elimination of these cells results in a transient locomotor impairment at 15 dpi.

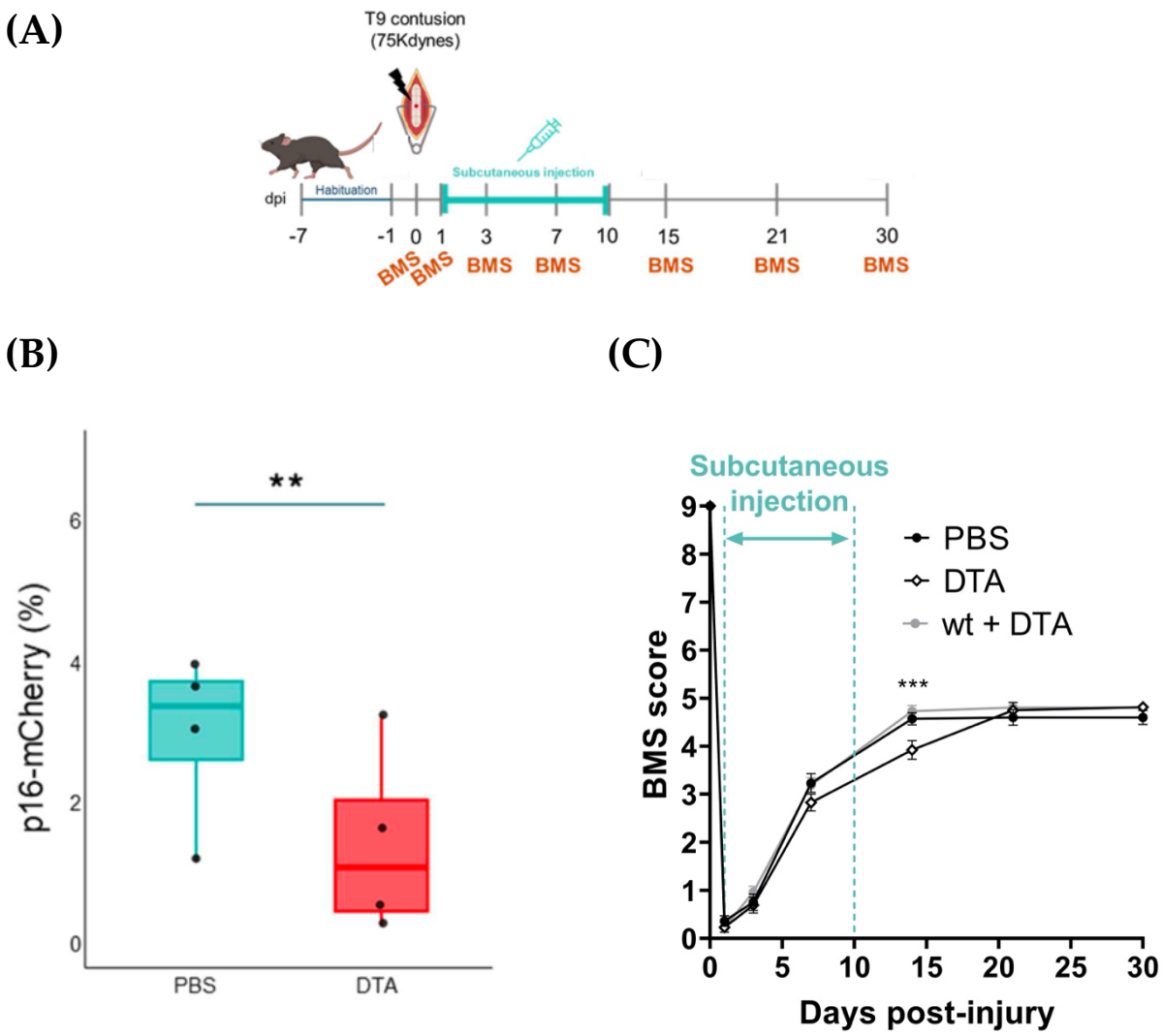

Figure 3.9- Selective elimination of mCherry positive cells in p16-FDR mice after spinal cord injury results in transient locomotor impairment at 15 dpi. (A) Schematic representation of the experimental design. Mice were administered 0.5 ng/g BW of DT or PBS via subcutaneous injection twice a week for 10 days, resulting in a total of four administrations. After SCI, animals were randomly assigned to three treatment groups: DT-treated p16$^{(FDR/+)}$ mice, PBS-treated p16$^{(FDR/+)}$ mice, and DT-treated wt p16-FDR (p16$^{+/+}$) mice. **(B)** Quantification of mCherry-positive cells in the spinal cord of injured p16$^{(FDR/+)}$ mice treated with DT or PBS at 10 dpi. DT treatment significantly reduced the number of mCherry-positive cells compared to PBS treatment. **(C)** BMS scores over time for DT-treated p16$^{(FDR/+)}$ mice, PBS-treated p16$^{(FDR/+)}$ mice, and DT-treated wt p16-FDR (p16$^{+/+}$) mice. DT-treated p16$^{(FDR/+)}$ mice showed a significant reduction in BMS scores at 15 dpi compared to both control groups. No differences were observed at later time points. Data are presented as mean ± SEM (n = 8-13 female mice per group). Statistical analysis was performed using unpaired t-tests for (B) (**p<0.01) and two-way ANOVA with Bonferroni correction for (C) (*p<0.05).

3.5.2 What are p16-mCherry cells expressing: sorting and bulk RNA sequencing of p16-mCherry positive cells

We have discovered that upon injury a transient population of p16-mCherry positive cells is induced and that is enriched for neurons. Moreover, when we selectively eliminate these cells before 15 dpi, after which they naturally disappear, injured mice experience temporary locomotor impairment, returning to normal levels after 15 dpi. The fundamental question remains, and possibly becomes more intricate: what are the factors that underlie the function of these transient cells?

Using our optimized protocol, we were able to conduct FACS and sort p16-mCherry-positive cells and send them for bulk RNA-sequencing for a more in-depth molecular analysis.SC tissue from four injured 7 dpi $p16^{(FDR/+)}$ was processed according to our optimized protocol. We sorted mCherry-positive and mCherry-negative cells from the same animal (control) using the optimized FACS protocol. The timepoint chosen was 7 dpi, as mCherry-positive cells are known to be present at high levels, as demonstrated previously in an independent IHC **(see Annex, Figure 6.2)** and Flow cytometry results **(Figure 3.4)**. The sorting was performed for yield rather than purity, as mCherry-positive cells make up a small percentage of the total cells **(See Annex-Figure 6.2 and Figure 3.4)**.

Our results confirmed the successful sorting **(Table.3.2)**. Despite sorting for yield, we were able to isolate a pure population of p16-mCherry with purity percentages ranging from 90-100% **(Table.3.2).** The percentage of p16-mCherry-positive cells varied between animals (0.6-5%). This variability was expected, as previous results from IHC and flow cytometry also showed high variability in the percentage of p16-mCherry-positive cells between animals **(as seen in Figure 3.4)**. After successful sorting and RNA extraction, we proceeded with bulk sequencing of the p16-mCherry-positive and p16-mCherry-negative populations. We only sequenced three out of the four sorted samples, due to the low number of p16-mCherry-positive cells in the first biological replicate. Additional data on extracted RNA quality and sequencing results can be found in the Annexes section in **table A.1**. Principal component analysis (PCA) showed a clear distinction between p16-mCherry-positive and negative populations in all three biological replicates, with a PC1 higher than 40% **(Figure 3.10).** This means that over 40% of the variance can be is explained by the existence of a p16-mCherry-positive vs negative population. This difference between mCherry populations was also corroborated with a different method, hierarchical clustering analysis. This analysis placed positive and negative p16-mCherry cell populations in different clusters, as expected. Moreover, these results confirmed that the samples were clustered based on p16-mCherry expression and respective transcriptional programs rather than by individual mice. This suggested that p16-mCherry expression is associated with transcriptional differences that are stronger than individual mouse-to-mouse variations.

With these results we can confirm that we can successfully sort and isolate pure and distinct populations. If sorting had not been successful, the samples would have appeared mixed or randomly clustered. Our sorting protocol is also consistent, the group separation is consistent across all biological replicates. Our results also suggest that the expression of mCherry (p16 locus activation) and its transcriptional program is consistent and significant enough to change the overall gene expression profile of the cells, regardless of which mouse they came from. These results are confirmed by two different

and consistent methods, hierarchical clustering produced and the PCA which strengthens the reliability of these findings.

Table 3.2- Cell sorting report for mCherry-positive and mCherry-negative populations from injured spinal cord tissue. This table summarizes the FACS data of sorted samples obtained from four mice (alfa-1 to alfa-4) at 7 dpi. The columns represent the individual mouse identifiers (alfa-1, alfa-2, alfa-3, alfa-4), the number of sorted mCherry-negative cells on the left, the number of sorted mCherry-positive cells on the right, and the percentage of mCherry-positive cells in the total sorted population for each animal on the far right.

	Far Left	Left	Right	Far Right
Alfa 1		mCherry-	mCherry+	
# cells		**369,741**	**16,112**	0.6% mCherry+
Purity		100%	90.2%	
Alfa 2		mCherry-	mCherry+	
# cells		**300,178**	**31,248**	1.5% mCherry+
Purity		na	na	
Alfa 3		mCherry-	mCherry+	
# cells		**196,049**	**65,970**	5% mCherry+
Purity		98%	92.3%	
Alfa 4		mCherry-	mCherry+	
# cells		**335,448**	**44,675**	2.1% mCherry+
Purity		95.5%	90.7%	

(A)

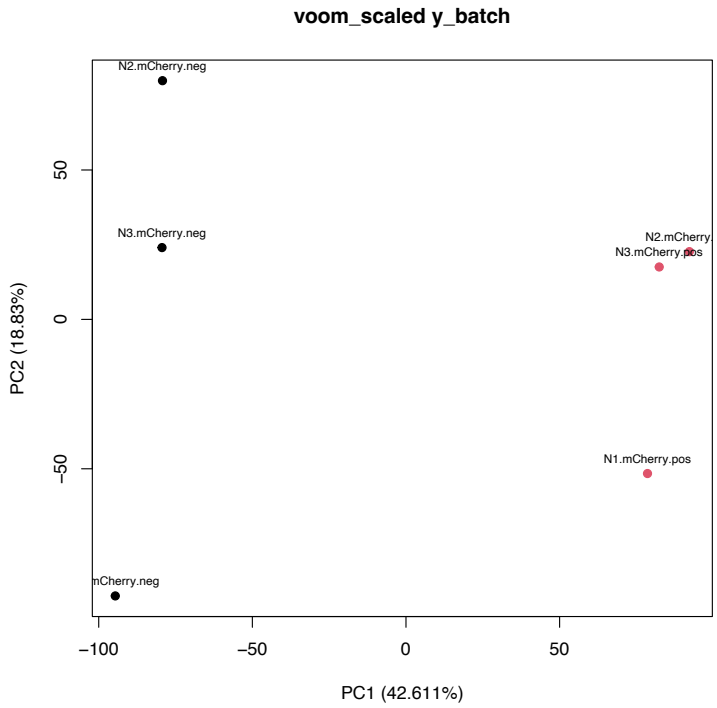

(B)

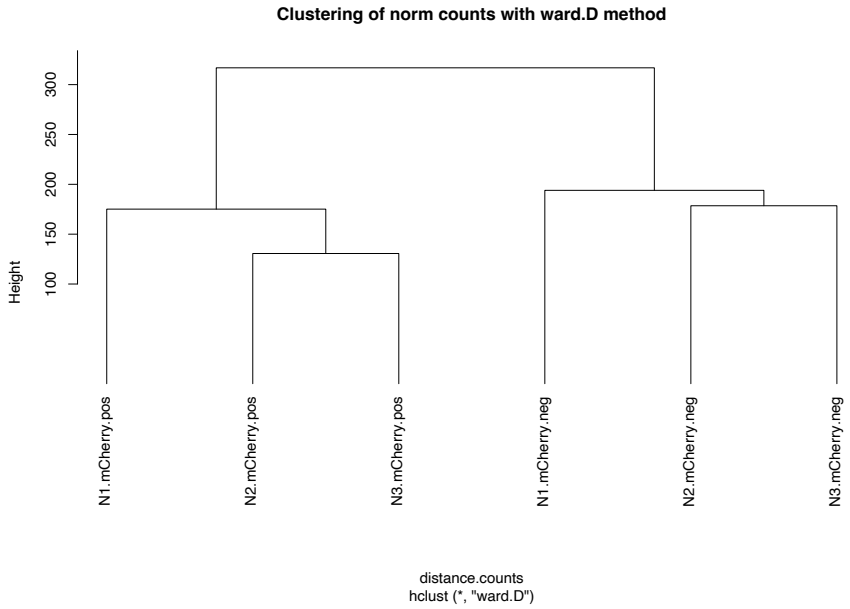

Figure 3.10- Transcriptional profiling reveals distinct gene expression patterns in mCherry-positive cells after spinal cord injury/ PCA and Hierarchical Clustering Reveal Distinct Transcriptional Profiles of mCherry-Positive and Negative Cells (A) Principal Component Analysis (PCA) of RNA-seq data from mCherry-positive and mCherry-negative cells isolated from injured spinal cord at 7 dpi. Each point represents an individual sample (n=3 per group). The first two principal components (PC1 and PC2) account for over 40% of the total variance, demonstrating a clear separation between mCherry-positive and mCherry-negative populations. **(B)** Hierarchical clustering of gene expression profiles from the same RNA-seq data. Samples are grouped based on their transcriptional similarities, showing clear clustering of mCherry-positive and mCherry-negative samples. This analysis confirms the distinct transcriptional profiles of the two populations across biological replicates.

Differential gene expression analysis revealed genes that were significantly upregulated and downregulated in p16-mCherry-positive cells when compared to their negative counterparts. **Figure 3.11 A)** represents a volcano plot with the top 10 upregulated and downregulated genes with the strongest statistical support. *Secreted phosphoprotein 1 (spp1)* was one of the up-regulated genes. Osteopontin (OPN) or Spp1 can be a matricellular protein (bound to the matrix) or secreted [54]. Spp1 is a multifunctional protein involved in cell adhesion, migration, and survival [54], [55]. Additionally, it is expressed in immune cells, mostly macrophages and T cells, promoting cell recruitment to inflammatory sites and its increase promotes the expression of pro-inflammatory cytokines, acting as an immune modulator [55]. Spp1 is also involved in wound-healing and fibrosis processes and can also be related to senescence processes [54], [56]. c*tss*, *ctsd*, *ctsb*, *ctsz* and *ctsa* (Cathepsin-s, d, b, z, a) are also upregulated, these genes encode for cathepsins, a family of lysosomal proteinases. They are found in the lysosomal compartments and are involved in several functions such as protein degradation, energy metabolism, immune responses, and autophagy [57], [58]. Cathepsins have been implicated in senescence processes [59]. In particular, cathepsin b is a known SASP factor [27]. *c1qc*, complement C1q C chain gene, is also upregulated and encodes the C-chain polypeptide of serum complement subcomponent C1q, part of the classical complement activation pathway. This protein is involved in cellular differentiation, intercellular adhesion, chemotaxis, and clearance of apoptotic debris [60] . High levels of C1q have also been associated with senescence of hepatitic livers [61] .
The gene *hexb*, hexosaminidase subunit beta is also upregulated. Hexosaminidase B is the beta subunit of the lysosomal enzyme beta-hexosaminidase that has been shown to be enriched in senescent cells [62], [63]. Lastly, *apoe* is also upregulated, providing instructions to produce apolipoprotein E (APOE). APOE is a multifunctional protein that plays a crucial role in regulating lipid metabolism and cholesterol transport [64]. In the context of spinal cord injury (SCI), APOE has been shown to have neuroprotective functions by promoting neuronal repair and nerve regeneration. Deficiency of APOE leads to increased inflammation and oxidative stress, neuronal apoptosis, and delays in the recovery of locomotor function and tissue repair. APOE expression has also been associated with senescence. Upon senescence, APOE expression increases, driving the loss of proteins from the nuclear envelope [65].

Regarding downregulated genes, several genes found are associated with myelin components. *mbp* encodes for myelin basic protein which is a major component of myelin sheaths, and it is expressed in oligodendrocytes and Schwann cells [66]. *Bcas1* encodes for a breast carcinoma amplified sequence 1 (BCAS1) protein which is a myelin-associated protein expressed mostly in oligodendrocytes and Schwan cells [67]. *Mobp* encodes for a myelin-associated oligodendrocyte basic protein which plays a role in stabilizing myelin sheaths in the CNS [68] .

Altogether, our findings show distinct gene expression differences between mCherry-positive and mCherry-negative cells. Upregulated genes appear to be involved in diverse roles such as immune activity, injury and tissue repair, lysosomal function, and senescence. On the other hand, most of the downregulated genes seem to be related to oligodendrocytes and myelin, possibly suggesting an underrepresentation of oligodendrocytes in mCherry-positive cells. We then performed CIBERSORT analysis to estimate the relative proportion of specific cell types in mCherry-positive and negative populations based on their bulk gene expression profiles. Our results suggested that mCherry-positive cells are enriched in immune cells with an enrichment of approximately 60% (**Figure 3.11 B)).** There seemed to be some enrichment for neurons in mCherry-positive cells, corroborating previous IHC and Flow cytometry results **(Figure 3.5 and 3.6).** Glial cells and vascular cells were more enriched in the mCherry-negative population. Almost no glial cell enrichment was seen in the mCherry-positive population. This was expected as glial cells and vascular cells were not the major cell types in mCherry-positive cells as

observed in previous IHC and Flow cytometry results. These results suggest that the majority of mCherry-positive cells in the sorted population are immune cells, adding to previous IHC findings. Moreover, differential gene expression analysis shows immune-related genes upregulated in mCherry-positive cells, which complements these findings. Through three different techniques, flow cytometry, IHC, and FACS we can confirm that indeed mCherry-positive cells are enriched for neurons and that vascular and glial cells seem to have minor contributions. Additionally, our FACS results suggest the presence of a very high immune component in the mCherry-positive cell population. There results also highlight the consistency of our optimized protocol as the three biological replicates are also very consistent.

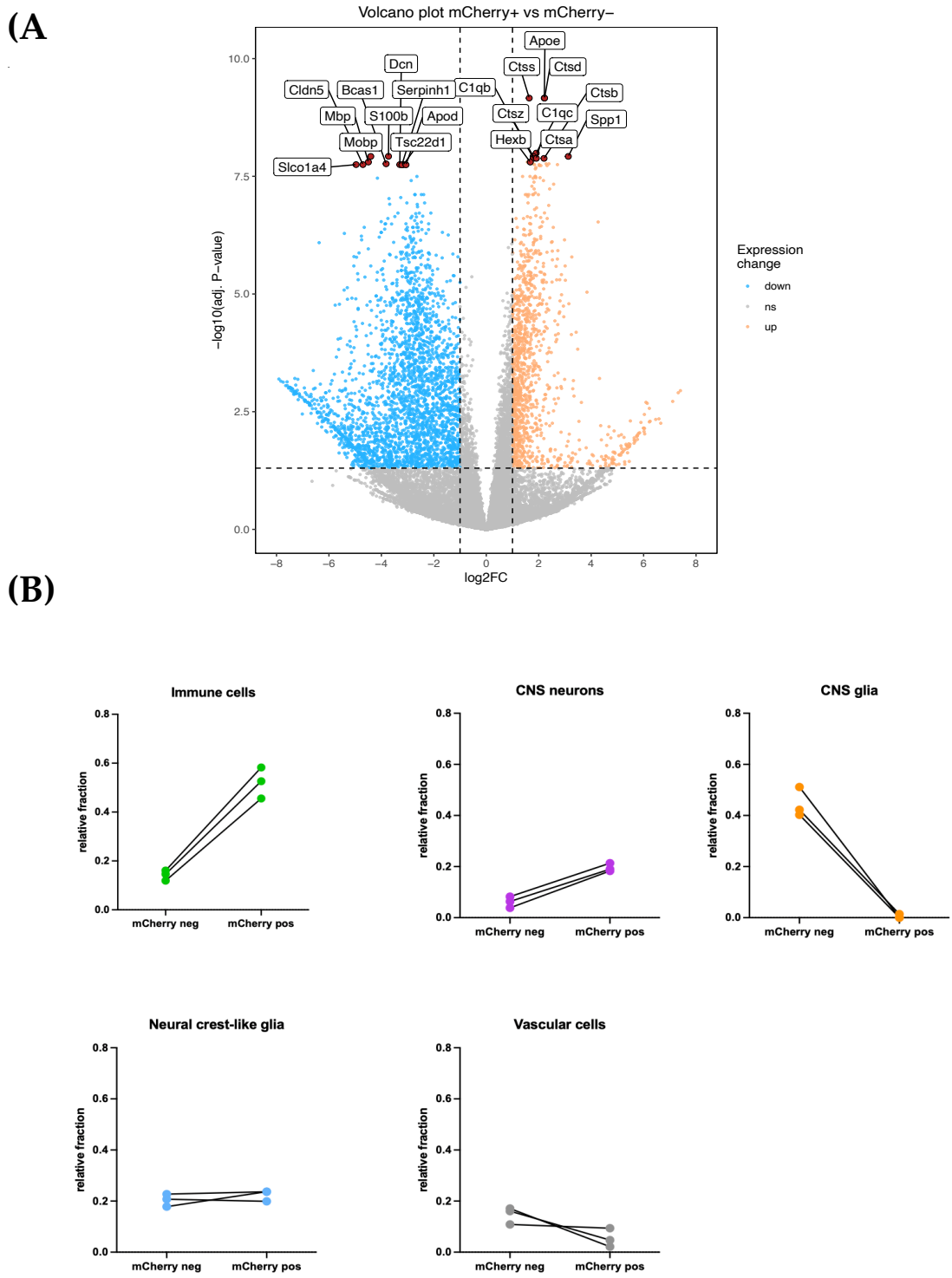

Figure 3.11- mCherry-positive cells are enriched for immune cells and neurons following spinal cord injury A) Volcano plot illustrating differential gene expression between mCherry-positive and mCherry-negative cells. The x-axis represents log2 fold change (log2FC), while the y-axis indicates -log10 (adjusted p-value). Significant genes are marked, with vertical dotted lines denoting biological significance cutoffs ($|\log2FC| > 1$) and a horizontal line indicating statistical significance (adjusted p-value < 0.05). Upregulated genes in mCherry-positive cells include *spp1*, *ctss*, *ctsd*, *ctsb*, *ctsz*, *ctsa*, *c1qc* *hexb*, and *apoe*, while downregulated genes include oligodendrocyte-related genes such as *mbp*,*bcas1* and *mobp*. **B)** CIBERSORTx results showing the estimated cell type proportion in mCherry-positive and mCherry-negative populations. The analysis reveals a 60% enrichment for immune cells in the mCherry-positive population, with additional contributions from neurons. n =3 biological replicates

4 Discussion

4.1 Discussion

Contrary to what was once thought, senescence is a highly heterogeneous concept. Previous laboratory findings have demonstrated that senescent cells (SeCs) are induced following a spinal cord injury (SCI), and their persistence in the tissue impairs locomotor recovery. p16 is one of the hallmarks of senescence, mediating cell cycle arrest [21]. However, the p16 role is far more nuanced and complex, with other roles in numerous processes, such as tumor development, aging, injury, stem cell renewal, and cell differentiation [6]. Unpublished data from our lab using a p16-mCherry transgenic mouse revealed that an injury-specific population of p16-mCherry cells is induced upon an SCI (Annex**, Figure 6.2**)**.** However, its expression does not follow the same tendency as other SeC populations. Here, by employing a multi-faceted approach with standard and newly optimized techniques, we aimed to perform a phenotypic characterization of this population of cells.

We first optimized a single-cell spinal cord (SC) dissociation protocol for flow cytometry, addressing a critical need in SCI research. We show that the optimized protocol consistently yields a high proportion of live and individual cells **(Figure 3.2)**. The strength of our protocol lies in its ability to identify isolated cells using canonical flow cytometry markers **(Figure 3.3)**. The identified cells are known to reside in the SC or to be recruited upon injury, thus re-enforcing the complete representation of each major SC cell type in the optimized protocol [6]. A key feature and innovation of this protocol is that it was designed to preserve and detect neuronal populations. The highest proportion of isolated cells was Thy1.2+ **(see Figure 3.3 A)**. This was one of our aims as, in previous independent experiments, p16-mCherry cells were shown to exhibit neuron-like morphologies. Moreover, it has been shown that mature neurons can co-localize with p16 in an SCI context and in human aged and Alzheimer's disease brains [13],[69]. Other known differences in the cellular changes observed upon an SCI were also reflected in our results. Injury-specific populations emerge in the injury condition at 7 dpi; this was observed for all cell types, with a particular focus on immune cells (CD45+), especially macrophages and microglia (CD11b+) and (Tmem119+) **(Figure 3.3 B, C)**. These results are not surprising, as both macrophages and microglia peak at 7 dpi after a moderate-severe contusion injury, and both M1 and M2 macrophages are present at the injury site at this timepoint [6]. An expected decrease in the neuronal population was also observed **(Figure 3.3 B, C)**, reflecting the prominent loss of mature neurons upon an SCI [6]. While not statistically significant, possibly due to a small sample size, this trend aligned with expected patterns. An increase in the number of animals used should allow us to draw significant conclusions. Our optimized single-cell isolation protocol provides a robust foundation for future SCI studies. Further optimizations can be implemented to improve the yield or viability of specific cell types, in case a specific enrichment is required. Adjustments to the concentrations of the dissociation enzymes and respective activators can also be made. For example, an increase in the concentration of L-cysteine (papain activator) or the usage of a different activator as a means to prevent neuronal excitotoxicity

(caused by L-cysteine) may improve the dissociation yield. Moreover, we acknowledge that some cell types, such as oligodendrocytes, may have been disregarded in our dissociation protocol. Oligodendrocytes are lipid-rich myelinating cells and, therefore, are less dense [70]. We hypothesize that this cell type may have been substantially lost in the upper layer of the gradient fractioning along with other myelin and less dense debris. Alterations in the concentration and number of Optiprep density gradients can improve cell fractioning and help isolate the different populations with high purity. Protocols have implemented this gradient-specific separation which allowed for the selective enrichment of different cell types in isolated brain tissue [71]. Our protocol was designed to use a large number of markers simultaneously in order to better characterize our cell population **(Table 3.1)**. However, compensating all channels to minimize spectral overlaps was challenging. Nevertheless, were able to overcome this issue and design a robust and reproducible SC color panel that suited our single-cell dissociation protocol. This protocol provides a strong base that can be adapted to answer other scientific questions. In case one wants to characterize further specific types of immune cells or neurons retrieved, it would be advised to separate the cell markers into different panels, thus avoiding reaching the detection limit of the equipment. Equipment alterations can also be made to adapt to specific needs, for example, a switch from conventional flow cytometry to spectral flow cytometry, as the latter allows high overlapping spectra to be resolved [72].

In parallel, we showed a highly significant induction in the p16-mCherry population at 7 dpi, corroborating previous independent IHC results **(Figure 3.4 and** Annex**, Figure 6.2).** Furthermore, p16-mCherry high and low populations can be seen through flow cytometry, indicating different reporter expression levels as already described **(Figure 3.4 A)** [40]. We complemented these results by introducing an earlier 3 dpi timepoint **(Figure 3.4)**. No significant differences were observed, possibly indicating that p16 is not expressed or is below detection levels **(Figure 3.4 B)**. Establishing a more rigorous profile assessment of other timepoints, such as 5 dpi, could be valuable in the future. Surprisingly, sham injury mice present significantly more p16-mCherry cells than uninjured controls **(Figure 3.4. B).** This may be due to an unexpected sham effect. Although we attempt to keep the SC untouched, there might be some remaining bone fragments near the SC that could possibly cause a minor injury. However, the latter should reflect a lower BMS score in these animals, which was not the case in all our four biological replicates (from two independent experiments) refer to annex**, Figure 6.4**. The former can be justified by mechanical stress to the tissue, triggering cell responses that in turn lead to p16 expression. In fact, sham-related alterations different from naïve animals have been previously reported. [73]. These findings highlight the importance of including both sham and uninjured controls when accessing the temporal profile of these cells. By including all the appropriate controls, our results gain strength and robustness. During this project, an additional control was made with injured *wt* p16-FDR littermate controls ($p16^{+/+}$), which are injured mice without the FDR cassette. One was included at 3 dpi and another at 7 dpi. However, the small sample size due to the rarity of this genotype led us to exclude this data from our main results. Nevertheless, the percentage of p16-mCherry cells resembled those in uninjured controls. For more information, refer to **annex, Figure 6.5**.

After establishing the temporal profile of p16-mCherry cells, we were determined to characterize this population. IHC results show a predominance of p16-mCherry neurons at 7 dpi **(Figure 3.5)**, which aligns with flow cytometry results **(Figure 3.6)**, strengthening the reliability of these findings. However, this predominance was not significant at 7 dpi. Although NeuN can identify most types of neurons, rare exceptions can be made [74]. For instance, γ-motor neurons are not immunohistochemically identified with NeuN, highlighting the need to conduct additional stainings to identify which types of neurons express p16 and confirm the higher proportion at this timepoint [74]. Flow cytometry data detected an injury-specific immune cell p16-mCherry population, which we would have missed by IHC **(Figures 3.6 and 3.7)**. The combination of Tmem119 and CD11b surface markers allows the discovery of an injury-specific p16-mCherry CD11b high population of macrophages, expanding previous results **(Figure 3.6)** [53]. Macrophages have been implicated in SCI contexts [75]. Following an SCI, M2 anti-inflammatory macrophages have a brief peak at 7dpi, but most of the injury site comprises M1, pro-inflammatory macrophages [76]. M1 macrophages are known to hinder regenerative responses upon an SCI, possibly by establishing a chronic inflammatory state. However, in models of skeletal muscle injury, M1 macrophages contribute to injury recovery, suggesting a context-dependent role [75]. Macrophages are also related to senescence processes and have been shown to express p16 and Sa-β-Gal [75]. Thus, it is unsurprising to see a p16-expressing macrophage population in our context, but why would these cells express p16? It has been proposed that p16 has a role in macrophage polarization [75] [77]. Could these p16-macrophages promote M1 to M2 polarization as a beneficial mechanism, or is it the other way around, contributing to a further pro-inflammatory environment? In future research, a suitable immune cell panel should also be included in the following IHC and flow cytometry experiments to confirm flow cytometry findings and better characterize this immune cell compartment, possibly uncovering the role of this population.

We also optimized a robust fluorescence-activated cell sorting (FACS) protocol to sort p16-mCherry cells, as indicated by the consistent PCA and hierarchical clustering results **(Figure 3.10).** Our population had high levels of purity **(table 3.2)**. Nevertheless, optimizations could be made to perform sorting for purity, considering that there is a trade-off between cell number and population purity, which is especially relevant for rare populations such as mCherry. Sorting samples from pooled SC tissue from multiple mice would allow for a better mCherry representation and purity sorting. In FACS, while neurons are enriched in the sorted population of mCherry-positive cells, immune cells are predominant **(Figure 3.11 B)**. At first glance, these results may seem contradictory to our IHC, but they are rather complementary, as the differences may stem from technical limitations **(Figure 3.5)**. One limitation was the absence of a comprehensive panel of immune cell markers, which was not included in our IHC experiments. We also do not discard the hypothesis that the optimized FACS protocol may be more sensitive in sorting smaller cell types, such as immune cells, and less sensitive in sorting cells larger in size, such as neurons, which might have resulted in an underrepresentation of this population in sorted samples and the difference between flow cytometry results, which also point to a neuronal predominance. However, as FACS analysis was based on RNA expression, taking into consideration several markers and levels of marker expression within our dataset, we may not discard the reliability of this data. To confirm this, further optimizations, such as changing the nozzle size, can be made to ensure a

representative neuronal population. All things considered, these findings indicate that both immune cells, with a specific population of macrophages and neurons, both express mCherry (p16).

At 15 dpi, most of the p16-mCherry cells are mature neurons **(Figure 3.5).** Moreover, when we selectively eliminate this population, a significant locomotor impairment is seen in injured $p16^{FDR/+}$ mice at this timepoint **(Figure 3.9 C)**. One can conjecture that at 15 dpi, most of the p16-mCherry cells are surviving neurons with spared functional connections contributing to locomotion, such as motor neurons that started to express p16 triggered by the injury and stress pathways. And thus, the elimination of these cells at 15 dpi would be reflected in motor impairments. This hypothesis can be substantiated by the fact that it has been reported that neurons can express p16 in response to mild traumatic brain injury due to genotoxic stress [78]. Additional studies must be done to determine which neurons are being targeted by using Choline Acetyltransferase (Chat) together with other motor neuron markers[79]. However, surprisingly, this impairment is transient, which indicates that the p16-mCherry cells eliminated at 15 dpi are not essential for the overall locomotor recovery, and other compensatory mechanisms may be present. Although our results are not able to thoroughly answer this intriguing behavior, they provide a starting point for future research.

At 30 dpi, the clear neuronal predominance seen at 15 dpi is not present, indicating that neurons may not be the primary cell type expressing p16-mCherry **(Figure 3.5 B and C)**. No locomotor impairment is observed at this timepoint. This could be due to the fact that diphtheria toxin (DT) is only administered until 10 dpi, having no effect at 30 dpi. However, in independent experiments, we attempted to administer DT at later timepoints and observed no locomotor effect. Interestingly, p16-mCherry neurons share the spotlight with p16-mCherry microglia at 30 dpi (**Figure 3.5 B and C**). This shift in the p16-mCherry cellular diversity at 30 dpi may reflect relevant molecular alterations. It has been shown that microglia depletion after an SCI impaired glial scar formation, promoted the infiltration of immune cells, hindered neuronal survival, and impaired recovery after an SCI [80]. Elimination of p16-mCherry cells at a later timepoint may have other unforeseen molecular and not motor consequences. Further research should be made to assess if molecular alterations are present. The p16-mCherry cell characterization at 15 and 30 dpi was done only by IHC. Characterization of these cell populations at 15 or 30 dpi could also be attempted through flow cytometry. However, this could be challenging as p16-mCherry cells tend to decrease with time (**Annex, Figure 6.2**). Pooling samples from multiple animals could be a way to overcome this challenge. Magnetic-based cell enrichment approaches have also been made to enrich central nervous tissue cell suspensions; enriching the samples with p16-mCherry cells prior to staining is also a viable approach [81].

Of all the subjects explored and developed in this dissertation, senescence is the one that presents the most unanswered questions. From previous independent results, mCherry-positive cells do not accumulate over time contrary to the standard SA-β-gal + cells in an injury context, indicating that p16 might not fit the canonical senescence profile (**Annex, Figure 6.2**), [13]. From the results of the ABT-263 study, p16-positive cells might not be the same as SA-β-gal positive cells since no significant differences were noted in the p16-population upon ABT-263 treatment, contrary to what was seen in the SA-β-gal

population **(Figure 3.8 D)**. As of recently, co-staining of both p16-mCherry and SA-β-gal was unfeasible. However, we may now use a different acquisition equipment, the Zeiss Axioscan 7, to obtain clearer results. This microscope allows both color and fluorescent image acquisition with the same frame size. We hope these results will help us determine whether mCherry-positive cells may also be SA-β-gal positive.

Surprisingly, there seems to be a tendency for a p16-positive cell increase upon ABT-263 treatment **(Figure 3.8 D)**. This was already observed in traumatic brain injury, where ABT-263 increased the expression of p16 in injured and sham female mice but not their male counterparts, indicating that ABT-263 may not be beneficial in the long run to female mice after injury, perhaps even having off-target effects [78]. In fact, in our study, only female mice were included. However, as these observations were not statistically significant, we must carefully interpret them accordingly. In the meantime, we have already conducted a new experiment using ABT-263. If the tendency stands, the same experimental design should be applied to both female and male groups in the future to assess the differences. Our transcriptomic profiling revealed differentially expressed genes in the mCherry-positive cell population (**Figure 3.11 A)**). Upregulated genes supported the previous findings regarding the immune nature of mCherry-positive cells with an emphasis on the macrophage population. Namely, *spp1*, expressed by both T cells and macrophages, that acts as an immune modulator, and *c1qc*, a component of the classical complement activation pathway. These results suggest that p16-mCherry cells are interacting with the microenvironment. Do they have a beneficial role? Are they the good senescent cells until they are not and need to be eliminated?

All of the top 10 upregulated genes are implicated in the senescence process, possibly indicating the presence of a senescence signature in mCherry-positive cells, complementing previous findings (**Figure 3.11 A)** [53-64]. Particular interest is noted in the cathepsins and hexosaminidase subunit beta, which are involved in lysosomal activity. Senescence is characterized by increased lysosomal activity, and cathepsin b is a known SASP factor [17], [27]. Moreover, in published data from our lab, *Spp1* was also upregulated upon injury and became downregulated upon ABT-263 senolytic treatment, indicating a possible role of Spp1 in the senescence process [13]. Downregulated genes were mostly oligodendrocyte-related, which could reflect oligodendrocyte underrepresentation. This is not surprising, as we previously observed in IHC experiments that oligodendrocytes were not the main mCherry-positive cell type **(Figure 3.5)**. It could also reflect a limitation of our dissociation protocol in failing to retrieve oligodendrocytes from the mixture due to their lipid rich nature. All of these results point towards a senescence nature of our mCherry-positive cells. However, further testing should be done. We could assess other senescence hallmarks, for example see if our mCherry population expresses BCL-2 protein for apoptosis resistance. Moreover, we could use the established and optimized flow cytometry protocol to evaluate the presence of these hallmarks in mCherry-positive cells. For example, label SA-β-gal+ cells with the SPiDER-β-gal fluorescent probe and see if the mCherry population is also positive for SA-β-gal. This could also be an excellent opportunity for future research as this technique has already been established in other contexts [82] .

4.2 Conclusion and Future Perspectives

Our study provided a comprehensive phenotypic characterization of mCherry-positive cells from a molecular, functional, and morphological point of view.

Important questions were raised that should be answered in future research. It would be interesting to know what subtypes of neurons are predominant at 15 dpi, which could explain the locomotor impairment observed. Furthermore, the existence of compensatory mechanisms should also be accessed, which could provide information regarding the transient nature of this impairment. Future research could also focus on unraveling the role of p16-positive macrophages in the SCI context. Are these macrophages beneficial or detrimental? Do they impact senescent cells? Are they involved in macrophage polarization mechanisms, and do they contribute to the inflammatory environment at the injury site? What happens if we eliminate these macrophages? The analysis of our FACS data could provide the answers to these questions and effectively guide our experimental design. This dissertation and independent experiments question the p16 canonical cellular senescence, where a transient profile is observed, contradicting these cells' traditional apoptosis resistance. Therefore, these cells must be further characterized regarding other senescent markers and hallmarks to assess their specific role and determine if they remain senescent in this particular context. In addition to what was previously mentioned, we could also access the expressions of p21, p53, and *glb1*. Furthermore, sex-dependent alterations observed in the p16-positive population should be regarded, especially concerning alterations after senolytic ABT-263 treatment. In addition, the bulk RNA-sequencing results only showed the most visible changes between cell populations. Further analysis will be made to extract more information regarding these cells' functions and the pathways involved.

Altogether, we have successfully developed an optimized protocol for isolating single cells from the spinal cord, which is well-suited for flow cytometry and fluorescence-activated cell sorting (FACS). This protocol, along with immunohistochemistry results, allowed us to see the induction of an injury-specific mCherry population at 7 days post-injury (dpi), which is enriched in neurons. Additionally, by flow cytometry, we also identified a new injury-specific mCherry macrophage population. The selective elimination of mCherry-positive cells revealed a transient locomotor impairment at 15 dpi, suggesting an important functional role for these cells. Pharmacological treatment with a powerful senolytic, ABT-263, did not eliminate p16-positive cells, questioning their canonical senescence nature. However, transcriptomic profiling of sorted mCherry-positive cells revealed an upregulation of immune, senescence, and SASP-associated genes. Our comprehensive approach has revealed new insights into the complex profile of p16-mCherry-positive cells and the interaction between senescence and tissue repair. We hope this work can contribute to a better understanding of the diversity of senescent cells and the intricacies of what it means to be senescent, paving the way for future research.

5 BIBLIOGRAPHY

[1] Harrow-Mortelliti M, Reddy V, and Jimsheleishvili G, "Physiology, Spinal Cord." [Online]. Available: https://www.ncbi.nlm.nih.gov/books/NBK544267/

[2] S. Lukersmith, "International Perspectives on Spinal Cord Injury." [Online]. Available: https://www.who.int/publications/i/item/international-perspectives-on-spinal-cord-injury

[3] L. Sakka, G. Coll, and J. Chazal, "Anatomy and physiology of cerebrospinal fluid," 2011, *Elsevier Masson SAS*. doi: 10.1016/j.anorl.2011.03.002.

[4] P. J. Osseward and S. L. Pfaff, "Cell type and circuit modules in the spinal cord," Jun. 01, 2019, *Elsevier Ltd*. doi: 10.1016/j.conb.2019.03.003.

[5] D. A. Lim, M. Sughrue, and M. W. Mcdermott, "Structure and Function of the Brain and Spinal Cord." doi: 10.1016/B978-1-4160-4653-0.10001-9.

[6] X. Hu *et al.*, "Spinal cord injury: molecular mechanisms and therapeutic interventions," Dec. 01, 2023, *Springer Nature*. doi: 10.1038/s41392-023-01477-6.

[7] A. Anjum *et al.*, "Spinal cord injury: Pathophysiology, multimolecular interactions, and underlying recovery mechanisms," Oct. 02, 2020, *MDPI AG*. doi: 10.3390/ijms21207533.

[8] G. Courtine and M. V. Sofroniew, "Spinal cord repair: advances in biology and technology," 2019, *Nature Publishing Group*. doi: 10.1038/s41591-019-0475-6.

[9] A. M. Te Choo, J. Liu, Z. Liu, M. Dvorak, W. Tetzlaff, and T. R. Oxland, "Modeling spinal cord contusion, dislocation, and distraction: Characterization of vertebral clamps, injury severities, and node of Ranvier deformations," *J Neurosci Methods*, vol. 181, no. 1, pp. 6–17, Jun. 2009, doi: 10.1016/j.jneumeth.2009.04.007.

[10] C. S. Ahuja *et al.*, "Traumatic spinal cord injury," Apr. 27, 2017, *Nature Publishing Group*. doi: 10.1038/nrdp.2017.18.

[11] Charles Aidemise Oyinbo, "Secondary injury mechanisms in traumatic spinal cord injury: a nugget of this multiply cascade," *Acta Neurobiol Exp (Wars)*, 2011.

[12] V. Cigliola, C. J. Becker, and K. D. Poss, "Building bridges, not walls: Spinal cord regeneration in zebrafish," May 01, 2020, *Company of Biologists Ltd*. doi: 10.1242/dmm.044131.

[13] D. Paramos-de-Carvalho *et al.*, "Targeting senescent cells improves functional recovery after spinal cord injury," *Cell Rep*, vol. 36, no. 1, Jul. 2021, doi: 10.1016/j.celrep.2021.109334.

[14] H. X. Nguyen, K. D. Beck, and A. J. Anderson, "Quantitative assessment of immune cells in the injured spinal cord tissue by flow cytometry: A novel use for a cell purification method," *Journal of Visualized Experiments*, no. 50, 2011, doi: 10.3791/2698.

[15] C. S. Ahuja *et al.*, "Traumatic spinal cord injury - Repair and regeneration," *Clin Neurosurg*, vol. 80, no. 3, pp. S22–S90, Mar. 2017, doi: 10.1093/neuros/nyw080.

[16] H. Lorach *et al.*, "Walking naturally after spinal cord injury using a brain–spine interface," *Nature*, vol. 618, no. 7963, pp. 126–133, Jun. 2023, doi: 10.1038/s41586-023-06094-5.

[17] D. Paramos-De-Carvalho, A. Jacinto, and L. Saúde, "Paramos-de-The right time for senescence," 2021, doi: 10.7554/eLife.

[18] R. L. Cohn, N. S. Gasek, G. A. Kuchel, and M. Xu, "The heterogeneity of cellular senescence: insights at the single-cell level," Jan. 01, 2023, *Elsevier Ltd*. doi: 10.1016/j.tcb.2022.04.011.

[19] G. Machado-Oliveira, C. Ramos, A. R. A. Marques, and O. V. Vieira, "Cell senescence, multiple organelle dysfunction and atherosclerosis," Oct. 01, 2020, *Multidisciplinary Digital Publishing Institute (MDPI)*. doi: 10.3390/cells9102146.

[20] N. Ohtani, "The roles and mechanisms of senescence-associated secretory phenotype (SASP): can it be controlled by senolysis?," Dec. 01, 2022, *BioMed Central Ltd*. doi: 10.1186/s41232-022-00197-8.

[21] N. S. Mohamad Kamal, S. Safuan, S. Shamsuddin, and P. Foroozandeh, "Aging of the cells: Insight into cellular senescence and detection Methods," Aug. 01, 2020, *Elsevier GmbH*. doi: 10.1016/j.ejcb.2020.151108.

[22] L. Wang, L. Lankhorst, and R. Bernards, "Exploiting senescence for the treatment of cancer," Jun. 01, 2022, *Nature Research*. doi: 10.1038/s41568-022-00450-9.

[23] L. Hu *et al.*, "Why Senescent Cells Are Resistant to Apoptosis: An Insight for Senolytic Development," Feb. 16, 2022, *Frontiers Media S.A.* doi: 10.3389/fcell.2022.822816.

[24] A. Hernandez-Segura, J. Nehme, and M. Demaria, "Hallmarks of Cellular Senescence," Jun. 01, 2018, *Elsevier Ltd*. doi: 10.1016/j.tcb.2018.02.001.

[25] C. Correia-Melo *et al.*, "Mitochondria are required for pro-ageing features of the senescent phenotype," *EMBO J*, vol. 35, no. 7, pp. 724–742, Apr. 2016, doi: 10.15252/embj.201592862.

[26] G. Machado-Oliveira, C. Ramos, A. R. A. Marques, and O. V. Vieira, "Cell senescence, multiple organelle dysfunction and atherosclerosis," Oct. 01, 2020, *Multidisciplinary Digital Publishing Institute (MDPI)*. doi: 10.3390/cells9102146.

[27] V. Gorgoulis *et al.*, "Cellular Senescence: Defining a Path Forward," Oct. 31, 2019, *Cell Press*. doi: 10.1016/j.cell.2019.10.005.

[28] Y. J. Liu, R. L. McIntyre, G. E. Janssens, and R. H. Houtkooper, "Mitochondrial fission and fusion: A dynamic role in aging and potential target for age-related disease," *Mech Ageing Dev*, vol. 186, Mar. 2020, doi: 10.1016/j.mad.2020.111212.

[29] Y. Valieva, E. Ivanova, A. Fayzullin, A. Kurkov, and A. Igrunkova, "Senescence-Associated β-Galactosidase Detection in Pathology," Oct. 01, 2022, *Multidisciplinary Digital Publishing Institute (MDPI)*. doi: 10.3390/diagnostics12102309.

[30] J. X. Tan and T. Finkel, "Lysosomes in senescence and aging," *EMBO Rep*, vol. 24, no. 11, Nov. 2023, doi: 10.15252/embr.202357265.

[31] Y. Kwon, J. W. Kim, J. A. Jeoung, M. S. Kim, and C. Kang, "Autophagy is pro-senescence when seen in close-up, but anti-senescence in long-shot," 2017, *Korean Society for Molecular and Cellular Biology*. doi: 10.14348/molcells.2017.0151.

[32] S. Lopes-Paciencia, E. Saint-Germain, M. C. Rowell, A. F. Ruiz, P. Kalegari, and G. Ferbeyre, "The senescence-associated secretory phenotype and its regulation," *Cytokine*, vol. 117, pp. 15–22, May 2019, doi: 10.1016/j.cyto.2019.01.013.

[33] L. Antelo-Iglesias, P. Picallos-Rabina, V. Estévez-Souto, S. Da Silva-Álvarez, and M. Collado, "The role of cellular senescence in tissue repair and regeneration," *Mech Ageing Dev*, vol. 198, Sep. 2021, doi: 10.1016/j.mad.2021.111528.

[34] Y. Saito, S. Yamamoto, and T. S. Chikenji, "Role of cellular senescence in inflammation and regeneration," Dec. 01, 2024, *BioMed Central Ltd*. doi: 10.1186/s41232-024-00342-5.

[35] W. Huang, L. T. J. Hickson, A. Eirin, J. L. Kirkland, and L. O. Lerman, "Cellular senescence: the good, the bad and the unknown," Oct. 01, 2022, *Nature Research*. doi: 10.1038/s41581-022-00601-z.

[36] D. Muñoz-Espín *et al.*, "XProgrammed cell senescence during mammalian embryonic development," *Cell*, vol. 155, no. 5, p. 1104, Nov. 2013, doi: 10.1016/j.cell.2013.10.019.

[37] M. Demaria *et al.*, "An essential role for senescent cells in optimal wound healing through secretion of PDGF-AA," *Dev Cell*, vol. 31, no. 6, pp. 722–733, Dec. 2014, doi: 10.1016/j.devcel.2014.11.012.

[38] H. Safwan-Zaiter, N. Wagner, and K. D. Wagner, "P16INK4A—More Than a Senescence Marker," Sep. 01, 2022, *MDPI*. doi: 10.3390/life12091332.

[39] S. Haston *et al.*, "Clearance of senescent macrophages ameliorates tumorigenesis in KRAS-driven lung cancer," *Cancer Cell*, vol. 41, no. 7, pp. 1242-1260.e6, Jul. 2023, doi: 10.1016/j.ccell.2023.05.004.

[40] S. Haston, "INVESTIGATION OF THE TUMOUR PROMOTING EFFECTS OF CELLULAR SENESCENCE DURING PITUITARY AND LUNG TUMOURIGENESIS."

[41] M. Sharif-Alhoseini *et al.*, "Animal models of spinal cord injury: A systematic review," Aug. 01, 2017, *Nature Publishing Group*. doi: 10.1038/sc.2016.187.

[42] E. Lilley *et al.*, "Refining rodent models of spinal cord injury," Jun. 01, 2020, *Academic Press Inc.* doi: 10.1016/j.expneurol.2020.113273.

[43] R. Nardone *et al.*, "Rodent, large animal and non-human primate models of spinal cord injury," Aug. 01, 2017, *Elsevier GmbH*. doi: 10.1016/j.zool.2017.06.004.

[44] T. Cheriyan *et al.*, "Spinal cord injury models: A review," 2014, *Nature Publishing Group*. doi: 10.1038/sc.2014.91.

[45] J. Gaire *et al.*, "Spiny mouse (Acomys): an emerging research organism for regenerative medicine with applications beyond the skin," Dec. 01, 2021, *Nature Research*. doi: 10.1038/s41536-020-00111-1.

[46] N. A. Silva, N. Sousa, R. L. Reis, and A. J. Salgado, "From basics to clinical: A comprehensive review on spinal cord injury," 2014, *Elsevier Ltd*. doi: 10.1016/j.pneurobio.2013.11.002.

[47] A. M. Te Choo, J. Liu, Z. Liu, M. Dvorak, W. Tetzlaff, and T. R. Oxland, "Modeling spinal cord contusion, dislocation, and distraction: Characterization of vertebral clamps, injury severities, and node of Ranvier deformations," *J Neurosci Methods*, vol. 181, no. 1, pp. 6–17, Jun. 2009, doi: 10.1016/j.jneumeth.2009.04.007.

[48] D. M. Basso, L. C. Fisher, A. J. Anderson, L. B. Jakeman, D. M. Mctigue, and P. G. Popovich, "Basso Mouse Scale for Locomotion Detects Differences in Recovery after Spinal Cord Injury in Five Common Mouse Strains," 2006.

[49] J. E. Huettner and R. W. Baughman, "Primary Culture of Identified Neurons from the Visual Cortex of Postnatal Rats," 1986.

[50] A. Reichard and K. Asosingh, "Best Practices for Preparing a Single Cell Suspension from Solid Tissues for Flow Cytometry," *Cytometry Part A*, vol. 95, no. 2, pp. 219–226, Feb. 2019, doi: 10.1002/cyto.a.23690.

[51] R. Z. Hussain *et al.*, "Defining standard enzymatic dissociation methods for individual brains and spinal cords in EAE," *Neurol Neuroimmunol Neuroinflamm*, vol. 5, no. 2, Mar. 2018, doi: 10.1212/NXI.0000000000000437.

[52] F. F. Chiang, T. H. Chao, S. C. Huang, C. H. Cheng, Y. Y. Tseng, and Y. C. Huang, "Cysteine Regulates Oxidative Stress and Glutathione-Related Antioxidative Capacity before and after Colorectal Tumor Resection," *Int J Mol Sci*, vol. 23, no. 17, Sep. 2022, doi: 10.3390/ijms23179581.

[53] M. L. Bennett *et al.*, "New tools for studying microglia in the mouse and human CNS," *Proc Natl Acad Sci U S A*, vol. 113, no. 12, pp. E1738–E1746, Mar. 2016, doi: 10.1073/pnas.1525528113.

[54] I. A. Mohamed, A. P. Gadeau, A. Hasan, N. Abdulrahman, and F. Mraiche, "Osteopontin: A promising therapeutic target in cardiac fibrosis," Dec. 01, 2019, *MDPI*. doi: 10.3390/cells8121558.

[55] S. R. Rittling and R. Singh, "Osteopontin in immune-mediated diseases," *J Dent Res*, vol. 94, no. 12, pp. 1638–1645, Dec. 2015, doi: 10.1177/0022034515605270.

[56] D. Sawaki *et al.*, "Osteopontin promotes age-related adipose tissue remodeling through senescence-associated macrophage dysfunction," *JCI Insight*, vol. 8, no. 8, 2023, doi: 10.1172/jci.insight.145811.

[57] T. Yadati, T. Houben, A. Bitorina, and R. Shiri-Sverdlov, "The Ins and Outs of Cathepsins: Physiological Function and Role in Disease Management," Jul. 13, 2020, *NLM (Medline)*. doi: 10.3390/cells9071679.

[58] S. Patel, A. Homaei, H. R. El-Seedi, and N. Akhtar, "Cathepsins: Proteases that are vital for survival but can also be fatal," Sep. 01, 2018, *Elsevier Masson SAS*. doi: 10.1016/j.biopha.2018.05.148.

[59] "aging-16-205955-2".

[60] K. Cho, "Emerging Roles of Complement Protein C1q in Neurodegeneration," May 28, 2019, *International Society on Aging and Disease*. doi: 10.14336/AD.2019.0118.

[61] T.-C. Ho *et al.*, "Complement C1q mediates the expansion of periportal hepatic progenitor cells in senescence-associated inflammatory liver", doi: 10.1073/pnas.1918028117/-/DCSupplemental.

[62] S. Marthandan *et al.*, "Conserved senescence associated genes and pathways in primary human fibroblasts detected by RNA-seq," *PLoS One*, vol. 11, no. 5, May 2016, doi: 10.1371/journal.pone.0154531.

[63] M. Rovira *et al.*, "The lysosomal proteome of senescent cells contributes to the senescence secretome," *Aging Cell*, vol. 21, no. 10, Oct. 2022, doi: 10.1111/acel.13707.

[64] Y. Huang and R. W. Mahley, "Apolipoprotein E: Structure and function in lipid metabolism, neurobiology, and Alzheimer's diseases," Dec. 01, 2014, *Academic Press Inc.* doi: 10.1016/j.nbd.2014.08.025.

[65] X. Yang *et al.*, "Apolipoprotein E deficiency exacerbates spinal cord injury in mice: Inflammatory response and oxidative stress mediated by NF-κB signaling pathway," *Front Cell Neurosci*, vol. 12, May 2018, doi: 10.3389/fncel.2018.00142.

[66] J. M. Boggs, "Myelin basic protein: A multifunctional protein," Sep. 2006. doi: 10.1007/s00018-006-6094-7.

[67] T. Ishimoto, K. Ninomiya, R. Inoue, M. Koike, Y. Uchiyama, and H. Mori, "Mice lacking BCAS1, a novel myelin-associated protein, display hypomyelination, schizophrenia-like abnormal behaviors, and upregulation of inflammatory genes in the brain," *Glia*, vol. 65, no. 5, pp. 727–739, May 2017, doi: 10.1002/glia.23129.

[68] N. Kaushansky, M. Eisenstein, R. Zilkha-Falb, and A. Ben-Nun, "The myelin-associated oligodendrocytic basic protein (MOBP) as a relevant primary target autoantigen in multiple sclerosis," Feb. 2010. doi: 10.1016/j.autrev.2009.08.002.

[69] J. R. Herdy *et al.*, "Increased post-mitotic senescence in aged human neurons is a pathological feature of Alzheimer's disease," *Cell Stem Cell*, vol. 29, no. 12, pp. 1637-1652.e6, Dec. 2022, doi: 10.1016/j.stem.2022.11.010.

[70] N. Jackman, A. Ishii, and R. Bansal, "Oligodendrocyte development and myelin biogenesis: Parsing out the roles of glycosphingolipids," Oct. 2009. doi: 10.1152/physiol.00016.2009.

[71] G. J. Brewer and J. R. Torricelli, "Isolation and culture of adult neurons and neurospheres," *Nat Protoc*, vol. 2, no. 6, pp. 1490–1498, Jun. 2007, doi: 10.1038/nprot.2007.207.

[72] J. P. Nolan and D. Condello, "Spectral flow cytometry," *Curr Protoc Cytom*, no. SUPPL.63, 2013, doi: 10.1002/0471142956.cy0127s63.

[73] A. De Biase *et al.*, "Gene expression profiling of experimental traumatic spinal cord injury as a function of distance from impact site and injury severity," 2005, doi: 10.1152/physiolgenomics.00081.2005.-Changes.

[74] V. V Gusel'nikova and D. E. Korzhevskiy, "NeuN As a Neuronal Nuclear Antigen and Neuron Differentiation Marker ABBREVIATIONS IHC-immunohistochemical analysis; NeuN-neuronal nuclear protein; shRNA-small hairpin RNA; MAP-2-microtubule-associated protein 2; GFAP-Glial Fibrillary Acidic Protein; TUNEL-Terminal

Deoxynucleotidyl Transferase-Mediated dUTP (2′-Deoxyuridine 5′-Triphosphate) Nick-End Labeling; BrdU-5-bromo-2′-deoxyuridine," 2015.

[75] S. S. Elder and E. Emmerson, "Senescent cells and macrophages: Key players for regeneration?: Senescent cells and macrophages," Dec. 01, 2020, *Royal Society Publishing*. doi: 10.1098/rsob.200309.

[76] L. M. Milich, C. B. Ryan, and J. K. Lee, "The origin, fate, and contribution of macrophages to spinal cord injury pathology," May 01, 2019, *Springer Science and Business Media Deutschland GmbH*. doi: 10.1007/s00401-019-01992-3.

[77] "aging-v8i7-100991".

[78] N. Schwab, D. Taskina, E. Leung, B. T. Innes, G. D. Bader, and L. N. Hazrati, "Neurons and glial cells acquire a senescent signature after repeated mild traumatic brain injury in a sex-dependent manner," *Front Neurosci*, vol. 16, Nov. 2022, doi: 10.3389/fnins.2022.1027116.

[79] X. Zhou *et al.*, "Identification of sensory and motor nerve fascicles by immunofluorescence staining after peripheral nerve injury," *J Transl Med*, vol. 19, no. 1, Dec. 2021, doi: 10.1186/s12967-021-02871-w.

[80] H. Fu, Y. Zhao, D. Hu, S. Wang, T. Yu, and L. Zhang, "Depletion of microglia exacerbates injury and impairs function recovery after spinal cord injury in mice," *Cell Death Dis*, vol. 11, no. 7, Jul. 2020, doi: 10.1038/s41419-020-2733-4.

[81] T. A. Volden, C. D. Reyelts, T. A. Hoke, J. Arikkath, and S. J. Bonasera, "Validation of Flow Cytometry and Magnetic Bead-Based Methods to Enrich CNS Single Cell Suspensions for Quiescent Microglia," *Journal of Neuroimmune Pharmacology*, vol. 10, no. 4, pp. 655–665, Dec. 2015, doi: 10.1007/s11481-015-9628-7.

[82] V. Moiseeva *et al.*, "Senescence atlas reveals an aged-like inflamed niche that blunts muscle regeneration," *Nature*, vol. 613, no. 7942, pp. 169–178, Jan. 2023, doi: 10.1038/s41586-022-05535-x.

6 ANNEXES

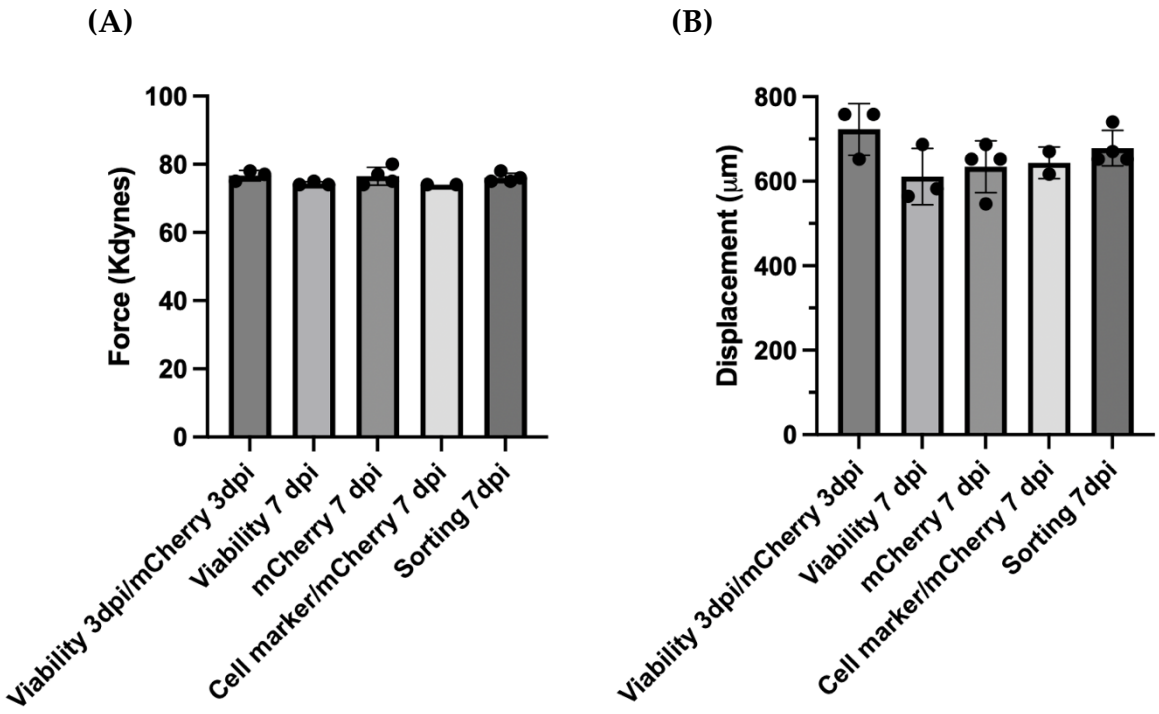

Figure 6.1. Surgical parameters, Force and Displacement, for spinal cord injury in p16-FDR mice. (A) Applied force during injury induction. The graph shows the force applied to the spinal cord, measured in kilodynes (kdyn), for each individual mouse. **(B)** Tissue displacement during injury. The graph illustrates the extent of spinal cord displacement, measured in micrometers (μm), for each individual mouse. Each dot represents an individual mouse. These parameters were measured to ensure consistency in the spinal cord injury model across all experimental animals. The tight clustering of data points in both graphs demonstrates the reproducibility of the injury procedure.

Table A 1. Quality information of the RNA extracted from sorted mCherry cells

Sample	Aria III cell nr reported (240619)	Nanodrop (ng/uL)	Volume (uL)	Fragment Analyzer - RQN (IGC)	Fragment Analyzer - 26S/18S (IGC)	Fragment Analyzer - ng/uL (IGC)	Total (ng)
R205377dpi mCherry- (alfa 1)	369741	4,2	26	8,8	1,5	0,5824	15,1
R205377dpi mCherry+ (alfa 1)	16112	3,3	26	8	1,7	0,2641	6,9
LL205327dpi mCherry- (alfa 2)	300178	4,0	26	8,7	1,8	0,7106	18,5
LL205327dpi mCherry+ (alfa 2)	31248	4,8	26	9,4	1,6	1,4630	38,0
RL205117dpi mCherry- (alfa 3)	196049	6,4	26	9,9	1,6	1,2948	33,7
RL205117dpi mCherry+ (alfa 3)	65970	9,2	26	9,3	1,8	5,9465	154,6
LL205507dpi mCherry- (alfa 4)	335448	4,8	26	9,2	2,3	1,1012	28,6
LL205507dpi mCherry+ (alfa 4)	44675	9,8	26	9,4	2,1	3,4287	89,1

(A

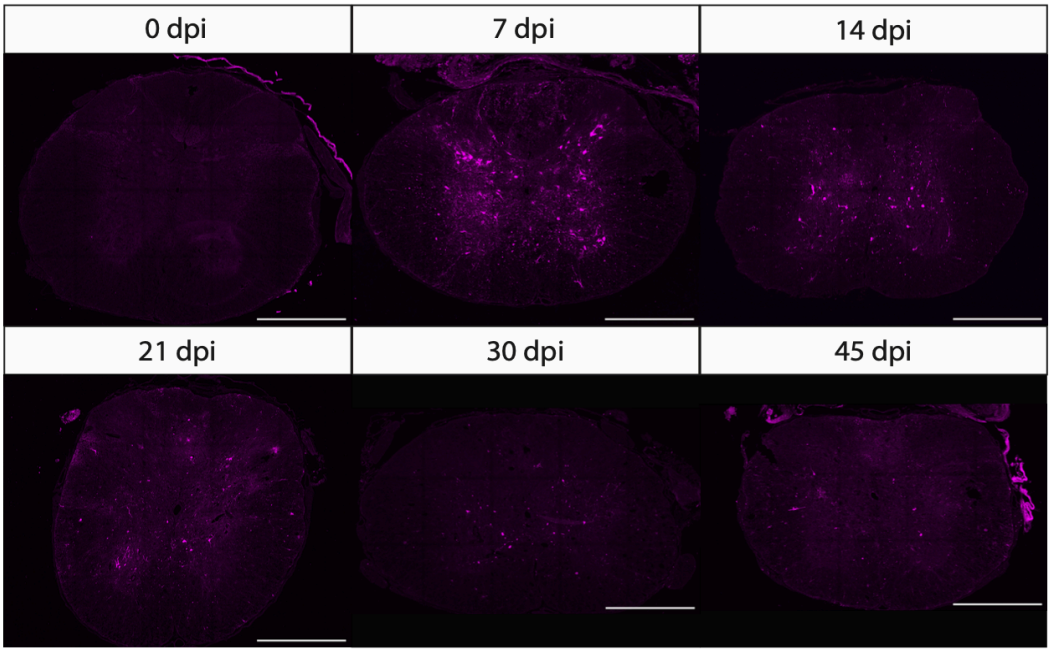

(B

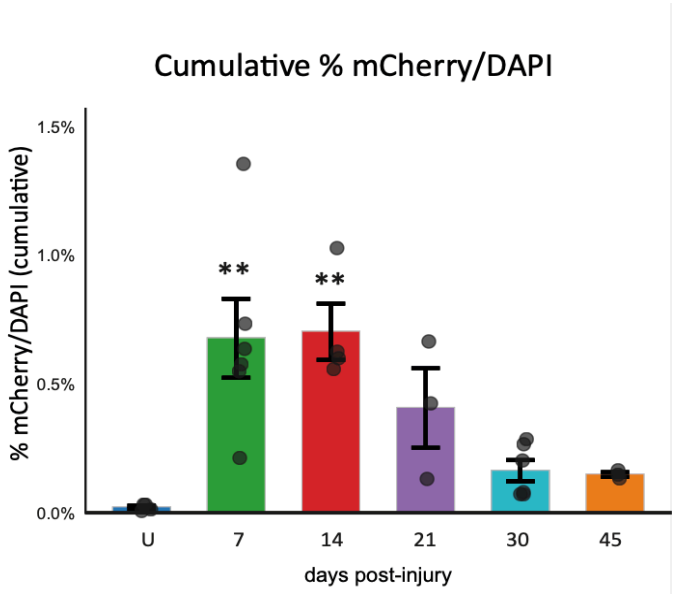

Figure 6.2. p16-mCherry positive cells present a transient profile across time (0, 7 ,14 ,21 ,30, 45 dpi) A) Representative images of the immunohistochemistry performed for mCherry at 0, 7 ,14 ,21 ,30 and 45 dpi. B) Quantification of mCherry-positive cells across time reveals a transient profile of this cell population. Data are presented as means ± SEM, based on *n* =3-6, each dot in the graph represents data from a single animal. Statistical analysis was performed using one-way ANOVA with Bonferroni's correction (95% confidence interval). Statistical significance is indicated as follows: **$p < 0.01$.

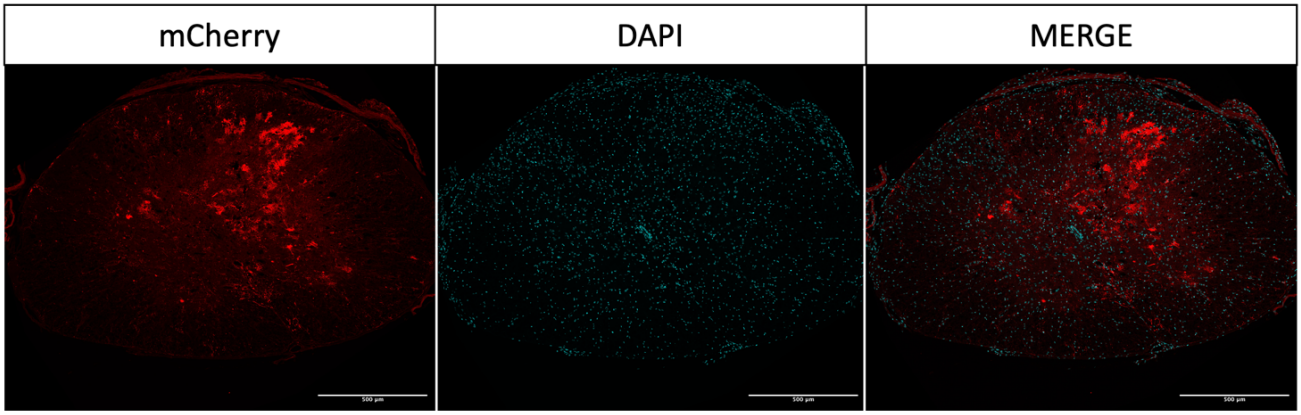

Figure 6.3. Immunohistochemistry of mCherry-positive cells at 3 dpi. Representative images of the immunohistochemistry performed for mCherry at 3dpi reveal a highly heterogeneous and diffuse signal. The staining pattern exhibited substantial variability and lacked distinct cellular localization, precluding reliable quantification. The complex and irregular nature of the signal suggests a need for alternative or complementary analytical approaches to accurately assess mCherry expression in this context.

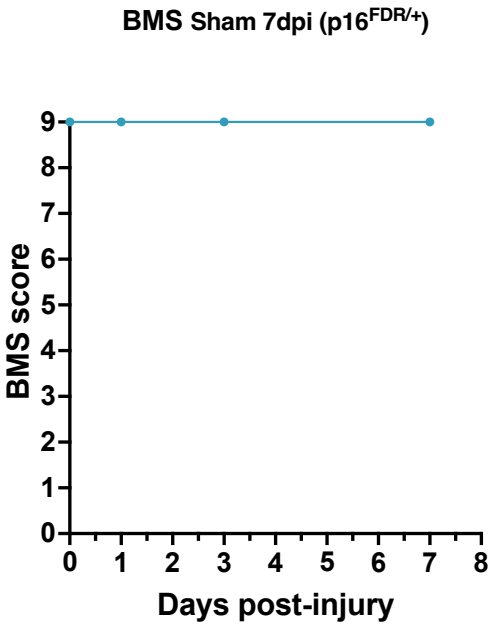

Figure 6.4 BMS score analysis of sham-injured p16-FDR mice demonstrates consistent locomotor function over time. Sham-injured mice maintained the maximum BMS score throughout the evaluation period, with no significant changes observed at 0-, 1-, 3-, and 7-days post-injury (dpi). This consistent performance suggests that the laminectomy procedure alone did not induce detectable alterations in locomotor behavior as measured by the BMS scale.

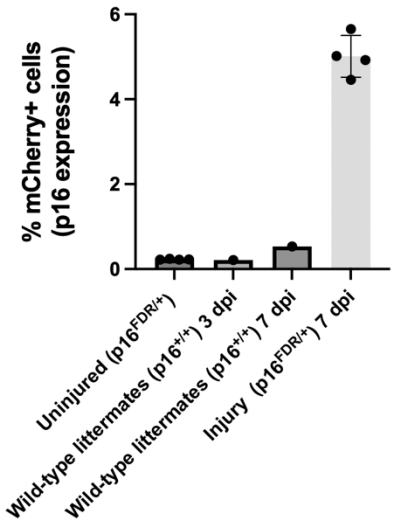

Figure 6.5. Analysis of mCherry expression in Wild-type littermates (p16+/+) p16-FDR controls at 3 and 7 dpi revealed levels similar to those of uninjured controls. At 3 dpi, injured WT controls exhibited mCherry expression levels similar to uninjured controls. At 7 dpi, a slight increase in mCherry expression was observed in WT controls compared to uninjured controls, but this difference remained minimal in terms of order of magnitude. These results suggest that, as expected, the mCherry cassette is not expressed in injured WT controls or under uninjured conditions, confirming the specificity of the expression system used.